Rydberg Atoms in Ponderomotive Potentials

by

Brenton J. Knuffman

A dissertation submitted in partial fulfillment
of the requirements for the degree of
Doctor of Philosophy
(Applied Physics)
in The University of Michigan
2009

Doctoral Committee:

Professor Georg A. Raithel, Chair
Professor Timothy E. Chupp
Professor R. Paul Drake
Associate Professor Luming Duan
Assistant Professor Aaron E. Leanhardt

ACKNOWLEDGEMENTS

I would like to thank Georg Raithel. It has been a privilege to have him as my adviser. His knowledge of science impressive, and his enthusiasm and patience for sharing it with others is equally inspiring. I have learned a great deal both from his technical expertise and from the example of professionalism he sets. Working in the Raithel lab for the past four years, I have had the pleasure of working with many fine individuals with whom I have shared many good times and from whom I have learned a great deal. I would like to thank members of the Raithel Group past and present, David Anderson, Jae-Hoon Choi, Katie Crimmins, Tara Cubel Liebisch, Jeff Guest, Cornelius Hempel, Juwon Lee, Rahul Mhaskar, Jordan Montgomery, Melinda Morang, Natalya Morrow, Louise Yuru Niu, Spencer Olson, Eric Paradis, Aaron Reinhard, Rachel Sapiro, Andy Schwarzkopf, Mallory Traxler, Varun Vaidya, Kelly Younge, and Rui Zhang, for making my time in the lab such a positive experience.

I gratefully acknowledge Kelly Younge and my committee members, Professor Raithel, Professor Timothy E. Chupp, Professor R. Paul Drake, Associate Professor Luming Duan, and Assistant Professor Aaron E. Leanhardt, for careful reading of this dissertation and their constructive critiques.

Many people have played important parts in my formal education, and to all these people, I am grateful. I would like to specifically thank Sister Celine Schumacher, my high school physics teacher. I would also like to acknowledge Professor Gangapodhyaya, Professor Mallow, Professor Ramsey, and the rest of the faculty and staff for

helping me develop during my undergraduate years.

Since moving to Ann Arbor, I have formed many friendships that I value greatly. From the outset, the Applied Physics office crew, Art, Eric, Erik, Kevin, and Malavika (the jewel of Applied Physics), from the first two years at Michigan became fast friends and have been there ever since. Kevin Haworth deserves very special acknowledgement as a great friend and partner in crime; in particular, he has provided me half of his basement for my woodworking shop. I would also like to cite the excellence of the summerof06 crew (you know who you are) for "unprecedented levels of achievement." Special thanks to Thom and Wendy Ryan for giving me a 1987 GMC Sierra pick-up truck. This vehicle has served me faithfully during my graduate school years, and I hope it will continue to operate so optimally for its new owner, Eric Paradis. Thank you to my Uncle Dave and Aunt Margaret for providing me the family support close by in Michigan. I have enjoyed the opportunity to visit with you regularly and get to know you both more closely. I am "fairly" glad to have made the acquaintance of Lekha Yadav during my time in Ann Arbor (special thanks to Ben Koziol for the introduction). I heartily appreciate her company, and her support and encouragement have meant a great deal to me.

Finally, I wish to thank my family. I am privileged and blessed to be part of such a wonderful family that has really been the cornerstone of my life. Mom and Dad, thank you for all the sacrifices you made to give me a chance to grow. Laura, thank you for keeping in such good contact with me despite frequently "reaching me when I cannot answer." Jason, thanks for being such a great older brother to look up to all these years (also thanks for giving me your Jeep). Jenny, I appreciate all the care packages you sent to me, and your encouragement has reminded me time and time again that "we can lick anything if we try." To my family, I dedicate this work.

TABLE OF CONTENTS

LIST OF FIGURES

Figure

ABSTRACT

In this thesis, we examine the ponderomotive interaction between an applied optical field and a highly excited Rydberg electron. An atom in a Rydberg state is essentially composed of an electron loosely bound, at a relatively large radial separation, to a positive ionic core. As such, the ponderomotive interaction for the Rydberg electron is similar to the interaction with free charges, which has been studied in context of plasma physics, new particle accelerator techniques, ion trapping, and electron diffraction among others. We are focused on using the ponderomotive interaction with the Rydberg electron to exert control over both the center-of-mass and electronic states of translationally cold Rydberg atoms. These capabilities can be adapted as tools for application in many experiments in areas such as atomic spectroscopy and quantum information processing. Our theoretical investigations have provided a well-defined parameter space for our experimental work and have allowed us to develop experimental methods appropriate for studying Rydberg atoms in ponderomotive potentials.

In dense gases of cold Rydberg atoms, rich dynamics stem from electric multipole interactions among the Rydberg atoms. For example, interatomic forces between Rydberg atoms cause state-changing collisions which can significantly increase the kinetic energy of the colliding atoms. In addition to the studies of Rydberg atoms in ponderomotive potentials, we discuss collisions of cold Rydberg atoms in which internal energy of the Rydberg atoms is converted into kinetic energy.

CHAPTER I

Introduction

1.1 Cold Rydberg Gases

A Rydberg atom, composed of a highly excited electron loosely bound at a relatively large radial separation from an ionic core, is a system of great physical interest located on the boundary of classical and quantum physics. These atoms have many exaggerated properties, such as their nearly macroscopic size, large geometrical and collisional cross-sections, huge accessible Hilbert space, extreme sensitivity to externally applied fields, and long lifetimes, which have been studied systematically and in great detail, particularly since the nineteen seventies with the development of tunable dye-laser technology [1]. Recent developments in laser-cooling have renewed interest in Rydberg atoms. One area of major current interest is the study of Rydberg-atom ensembles in which the electric multipole interactions between Rydberg atoms dominate the dynamics of such systems. These interactions can influence laser-excitation dynamics of Rydberg systems in the so-called dipole blockade [2, 3] which creates the necessary entanglement for use in proposed quantum information processing schemes [2, 4]. In cold gases of Rydberg atoms, these strong interactions can occur among a large number of atoms, providing an interesting context for studying many-body physics [5, 6].

Under certain conditions, interactions also induce state-mixing and ionizing collisions in cold Rydberg gases which govern the evolution dynamics of these systems [7]. In chapter II, we examine a how interactions among Rydberg atoms in a cold Rydberg gas cause motion of the atoms, significantly altering the kinetic energy distribution of the constituent atoms [8]. In particular, attractive forces accelerate atoms toward each other, increasing the kinetic energy of the atoms, and these collision often end in Penning ionization. For this study, we developed a time of flight measurement technique, which detects fast atoms that are emitted from the cold Rydberg gas. Since the time-resolved detection occurs at a specified distance from the gas, we can construct velocity distributions of these fast atoms. State selective field ionization and density dependent studies link the increase in kinetic energy of the detected atoms to binary collision processes in cold Rydberg gases in which internal energy of the Rydberg atoms is converted into kinetic energy. We have also adapted this technique to study the formation of Rydberg atoms in an expanding ultracold plasma, presumably through a process called three-body recombination. Our preliminary results are in qualitative agreement with expectations based on ion expansion rates in ultracold plasmas [9] and the density scaling of three-body recombination rates.

1.2 Rydberg Atoms in Ponderomotive Potentials

In the remainder of the text, we investigate the ponderomotive interaction between a Rydberg electron and an applied optical field. Since the Rydberg electron is very weakly bound or quasi-free, its interaction with an applied field is similar to that of a free electron, which has been studied in the context of plasma physics [10], new particle accelerator techniques [11], ion trapping [12, 13], and high-harmonic generation [14], among others. In chapter III, we describe the ponderomotive interaction

involving a Rydberg electron in great detail. In first order, the energy levels of the Rydberg electron in a homogeneous applied optical field are shifted by an amount equal to the shift of a free electron in the same field. However, inhomogeneities in the applied field produce spatially and Rydberg-state dependent energy level shifts, which result in forces on the Rydberg atoms. These forces can be tailored to control the motion of Rydberg atoms. Initial experiments focus on spectroscopically probing these energy level shifts, either in the Rydberg laser-excitation spectra or in microwave spectra between neighboring Rydberg states. In particular, we explore the effects of applying a strongly inhomogeneous standing plane wave optical field, which could be used to form a periodic 1D ponderomotive optical lattice of Rydberg-atom traps. The depth of these traps depends on the intensity of the applied optical field and can easily exceed the average kinetic energy of Rydberg atoms excited from laser-cooled ground state atoms. Rydberg-atom trapping or control of Rydberg atom motion has potentially useful applications in quantum information processing, cavity QED experiments with Rydberg atoms [15], and precision spectroscopy of atomic quantities. Additionally, the ponderomotive optical lattice confines Rydberg atoms with a much smaller trap-induced shift than other Rydberg-trapping schemes [16, 17].

In chapter IV, we propose a new method for driving transitions between Rydberg states by resonantly modulating an applied ponderomotive potential [18]. In particular, we consider a Rydberg atom in a ponderomotive potential formed by a 1D standing plane wave. If the intensity of the plane wave is modulated at frequencies corresponding to transitions from the initial state to another target Rydberg state, the amplitude modulated ponderomotive optical lattice can transfer population between the two states. Rabi frequencies of order 100 kHz are calculated for a wide variety of transitions between nearby Rydberg states under anticipated experimental

conditions. Transitions driven in this way differ from transitions resulting from the direct application of resonant radiation. First, transitions in the modulated lattice are not subject to the familiar dipole selection rules, since the length scale of the spatial variation of the lattice is comparable to the extent of the Rydberg wavefunction. In this case, many nonlinear terms in the transition matrix elements have similar magnitudes and allow the coupling of Rydberg states without well-defined selection rules for the orbital angular momentum quantum number ℓ. However, transitions in the lattice exhibit a $\Delta m = 0$ selection rule, where the quantization axis is defined to be normal to the lattice planes. Second, the modulated lattice can, in principle, be used to drive transitions within an ensemble of Rydberg atoms with micron precision, since the light field which delivers the microwave-frequency perturbation can be focused. Such spatial selectivity is not possible simply with the direct application of microwave radiation. The ponderomotive optical lattice has the capability of manipulating both center-of-mass states and internal states of Rydberg atoms to which it is applied. This combination of capabilities would have potentially useful applications in quantum information processing schemes and high precision Rydberg spectroscopy.

In chapter V, we discuss the development of experimental techniques for applying a ponderomotive potential to Rydberg atoms and probing the effects of the interaction. In particular, we concentrate on creating and aligning a 1D ponderomotive optical lattice formed with a retro-reflected 1064 nm laser beam. To achieve desired intensities, the lattice beams are focused to a spot size of 15 μm. Schemes for localizing Rydberg atoms to the volume subject to the applied ponderomotive potential are discussed in detail. For using the ponderomotive lattice as a spectroscopic tool for coupling Rydberg states, the lattice must be amplitude modulated at frequencies

in the tens of gigahertz range. Techniques for providing this type of modulation to a focused, retro-reflected lattice beam geometry over a broad frequency range are presented. Spectroscopy with direct application of microwaves is a useful tool for characterizing the effects of a ponderomotive potential on a Rydberg atom, and relevant techniques are developed in this chapter as well.

1.3 Relation to Other Work

Cold Rydberg atoms are created by photo-exciting atoms in laser-cooled gases into Rydberg states. The initial kinetic energy of the Rydberg atoms is characteristic of the thermal energy of the laser-cooled atoms from which they are excited. Even at relatively low Rydberg atom densities (of order 10^{-7} cm^{-3}), long range, electric multipole interactions among Rydberg atoms can be large compared to their kinetic energy. The "frozen Rydberg gas" picture of essentially stationary, strongly interacting Rydberg atoms resembles an amorphous solid [19, 20] on time scales less than a couple of microseconds. Coherent many-body interactions among Rydberg atoms in the "frozen Rydberg gas" regime are of great interest in studies of Rydberg atoms. One important example of this is work related to the so-called dipole blockade [2–4], a mechanism central to quantum information processing schemes using Rydberg atoms. On longer time scales, these interactions, which depend strongly on the separation of the atoms, create attractive and repulsive forces on atoms leading motion of the atoms and a variety of incoherent state-changing and ionizing collisions. Our work in chapter II examines the motion of the atoms in a cold Rydberg gas over such longer timescales [8]. The collisions we examine highlight an interesting case where the internal energy of the "frozen," many-body Rydberg system is converted into kinetic energy.

Much of the work in this thesis examines the ponderomotive interaction between a Rydberg electron and an applied optical field. A free electron in an oscillating electric field experiences a ponderomotive energy shift equal to its time-averaged kinetic energy. Spatial inhomogeneities in the applied electric field lead to forces on charged particles. For an optical standing wave, the potential is periodic and represents a potential from which electrons can be scattered (Kapitza-Dirac effect). Rainbow scattering [21], Bragg scattering [22], and diffraction [23] of electrons from high intensity laser pulses have all been observed experimentally. Since the Rydberg electron is weakly bound or quasi-free, its interaction with an oscillating electric field is similar to the ponderomotive interaction with a free electron. This intuition has been confirmed experimentally in measurements of the ponderomotive shift of the laser excitation frequency of a transition from a ground state to a Rydberg state performed on atoms immersed in a high intensity laser field [24]. In our work, we develop schemes for applying periodic ponderomotive potentials to Rydberg atoms in such a way as to control their motion and internal states. Rydberg atom trapping has been demonstrated using magnetic [16] and electrostatic [17] potentials. In chapter III, we discuss trapping cold Rydberg atoms in a ponderomotive optical lattice [25], and in chapter IV, we develop a method for coupling Rydberg states through the application of a time-dependent ponderomotive potential [18]. These methods may become relevant in future coherent-control and quantum information processing applications.

1.4 Experimental Apparatus - Overview

In this section, we present a brief overview of the apparatus used to conduct the experiments presented in the remainder of the thesis. Figure 1.1 shows a picture of

the vacuum chamber that houses the internal elements represented diagrammatically in figure 1.2.

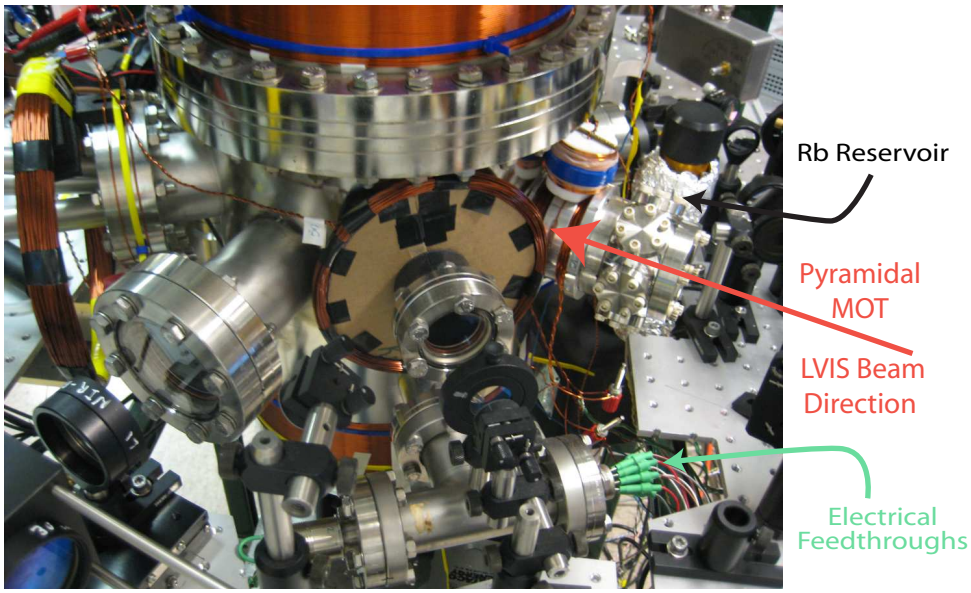

Figure 1.1: Apparatus used to conduct the experiments presented in this thesis.

Cold Rydberg atoms are created by photo-exciting ^{85}Rb atoms (see table 1.1 for relevant atomic data) that have been laser-cooled in the magneto-optical trap (MOT) shown in the picture in figure 1.2. A Rydberg atom created in this way is called "cold" because it has essentially the same kinetic energy as the laser-cooled ground state atom from which it was excited. The MOT in figure 1.2 is loaded from a cold, slow atomic beam (low-velocity, intense source or LVIS) formed in a pyramidal MOT that is located on the right-hand side of figures 1.1 and 1.2. The atomic beam is directed toward the center of the chamber and collected in the six-beam MOT shown in figure 1.2. The various copper wire-wound coils visible in figure 1.1 are used to compensate stray magnetic fields at the location of the MOT.

The primary means for gathering information is through the detection of electrons that originate from the cold Rydberg atoms. Figure 1.2 shows a rendering of the cylindrical electrode package, whose vertical axis corresponds to the central axis of

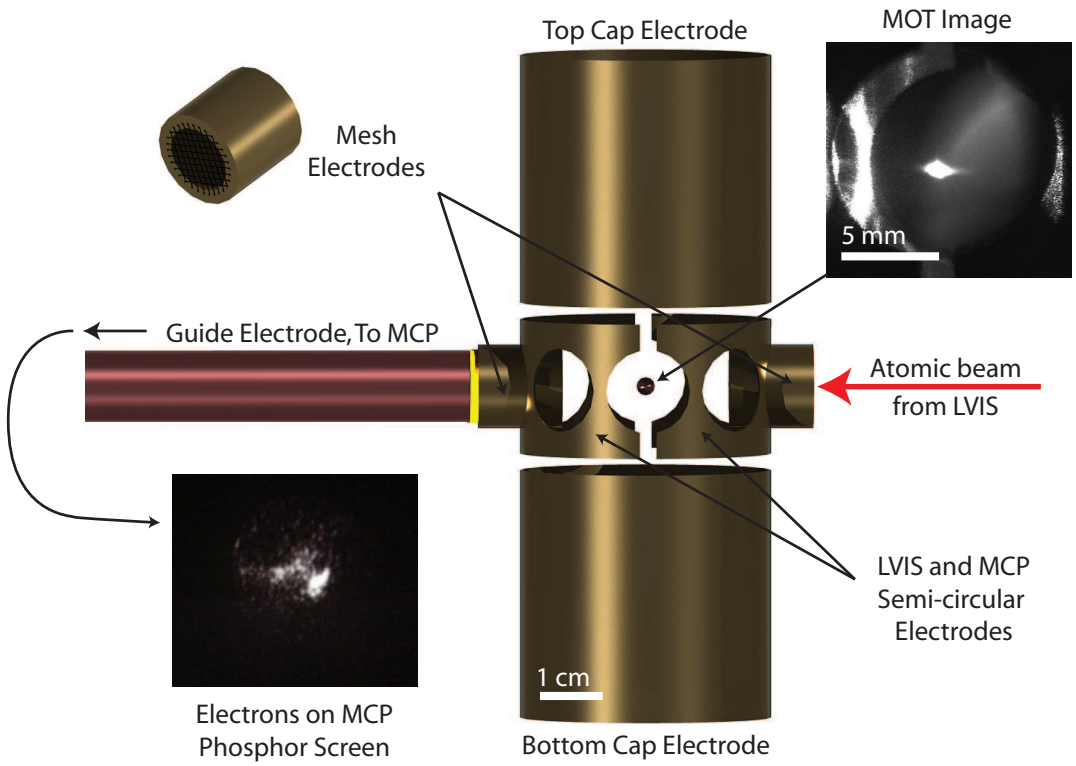

Figure 1.2: Electrode structure for creating and controlling electric fields for use in experiments.

the outer chamber, that facilitates the ionization and detection of the Rydberg electrons. Applying appropriate voltage signals (using the UHV electrical feedthroughs shown in figure 1.1) to the semi-circular electrodes creates an electric field at the location of the atoms that liberates electrons from the cold Rydberg gas (created from photo-excitation of laser-cooled atoms in the MOT) and directs them toward a micro-channel plate detector (MCP).

The signal at the MCP can then be read out temporally and related to the applied voltage. In this way, we construct the probability distribution for detecting an electron at a particular applied electric field. This forms the basis of an essential tool for analyzing the distribution of Rydberg states in a sample, since different Rydberg states tend to ionize at distinct electric fields. This technique is referred to as state selective field ionization. For low angular momentum states, the ionizing electric

Table 1.1: ^{85}Rb Parameters

Atomic Number:	37
Relative Natural Abundance:	72 %
Ground State:	$5S_{1/2}$
Ionization Potential:	33 690.798 47(3) cm^{-1} [26]
Nuclear Spin:	5/2
D_2 Line ($5S_{1/2} \rightarrow 5P_{3/2}$) Parameters	
Wavelength ($F = 3 \rightarrow F' = 4$):	780.244 nm [27]
Resonant Saturation Intensity ($F = 3 \rightarrow F' = 4$):	1.67 mW/cm^2 [27]
Natural Line Width (FWHM):	6.06 MHz [27]
Doppler Temperature:	145.57 μK
Quantum Defects:	$\delta(n) = \delta_0 + \delta_2/(n - \delta_0)^2$
$nS_{1/2}$	$\delta_0 = 3.131804(10)$, $\delta_2 = 0.1784(6)$ [28]
$nP_{1/2}$	$\delta_0 = 2.6548849(10)$, $\delta_2 = 0.2900(6)$ [28]
$nP_{3/2}$	$\delta_0 = 2.6416737(10)$, $\delta_2 = 0.2950(7)$ [28]
$nD_{3/2}$	$\delta_0 = 1.34809171(40)$, $\delta_2 = -0.60286(26)$ [28]
$nD_{5/2}$	$\delta_0 = 1.34646572(30)$, $\delta_2 = -0.59600(18)$ [28]
$nF_{5/2}$	$\delta_0 = 0.0165192(9)$, $\delta_2 = -0.085(9)$ [29]
$nF_{7/2}$	$\delta_0 = 0.0165437(7)$, $\delta_2 = -0.086(7)$ [29]

field in atomic units is typically $E = 1/(16n^{*4})$, where n^* is the effective principal quantum number. These states are said to ionize adiabatically. Higher angular momentum states tend to ionize in the electric field range $1/(9n^{*4}) < E < 1/(4n^{*4})$ and are said to ionize diabatically. It is evident from the differing ionization behavior of the high and low angular momentum states that the detailed mapping of quantum states onto an ionizing electric field is not completely straightforward. However, this technique remains essential for studying cold Rydberg atoms.

CHAPTER II

Cold Rydberg-Rydberg Collisions - Fast Rydberg Atoms

The internal states of atoms in cold Rydberg gases evolve through state-mixing and ionizing collisions with electrons and other Rydberg atoms [7, 20, 30, 31]. In addition to the changes in their internal states, Rydberg-Rydberg collisions in a cold, dense Rydberg gas can lead to the conversion of internal energy into center-of-mass energy of the colliding atoms, resulting in Rydberg-atom velocities much larger than the initial velocities in the gas. In this chapter, we discuss a series of experiments in which we investigate how interactions among Rydberg atoms in a cold Rydberg gas alter the kinetic energy distribution of the constituent atoms [8]. Attractive interactions between Rydberg atoms lead to interatomic forces that accelerate atoms toward each other. On the timescale of a few microseconds, this type of collision often ends in Penning ionization. The accelerated atoms have increased kinetic energy that can be large compared to the initial kinetic energy in a cold Rydberg gas, so we refer to these atoms as "fast" Rydberg atoms.

In the experiments, we prepare cold Rydberg-atom gases by photo-excitation of laser-cooled atom clouds and use time-of-flight measurements to demonstrate the production of fast Rydberg atoms. The velocity distributions of Rydberg atoms emerging from the Rydberg-atom gases are obtained. State-selective field ionization

spectra indicate a correlation between the production of fast Rydberg atoms and the presence of Penning ionization signatures. The connection between the production of fast Rydberg atoms and binary collisions is also supported by examining the number of fast atoms produced as a function of density. Additionally, we will discuss preliminary results from experiments using a similar procedure to study the production of fast Rydberg atoms produced via three-body recombination in an expanding ultracold plasma.

2.1 Binary Rydberg-Rydberg Collisions

In cold Rydberg gases, the kinetic energy of the constituent Rydberg atoms is relatively small. Electric multipolar interactions among the Rydberg atoms can be quite strong and long range. Thus, interesting dynamics in these systems can occur on time scales that are quite small compared to the time scale for appreciable displacement of the Rydberg atoms from their initial positions (relative to the interatomic spacing). The "frozen Rydberg gas" picture of essentially stationary, strongly interacting Rydberg atoms resembles an amorphous solid [19, 20] on time scales less than a couple of microseconds.

On longer time scales, the Rydberg atoms do move about due to thermal motion and accelerate due to interatomic electric multipolar interactions. For the case of attractive interactions between two Rydberg atoms, they would undergo accelerations that reduce their relative interatomic spacing R. When R is small enough that the Rydberg-atom interaction energy is comparable to the binding energy of the Rydberg state, one of the atoms can be ionized, and the other atom de-excited into a more deeply bound state. This process is known as Penning ionization and can be

expressed symbolically as,

$$\mathrm{Ryd}(n_0) + \mathrm{Ryd}(n_0) \rightarrow Ryd(n) + ion + \mathrm{e}^- \quad , \tag{2.1}$$

with n_0 and n denoting the initial and final principal quantum numbers, respectively.

The binary Rydberg-Rydberg interaction (considered in detail in reference [32]) for Rydberg atoms with an appreciable separation relative to the extent of their electronic wavefunction can be described by an essential states model. States coupled via near-resonant channels strongly interact through a resonant dipole-dipole interaction, which scales as n^4/R^3, in contrast to weaker off-resonant van der Waals interactions, which scale as n^{11}/R^6. In a typical Rydberg series, over large n-ranges the interactions are predominately of the off-resonant type; however, resonant interactions occur naturally over small n ranges. Enhancement in the ionization rates of laser excited, low-angular-momentum Rydberg atoms resulting from resonant interaction compared to off-resonant interactions has been observed experimentally [6].

In experiments described in this chapter, the production of fast Rydberg atoms is always accompanied by large amounts of state-mixing collisions, which transfer Rydberg population from laser-excited low angular momentum states to high angular momentum states in nearby hydrogenic manifolds [30]. States in the hydrogenic manifolds tend to mix easily and interact strongly. The strength of these interactions depends on inter-atomic separation as R^{-3}, and on the mutual orientation of the dipole moments of the atoms. Ignoring the angular dependence and following reference [33], we can estimate the time required for two Rydberg atoms interacting via $V \propto n^4/R^3$ (in atomic units) to come together. If we assume that the initial velocity of the Rydberg atoms (of mass M, separated by an amount R_0) is zero, the

relative velocity at a separation R is given in atomic units by

$$v = \sqrt{2n^4(2/M)\left(\frac{1}{R^3} - \frac{1}{R_0^3}\right)} \tag{2.2}$$

From the form of this equation for v, it is clear that the velocity of the Rydberg atoms is increasing as they approach each other. The time for the two atoms to "snap together" is approximately

$$T = \int_0^{R_0} \frac{dR}{v(R)} \approx 20\ \mu\text{s} \times \sqrt{M(\text{amu})R_0^5(\mu\text{m})}/n^2 \tag{2.3}$$

For a cold Rydberg gas at $n = 64$, the timescale (estimated by equation 2.3) over which two atoms separated by the Wigner-Seitz radius corresponding to a Rydberg density of 8×10^8 cm^{-3} is approximately 7 μs. This simple estimate of the collision time agrees quite well with the observations in reference [7] obtained at $n = 64$ and a density of 8×10^8 cm^{-3}. This work used state-selective field ionization techniques to analyze the state distributions in cold Rydberg gases as a function of the delay between the photo-excitation and field ionization of the Rydberg sample (figure 4 in reference [7]). The fraction of the signal associated with Penning ionization reached its maximum in about 12 μs.

In a Penning ionizing collision, the energy difference between the initial and final Rydberg state must be greater than the initial binding energy in order to ionize one collision partner. This energy conservation statement is summarized by the following inequality (given in atomic units), which places the following restriction on the final state distribution of the bound Rydberg atom

$$-1/2n^2 - (-1/2n_0^2) \leq -1/2n_0^2 \Rightarrow n \leq n_0/\sqrt{2} \tag{2.4}$$

where n_0 and n denote the principal quantum number for the initial and final state, respectively. Thus, the maximum final n-value is $\lesssim$ 70 % of the initial n-value.

Classical monte carlo simulations of the collisions of two translationally cold Rydberg atoms were performed in reference [33]. There, final state distributions of n for the bound collision partner were calculated. In these distributions (figure 1 in reference [33]), the weight is concentrated near the $n_0/\sqrt{2}$ upper limit but covers more deeply bound states as well. Since the final states are always more deeply bound than the equality condition, there is an energy balance which must be contained in the kinetic energy of the collision particles. The final velocity distributions for ions obtained from these trajectories show a most probable velocity corresponding to roughly 1 % of the initial binding energy (see figure 2 in reference [33]). Since the mass of the Rydberg atom is similar to that of the ion, the velocity distribution for the bound Rydberg atom would be virtually the same as for the ion. Following reference [33], for $n_0 = 90$ Rydberg atoms, the most probable velocity (which is expected to scale with $1/n_0$) would be about 7 m/s. The initial temperature of the atoms in this calculation was 500 uK, where the r.m.s. velocity is about 40 cm/s. This represents a increase of the kinetic energy of a factor of 300 through this collision process, which converts internal energy of the atoms to kinetic energy of the center of mass.

After the ionizing collision, the liberated electron receives most of the kinetic energy, leaving behind the Rydberg atom and the ion at small relative separation. In this situation, the net positive space-charge would tend to cause repulsion and an increase in the kinetic energy of the collision particles on the outgoing leg of the collision. Also present would be the forces resulting from the interaction of the highly-polarizable Rydberg atom and the inhomogeneous field of the ion. Rydberg atoms in low-electric-field seeking states would be repelled from the ion while Rydberg atoms in high-electric-field seeking states would be attracted to the ion.

To estimate the strength (upper limit) of the polarization potential between the ion and the Rydberg atom, we consider the linear Stark shift of the extreme Stark state $W = 3n^2E/2$ [1]. We take E to be the value of the electric field from the ion at the location of the Rydberg atom center-of-mass. For an $n = 90/\sqrt{2}$ Rydberg atom in the extreme Stark state at a distance of 2.5 μm from a singly charged ion, the Stark shift is 7×10^{-5} eV. For comparison, the kinetic energy of a Rubidium atom moving at 7 m/s (most probable velocity from above) is 2×10^{-5} eV. This estimate indicates the importance of the polarization forces in the outgoing leg of the collision. In fact, the monte carlo simulations of reference [33] revealed the formation of molecular ions in a few percent of the trajectories. Regarding our simple estimate however, the final state distribution will mostly contain states with a shift significantly less than that of the extreme Stark states, and the Coulomb repulsion will also be important since the three-particle interaction is not simply an interaction between a charged particle and a perfect dipole at small relative separations. In any case, these collisions highlight the interplay between the internal state and motion of the collision particles. While most of the energy is transferred to the ionized electron, enough internal energy is transferred to the kinetic energy of the product ion and Rydberg atom that their velocities should exceed the initial thermal velocities by a couple of orders of magnitude [33].

Penning ionization has been studied in other cases, notably, in collisions where metastable helium atoms are directed into a gas of noble-gas atoms or simple molecules. In these experiments, target gas atoms are ionized in collisions with metastable helium. The ionization energy is provided when the metastable atom undergoes a transition to its ground state during the collision. Interaction is primarily mediated by the van der Waals interaction between the atoms that can be considered to be

spherically symmetric [34–36]. Experiments are typically performed at thermal velocities [37]. In cold Rydberg gases, not only is the ionizing interaction mediated by electric multipolar interactions, but the kinetic energy of the collision particles is also determined by these interactions.

2.2 Fast Rydberg Atom Experiments

2.2.1 Apparatus-Experimental Setup

In this section, we discuss the detection of fast Rydberg atoms with velocities up to ~ 10 m/s described in the previous section, that are emitted from cold Rydberg-atom gases [8]. The velocity distributions of these fast atoms have been characterized using a time of flight measurement. Additionally, we have studied the production of fast Rydberg atoms as a function of the initial Rydberg-atom density, upon which many of the processes occurring in cold Rydberg gases depend. Using state-selective field ionization spectra to obtain the probability distribution of ionization electric fields, we are able to characterize the Rydberg-gas conditions that lead to the production of fast Rydberg atoms, and have found a correlation between the signature of Penning ionization and the production of fast Rydberg atoms.

In our experiment, ^{85}Rb atoms are loaded into a magneto-optical trap from a low-velocity intense source (LVIS [38]). The trapping light is used to excite atoms from the $5S_{1/2}$ to the $5P_{3/2}$ state. The cold Rydberg gas is prepared by exciting atoms from the $5P_{3/2}$ state into Rydberg states by a tunable pulsed dye laser ($\lambda \approx 480$ nm, pulse width ≈ 10 ns, bandwidth ≈ 15 GHz, pulse energy $\lesssim 1$ mJ, fluence $\Phi \approx 3 \times 10^{15}$ photons/cm^2). Excitation into the $n_0 = 90$ Rydberg state (typical of many of these experiments) actually refers to excitation into a range of states ($\Delta n \approx 5$) centered at $n_0 = 90$. Initially the angular momentum of these states is predominately of D character since the oscillator strength from the $5P$ intermediate

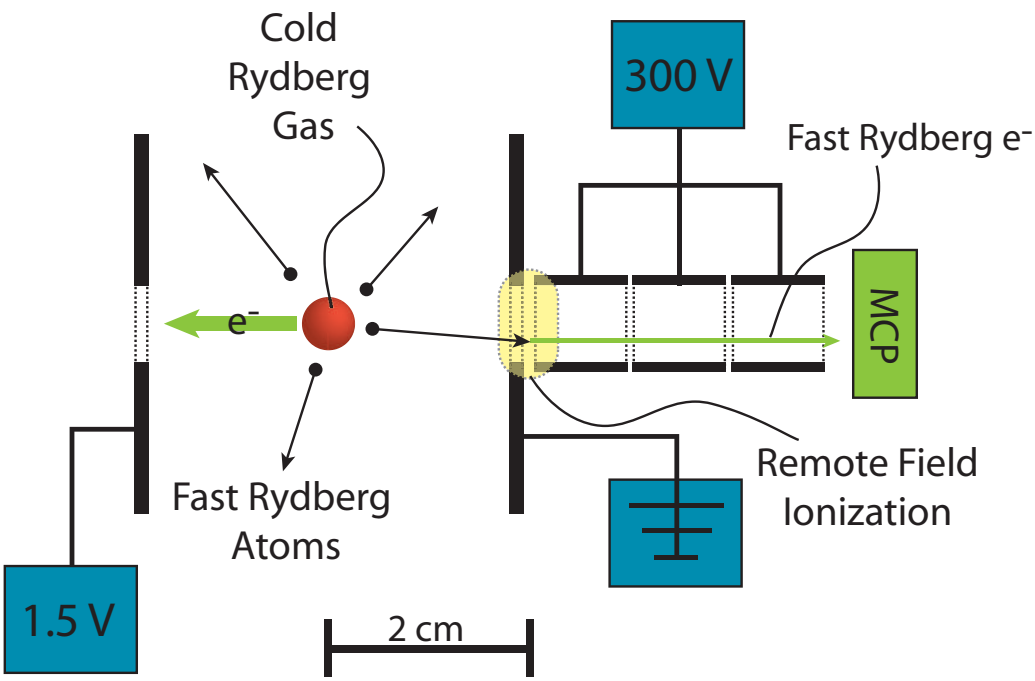

Figure 2.1: Experimental setup for time-of-flight measurement. A fraction of the fast Rydberg atoms emitted from the cloud travel into the remote field ionization region (shown in shaded yellow) between the grounded electrode and the first extraction electrode. Rydberg atoms which enter this region are field-ionized, and the resulting electrons are directed onto a micro-channel plate detector and counted.

state is higher to nD-states than nS-states.

Figure 2.1 shows the apparatus used to measure time-of-flight distributions of the Rydberg atoms emitted from the cold Rydberg gas. Fast Rydberg atoms created in the gas travel 2 cm from the cold Rydberg gas to a remote field ionization region located between the grounded electrode and the first extraction electrode. The region has an aperture of 1 cm such that the solid angle subtended by the remote field ionization region with respect to the cold Rydberg gas gives a detection efficiency of about 2 %. Using relaxation calculations, we estimate the electric field in this region to be $\approx$ 400 V/cm, which is strong enough to ionize low-angular-momentum Rydberg atoms down to $n = 30$ and high-angular-momentum atoms down to $n = 42$. Electrons resulting from Rydberg atoms ionized in this region are then counted by a micro-channel plate detector located approximately 10 cm away. A photon counter

then records the pulses from the micro-channel plate over a 0.5 to 1 ms wide window with variable delay.

From earlier experiments [30] it is known that thermal ionization of high-angular-momentum Rydberg atoms produces time-delayed electrons up to tens of milliseconds after the creation of the Rydberg gas. To ensure that such time-delayed electrons could not migrate from the atom cloud location into the remote field ionization region and produce a signal that could be mistaken for a signal from fast Rydberg atoms, a bias voltage of 1.5 V is applied to the electrode on the left of the cold Rydberg gas in figure 2.1. The resultant electric field slightly over-compensates the fringe electric field produced by the extraction electrodes at the location of the atom cloud, leading to a weak net field of ≈ 0.2 V/cm (pointing from left to right in figure 2.1). This field pulls electrons generated by time-delayed thermal ionization of slow Rydberg atoms toward the leftmost electrode so that the signal measured in the remote field ionization region is solely due to fast Rydberg atoms.

2.2.2 Experimental Results

Figure 2.2 shows typical time-of-flight data for $n_0 = 90$. Since the distance traveled by the atoms from the cold Rydberg gas to the detection region is $L = 2$ cm, the velocity distribution $P_V(v)$ of the detected fast Rydberg atoms, shown in figure 2.2(b), can be calculated from the time-of-flight data $P_T(t)$, shown in figure 2.2(a), using the relation $P_V(v) = P_T(\frac{L}{v})\frac{L}{v^2}$. The center of weight of the velocity distribution of the detected fast Rydberg atoms is found to be slightly less than 5 m/s, and the width of $P_V(v)$ about 5 m/s. The corresponding kinetic-energy range exceeds that of Rb atoms in a magneto-optical trap (velocity ~ 0.20 m/s) by a factor of about 600. The precise distance L from the MOT to the location in the remote field ionization region where the fast Rydberg atoms ionize is known to an accuracy of ± 5 mm.

This corresponds to an uncertainty in the center of weight of the velocity distribution of ±1.25 m/s. The the center of weight of the velocity distribution from figure 2.2 agrees well with the 7 m/s velocity estimated in section 2.1 from the classical calculations by Robicheaux [33], and the shapes of simulated and measured velocity distributions are very similar. These results are consistent with the notion that the fast Rydberg atoms are a product of binary collisions between two Rydberg atoms. This assessment is supported by state-selective field ionization data (see figure 2.4) and trends in the number of fast atoms detected versus density (see figure 2.5).

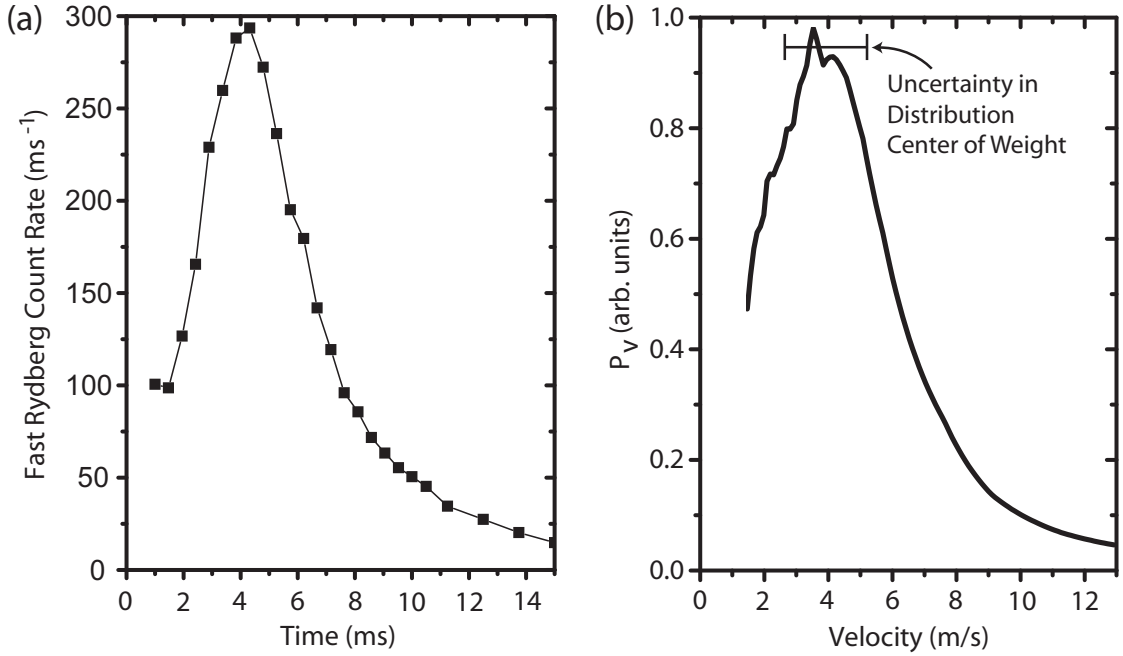

Figure 2.2: Time-of-flight (a) and velocity distribution (b) of Rydberg atoms emitted from a cold Rydberg-atom gas with initial principal quantum number $n_0 = 90$, central Rydberg atom density 1.4×10^8 cm^{-3} and Rydberg atom number 3×10^5. The time-of-flight t is the elapsed time between the Rydberg excitation pulse and the detection of the Rydberg electron by the MCP detector.

The most probable time of flight in figure 2.2 is 4 ms, which exceeds the natural lifetime of most Rydberg states. To explain this apparent conflict, we consider the effect of radiative decay and thermal ionization of fast Rydberg atoms prior to detection. For $n_0 = 90$, the principal quantum numbers of the fast Rydberg atoms

are expected to be in the range $45 \lesssim n \lesssim 65$, peaking around $n = 60$ [33]. Also, based on the field ionization data presented in figure 2.4 below we assume that the Rydberg-atom products of Penning-ionizing collisions typically are in high-angular-momentum states. Dipole selection rules allow atoms in high-angular-momentum states to only undergo transitions to other high-angular momentum states, so these atoms remain in Rydberg states for much longer than the lifetime of the initial high-angular-momentum state.

To obtain a quantitative estimate of the fraction of detectable atoms that reach the remote field ionization region, we have simulated the evolution of an ensemble of $n = 60$ Rydberg atoms with initially random angular momenta, weighted $\propto (2l + 1)$ and prepared in a 300 K radiation field, using a rate equation calculation developed previously [39]. We find that 4 ms after excitation about 80 % of the atoms still reside in detectable states ($n \gtrsim 35$ in our case). Therefore, under the conditions of figure 2.2, most of the fast Rydberg atoms survive until detection, and our TOF method yields good representations of the velocity distribution of fast Rydberg atoms produced in Rydberg-Rydberg collisions.

The product Rydberg states of Penning ionization are distributed over a certain n-range. A subtle consequence of radiative decay or ionization is that we preferentially measure the velocities of the longer-lived, higher-n portion of the distribution and lose more of the shorter-lived, lower-n portion. Since it is likely that atoms produced with below-average n have above-average velocities (because of generally larger energy exchanges in the Penning collision process), preferential detection of high-n atoms distorts the measured velocity distribution. For the case $n_0 = 90$, we expect $45 \lesssim n \lesssim 65$. Using the simulation discussed in the previous paragraph, we find that this n-range corresponds to survival probabilities ranging from about 66 % at $n = 45$ to

86 % at $n = 65$. Since the width of this percentage range is quite small, for $n_0 = 90$ the difference between measured and actual velocity distributions of the fast Rydberg atoms is deemed minimal. However, we found that the estimated spread in survival probabilities of product atoms increases considerably with decreasing n_0. Therefore, we have limited most studies in this paper to large values of n_0 (namely 90 and 75).

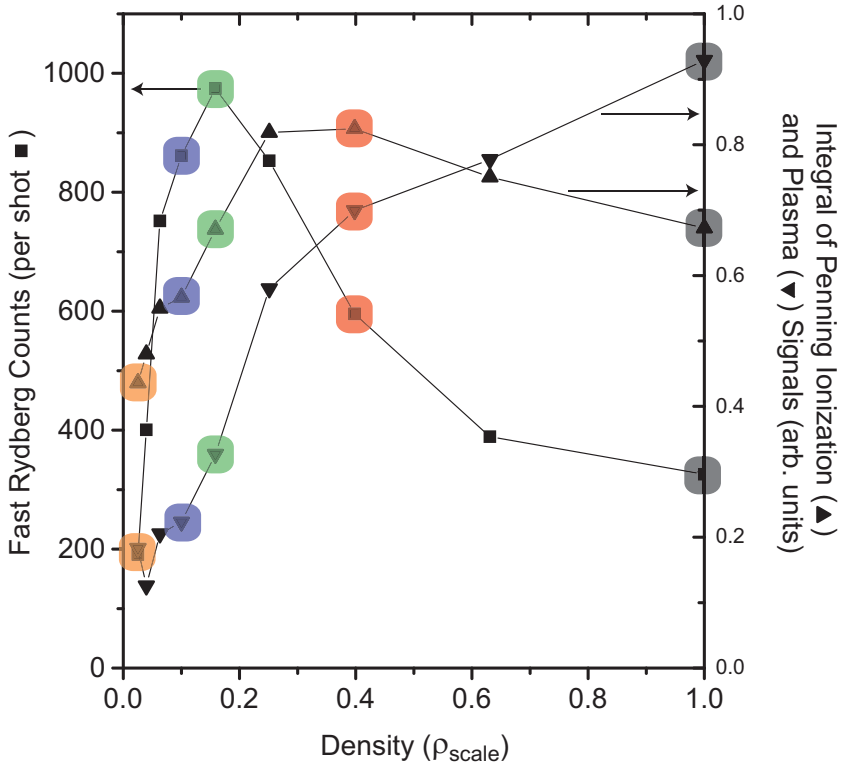

Figure 2.3: Total production of fast Rydberg atoms (■) vs initial Rydberg atom density ρ at $n_0 = 90$, where $\rho_{\text{scale}} = 9 \times 10^8$ cm^{-3} is a convenient density unit. The production of fast Rydberg atoms is compared with integrated Penning ionization (▲) and plasma (▼) signals obtained from state-selective field ionization spectra. For the color-highlighted data points, the corresponding field ionization spectra are shown in figure 2.4.

We have studied the dependence of fast Rydberg atom production on the initial Rydberg atom density (■ in figure 2.3). Fast Rydberg atom production is determined by summing the MCP counts for a time-of-flight scan at a particular density over all times. At low densities, we observe a rapid increase of fast Rydberg atom production, while at the highest densities the production of fast Rydberg atoms is suppressed.

Optimal production is observed at some intermediate density.

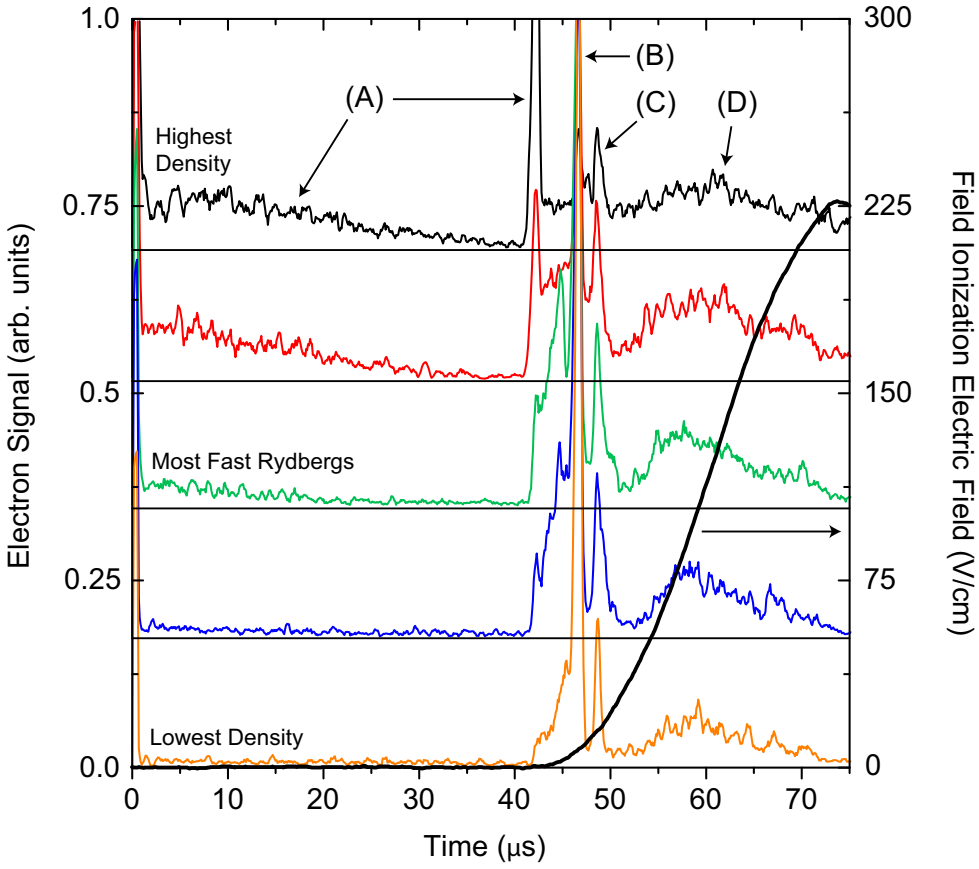

Figure 2.4: Field ionization spectra for $n_0 = 90$ and Rydberg atom densities colored coded with corresponding data points in figure 2.3. The Rydberg gas is excited at $t = 0$, and the field ionization pulse (thick line) is applied between 40 μs$< t \lesssim 75$ μs. Characteristic state selective field ionization signatures: (A) plasma electrons, (B) initial state, (C) ℓ-mixing, (D) Penning ionization.

In order to understand the density dependence of fast-Rydberg-atom production, we have examined state-selective field ionization spectra (see figure 2.4) of cold Rydberg gases for various densities at which time-of-flight measurements were taken (color coded with corresponding data points in figure 2.3). During a Penning ionizing collision, one of the Rydberg atoms undergoes a transition into a more deeply bound state with $n \lesssim n_0/\sqrt{2}$ and presumably high angular momentum. The de-excited atoms should produce a broad FI signal at electric fields of order ten times the ionization electric field of the initial state, because the ionization electric field

scales as n^{-4} and because high-angular-momentum atoms ionize at fields up to four times higher than those for low-angular-momentum atoms. The broad field ionization signal labeled "D" in figure 2.4 covers the expected ionization electric field range of the de-excited product atoms of Penning ionization. The net Penning ionization signal (▲ in figure 2.3), obtained by integrating over the "D"-signatures in figure 2.4, can be compared with the production of fast Rydberg atoms (■ in figure 2.3). Both quantities rapidly increase with density at low densities, exhibit broad maxima at intermediate densities values, and decrease with density at high densities. These similarities suggest that Penning-ionizing collisions lead to the production of fast Rydberg atoms. At low densities, the Penning-ionization and fast-Rydberg signals steadily increase, because with increasing density it becomes increasingly likely that two atoms are sufficiently close to each other to "snap together" and undergo the reaction in equation 2.1. As the density significantly exceeds the density of optimal production of fast Rydberg atoms, the Rydberg gas increasingly evolves into a plasma, as evidenced by the free-electron signatures "A" in figure 2.4. Electron-Rydberg-atom collisions in the plasma cause the Rydberg atoms to ionize or to undergo transitions to lower Rydberg states that ionize at higher electric fields than are present in the remote field ionization region [7]. We believe that both of these effects contribute to the detection of weaker Penning-ionization signatures in field ionization spectra and fewer fast Rydberg atoms at high densities.

The Penning-ionization signature is correlated with field ionization signatures of l-mixing (signal "C" in figure 2.4). Therefore, it seems likely that many Rydberg atoms first acquire large permanent electric dipole moments due to l-mixing collisions before undergoing Penning-ionizing collisions [7]. This sequence of processes appears reasonable because polar (high-l) atoms interact via dipole-dipole forces that are

stronger than the van-der-Waals forces acting between the (initially) non-polar low-l atoms as discussed in section 2.1.

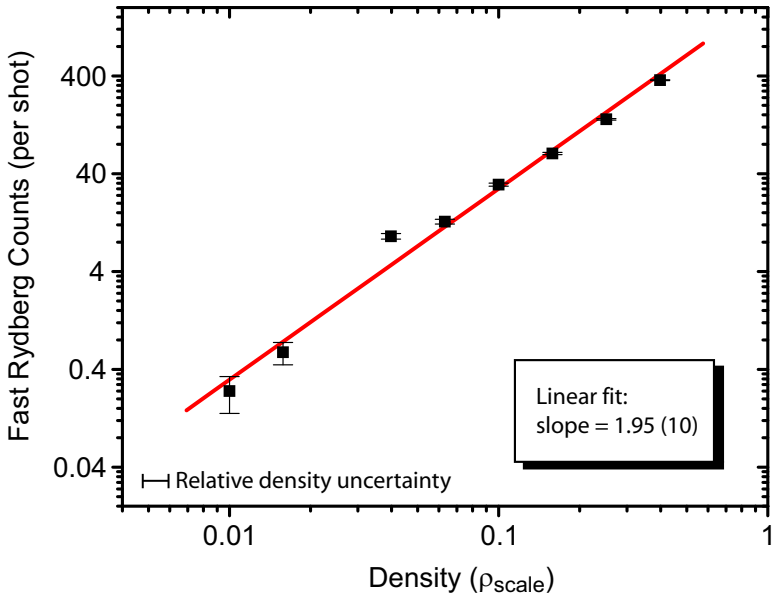

Figure 2.5: Total production of fast Rydberg atoms vs initial Rydberg atom density ρ in the low-density limit at $n_0 = 75$, where $\rho_{\text{scale}} = 3 \times 10^7$ cm^{-3} is a convenient density unit. A constant background of 17 counts was subtracted from the data set to compensate for dark counts on the MCP. The uncertainty for these counting measurements arises mainly from statistical noise which is $\approx \sqrt{N}$.

By examining the production of fast Rydberg atoms at low densities, the number of fast Rydberg atoms produced should possess a simple power law dependence on density. At higher densities, secondary effects, such as multiple electron collisions, tend to alter the fast Rydberg atom detection efficiency in a highly nonlinear way. Figure 2.5 shows a log-log plot of total fast Rydberg counts vs density for very low densities. The uncertainty for the number of Rydberg atoms detected stems mainly from the statistical noise proportional to the square root of the total number of counts and is indicated by the vertical error bars. The densities plotted on the x-axis are scaled by a density ρ_{scale}, which is accurate to within a factor of two. However, the uncertainty of a given density relative to the other densities in the plot is less than 20 %. The uncertainty in the relative densities arises mainly from the shot-to-

shot fluctuations in the 480 nm pulsed dye laser intensity. Assuming that the density fluctuates in proportion to the intensity, the relative uncertainty of each density value plotted in figure 2.5 is approximately given by $1/\sqrt{N_{\text{shots}}}$, where $N_{\text{shots}} = 25$ is the number of shots over which the number of fast Rydberg atoms was averaged. A linear fit using a least squares method to determine the slope of the line (drawn in red in figure 2.5) yields an experimentally determined exponent for the low-density power law of 1.95 ± 0.1. This exponent is close to two, indicating that the production of fast Rydberg atoms indeed results from binary collisions between Rydberg atoms, such as Penning ionization.

2.2.3 Discussion of Results

Time of flight data taken was taken for initial principal quantum numbers $n_0 = 90$, 75, 60, and 45. As n_0 was decreased from 90 to 45, the optimal yield of fast Rydberg atoms steadily decreased by about a factor five, while the velocity distributions remained approximately the same. The signal decrease can be qualitatively explained as a consequence of radiative decay and thermal ionization [39], which cause a decrease of the survival probability of the Rydberg-atom products of equation 2.1 from about 85% at $n = 60$ to less than 10% at $n = 20$. The fact that we observe essentially n_0-independent velocity distributions contradicts the simulations in Ref [33], where it is found that the velocities of the fast Rydberg atoms should scale as $1/n_0$. This discrepancy can partially be explained by the n-dependence of the survival probabilities of the product states in our time-of-flight experiment. An interesting possibility to further explain the discrepancy is that at lower n_0 we may increasingly observe "van de Graaf" type collisions that result in product velocities that are actually lower than those calculated for Penning ionization [33]. In these predicted collisions, the Rydberg atoms initially approach each other on an attractive dipole potential.

During the collision, the Runge-Lenz vectors of the Rydberg atoms precess in such a way that the dipole potential becomes repulsive. In this process, both atoms remain bound and gain kinetic energy from the collision because the internal states of the atoms change during the collision. In any case, we cannot distinguish between the "van de Graaf" type and Penning ionizing collisions in our experiment.

Fast Rydberg atoms could also form by three-body recombination in dense, expanding plasmas; however, this mechanism does not significantly contribute to these results. First, Rydberg atoms formed by three-body recombination are expected to have velocities ~ 50 m/s [40], while our data indicate an average velocity of only ~ 5 m/s and a rapid drop-off at velocities above ~ 10 m/s (see figure 2.2). Second, the signal we observe already appears at low densities, where it scales like a binary collision effect (see figure 2.5) and where the Rydberg gas does not evolve into a plasma. In contrast, Rydberg-atom formation via three-body recombination presumably will exhibit a threshold behavior, because the evolution of the Rydberg gas into a plasma proceeds via an ionization avalanche [41, 42]. In section 2.3, we present preliminary data from a similar time of flight experiment detecting fast Rydbergs formed by three-body recombination in expanding plasmas.

To summarize, we have performed time of flight measurements on Rydberg atoms emitted from a cold Rydberg gas. We have characterized the velocity distribution of these atoms, and found that the atoms have acquired a factor of ≈ 600 in kinetic energy. Furthermore, we have correlated the production of these fast atoms with Penning ionization. While large parts of our results agree with simulations [33], it is presently not clear why for small n_0 the experiments show lower atom velocities than the simulations.

2.3 Fast Rydberg Atoms in Expanding Ultracold Plasmas

At high densities, cold Rydberg-atom gases have also been found to evolve into cold, neutral plasmas [41, 42]. Such plasmas have also been created directly by excitation beyond the photo-ionization threshold, and have been studied extensively from both a theoretical and experimental perspective [9, 43–47]. Rydberg atoms are formed in these plasmas presumably via three-body recombination [40] at velocities in the range of 50 m/s. In this section, we discuss preliminary experiments using the time of flight technique discussed in the previous section to examine the formation of fast Rydbergs atom in expanding plasmas.

2.3.1 Three-body Recombination

Three-body recombination occurs when an ion collides with two electrons, resulting in an electron and ion forming a bound atom in a Rydberg state. The remaining electron conserves energy and momentum in the collision. The process can be represented symbolically as

$$ion + 2\mathrm{e}^- \rightarrow \mathrm{Ryd}(n) + \mathrm{e}^- \tag{2.5}$$

The process has been examined in numerous theoretical considerations [48–50], which have resulted in the rate equations for this process of the form

$$R_3 = C \times n_\mathrm{e}^2 n_\mathrm{ion} v_\mathrm{e} b^5 \tag{2.6}$$

where $v_\mathrm{e} = \sqrt{k_\mathrm{B} T_\mathrm{e}/m_\mathrm{e}}$ is the thermal velocity of an electron and $b = e^2/(4\pi\epsilon_0 k T_\mathrm{e})$ is the distance of closest approach where the thermal energy of the electron equals the Coulomb repulsion potential between two electrons. In reference [48], $C = 0.07$ for the case of a magnetized plasma ($B \rightarrow \infty$). For the the magnetic field free case, $C = 0.76$ is an order of magnitude larger. In reference [51], C ranges from

≈ 0.1 to 0.12 for magnetic fields in the 3 to 6 T range. From equation 2.6, we can see that the three-body recombination rate R_3 scales $\propto T^{-9/2}$, which would tend to make it the dominant recombination process at low temperatures like those found in ultracold plasmas. Experiments measuring the rate of Rydberg atom formation in these systems [40, 52] have reported rates significantly smaller than those predicted by equation 2.6. Low-temperature corrections to the rate formulas are addressed in references [53, 54].

Three-body recombination is important in the evolution of ultracold plasmas. The recombination removes one electron from the plasma and increases the kinetic energy of the second electron by the binding energy of the new Rydberg atom. Subsequent collisions between the Rydberg atom and plasma electrons can result in de-excitation of the Rydberg atom and further heating of the electronic component of the plasma. This heating of the electronic component increases plasma expansion velocities [45]. Along with disorder-induced heating resulting from the initially random photo-ion and electron distributions [55, 56], this heating presents challenges to observing strong-coupling [57] in these neutral plasma systems.

Current cold anti-hydrogen experiments [58, 59] rely on three-body recombination of antiprotons and positrons to produce antihydrogen in antimatter plasmas. The two-component antimatter plasmas are confined in nested penning traps which use a strong magnetic field to confine the particles transverse to the field and an electrostatic potential for longitudinal confinement. In our lab, we have created and trapped plasmas by photo-ionizing ^{85}Rb contained in a variation of this type of trap [60]. This trap has the unique ability to simultaneously trap two-component plasmas [60], Rydberg atoms [16], and ground state atoms [61] (which can be laser-cooled as well). Preliminary experiments involving three-body recombination in strongly-magnetized

plasmas have been performed in this trap [62], and work continues in this area.

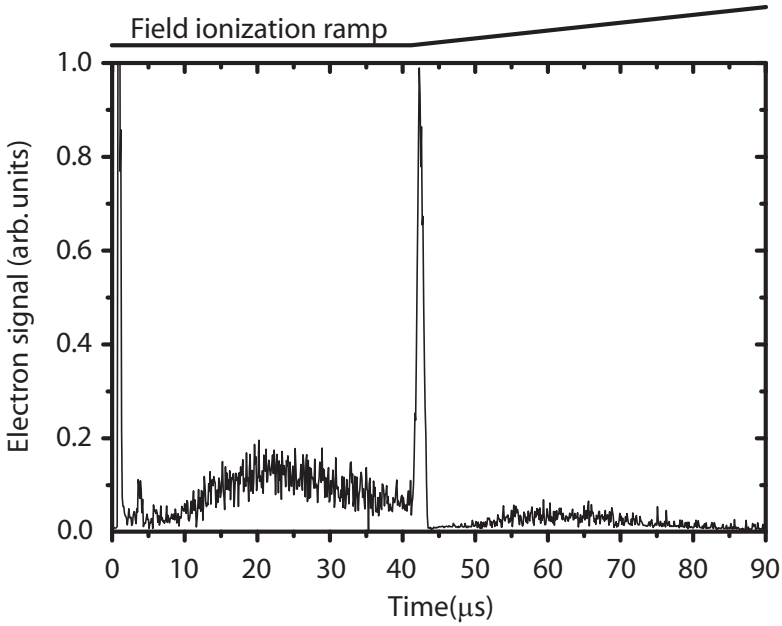

Figure 2.6: Field ionization spectrum of an ultracold plasma (initial ion density around 10^9 cm^{-3}) showing evidence of three-body recombination.

2.3.2 Experimental Results

Figure 2.6 shows a field ionization spectrum of an ultracold plasma (initial ion density around 10^9 cm^{-3}). Near $t = 0$ the ultracold plasma is created by photo-ionizing atoms collected in a magneto-optical trap. The excitation proceeds in a fashion similar to that described in section 2.2 except that the atoms are created at or above the single-atom, field free ionization potential. For atoms excited from the $5P_{3/2}$ state, the ionization threshold corresponds to photons with wavelength $\lambda \approx 479.1$ nm. In an experiment, the ionization threshold is determined by stray electric fields that can field ionize fragile high-lying Rydberg states and density, as interactions lead to continuum lowering. To obtain the data in figure 2.6, the photo-ionization laser was tuned to $\lambda = 479.2$ nm, which lies above the ionization threshold for the given experimental conditions.

After photo-ionization, the ultracold plasma is allowed to evolve for 40 μs before

applying a state selective field ionization ramp, which is applied for 40 μs $\leq t \leq$ 90 μs. During the field free expansion time ($t \leq 40$ μs), we see the characteristic signature of electrons emitted from the expanding ultracold plasma [9]. At $t = 40$ μs, the sharp peak of electron signal results from the removal of electrons remaining in the positive space-charge potential of the ion cloud. The broad electron signal arriving during the electric-field ramp corresponds to bound Rydberg atoms created in the expanding plasma presumably via three-body recombination as discussed above.

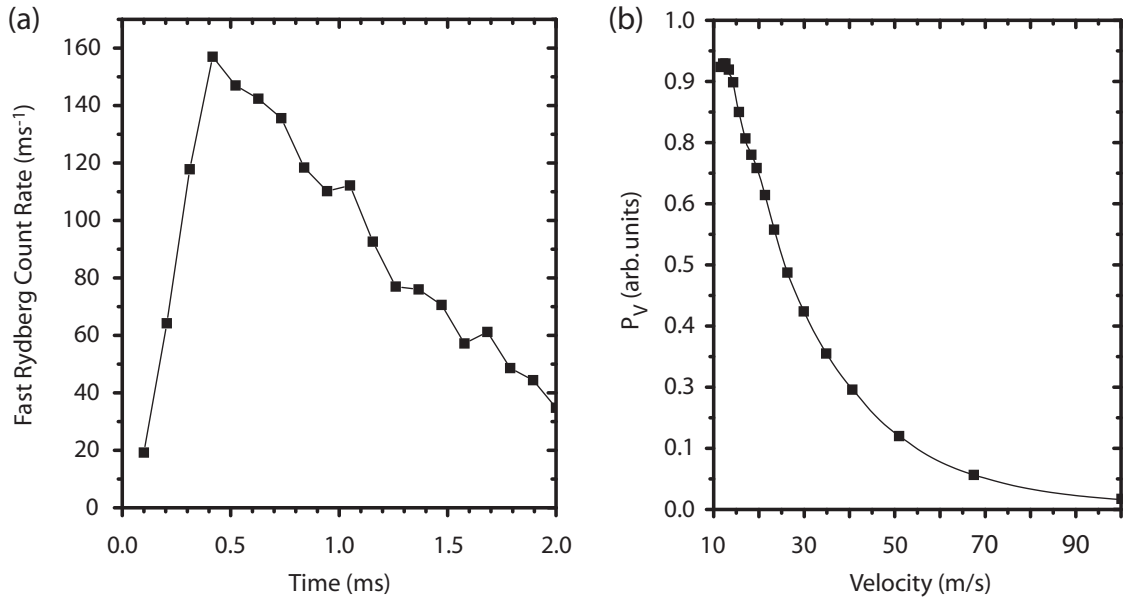

Figure 2.7: Time of flight data (a) and calculated velocity distribution (b) of fast Rydberg atoms emitted from an expanding ultracold plasma.

Figure 2.7(a) shows time of flight data obtained using the technique illustrated in figure 2.1. In this case, an ultracold plasma is created instead of a cold Rydberg gas, the bias voltage is 900 mV (instead of 1.5 V), and the segmented guide tubes are held at 350 V (instead of 300 V). Some of the fast Rydberg atoms formed in the expanding ultracold plasma are emitted into the solid angle subtended by the remote field ionization region and their detection is recorded as a function of delay time from the creation of the ultracold plasma. The most probable arrival time of

Rydberg atoms at the remote field ionization region is about 500 μs. The ultracold plasma has a lifetime on the order of 50 μs, which is a factor of ten smaller than the most probable arrival time. Thus, we consider the arrival time relative to the creation of the ultracold plasma to approximately measure the time of flight of the Rydberg atom over the $\approx$ 2 cm flight distance (see figure 2.1). The most probable arrival time corresponds to velocities in the 40 m/s range, which is consistent with ion expansion velocities in ultracold plasmas [9, 50].

The velocity distribution calculated from the time of flight data in figure 2.7(a) is shown in part (b) of the figure. From this velocity distribution, we can see that Rydberg atoms are preferentially formed at lower velocities. This is consistent with the scaling laws for three-body recombination (see equation 2.6). Recombination rates will be highest at places in the ultracold plasma where densities are the highest. The highest densities in the expanding ultracold plasma occur at the center of the plasma where ions are moving the slowest. These results are in qualitative agreement with the simulations of Rydberg atom formation in expanding plasmas in Pohl et. al. [63] (see figures 4 and 5 in this reference).

Figure 2.8(a) shows the total number of fast Rydberg atoms detected as a function of the photo-ionizing laser's wavelength λ. The excess photon energy above the ionization potential corresponds to energy imparted to the plasma per photon ($\Delta E = hc[\lambda^{-1} - \lambda_{\text{threshold}}^{-1}]$) by the photo-ionization process. Assuming the electrons receive most of the excess energy, the wavelength range in figure 2.8 corresponds to an initial electron temperature range of 10 to 600 K. The weak trend of reduced fast Rydberg atoms detected with increasing photon energy (decreasing wavelength) does not seem at all consistent with the $T_{\text{e}}^{-9/2}$ scaling predicted for three-body recombination, which would predict a huge change in fast Rydberg production over this excess photon

energy (initial electron temperature) range. The electronic component cools as it drives the expansion the plasma [52], which could make the rates similar for the various wavelengths despite the disparity in the initial electron temperature.

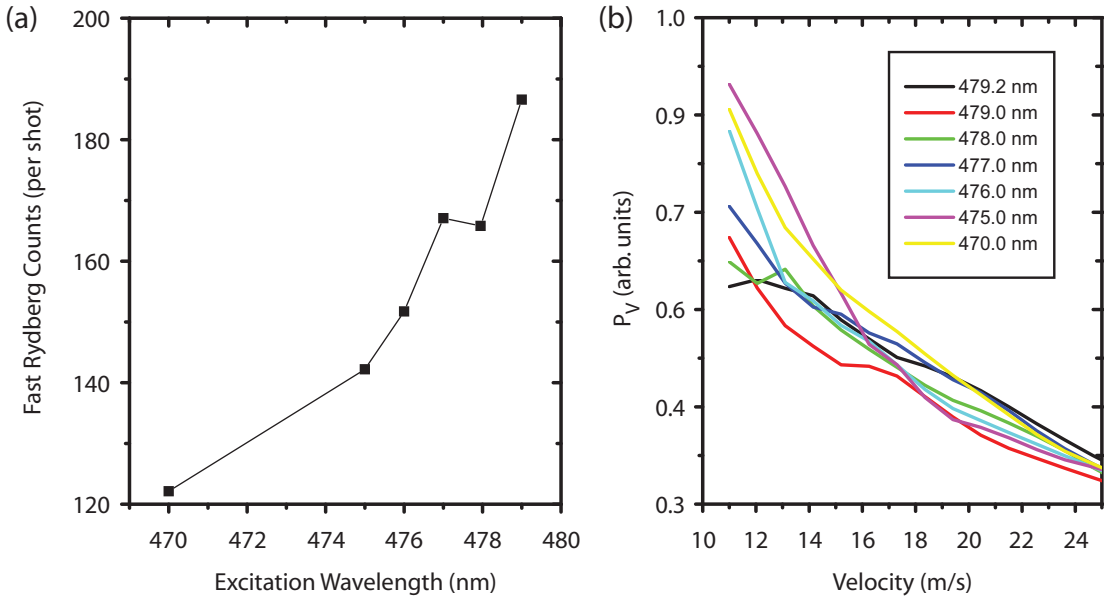

Figure 2.8: Total fast Rydberg atoms counted (a) and corresponding velocity distributions calculated from time-of-flight data (b) of fast Rydberg atoms formed in an expanding ultracold plasma.

Higher energy plasmas would expand more rapidly [50]. Thus, one might expect to see increasingly higher fast Rydberg velocities at lower ionizing wavelengths. This expectation is not reflected in the fast Rydberg atom velocity distributions plotted in figure 2.8(b), which are calculated from time-of-data taken at various photoionization wavelengths. Though the trend is not perfect, the velocity distributions for lower-wavelength (higher plasma energy) data seem to favor lower velocities than corresponding distributions for data at higher wavelengths. A major difficulty in interpreting the data is that it is unclear what fraction of the Rydberg atoms formed in the plasma at a particular velocity are in detectable states when they arrive at the remote field ionization region. For example, the simulations in reference [63] predict that a significant fraction of Rydberg atoms formed in the expanding plasma reside

in states the are too deeply bound to be ionized in the remote field ionization or too short-lived to survive the time-of-flight. An experiment that could probe the spatial Rydberg-atom distribution in real time would be useful in overcoming this problem. Such an experiment, which utilizes a needle as a field ionization electrode to project a magnified image of the charge distribution on a micro-channel plate, is discussed in section VI.

To summarize the results of this section, we have made time-of-flight measurements detecting fast Rydberg atoms emitted from expanding ultracold plasmas. The velocity distributions calculated from these measurements agree qualitatively with expectations based on the typical ion expansion velocities and three-body recombination density scaling, which predicts preferential formation at lower velocities. More detailed interpretation of trends with photo-ionization energy are difficult because of the complex nature of the evolution of these plasmas and limitations of the apparatus. Future experiments using another apparatus being developed in our lab (see discussion in chapter VI) could provide more insight into this important physical process.

CHAPTER III

Ponderomotive Interaction with Rydberg Electrons

In this chapter, we discuss the theoretical framework for the ponderomotive interaction of an optical field with a Rydberg electron. The starting point for this description is the classical interaction of a free electron with a rapidly oscillating, spatially inhomogeneous electromagnetic field that results in the so-called ponderomotive force on the electron directed towards regions of low intensity. One might anticipate a similar interaction between an oscillating field and the Rydberg electron since a Rydberg electron is essentially a quasi-free electron bound weakly to an ion through their Coulomb interaction. This can be made rigorous by considering the various timescales over which the relevant coordinates for a Rydberg atom in an optical field evolve. Through the application of the Born-Oppenheimer approximation [25], it can be shown that the Rydberg electron experiences a ponderomotive shift in its energy in proportion to the intensity of an applied optical field. Forces on the Rydberg atom result from spatial inhomogeneities in the optical field. These inhomogeneities also cause the ponderomotive shift to be Rydberg state dependent. Finally, we discuss schemes for spectroscopically probing the ponderomotive interaction for the Rydberg electron.

3.1 Ponderomotive Potential for a Free Electron

In this section, we discuss the ponderomotive potential for free a electron in an inhomogeneous electromagnetic field. A free electron in an oscillating electric field experiences a ponderomotive energy shift equal to its time-averaged kinetic energy. For applied electric fields of the form $\mathbf{E}(\mathbf{r},\ t) = \mathbf{E}(\mathbf{r})e^{i\omega t}$, the ponderomotive energy can be expressed as [64],

$$W^{\mathrm{Q}} = \frac{e^2|\mathbf{E}(\mathbf{r})|^2}{4m_{\mathrm{e}}\omega^2}\ , \tag{3.1}$$

where and $-e$ and m_{e} are the electronic charge and mass, respectively. The potential is obtained from classical considerations, and this form will be taken for the quantum mechanical interaction potential describing the effect of a ponderomotive potential on a Rydberg electron.

Spatial inhomogeneities in the applied electric field lead to forces on charged particles. For an optical standing wave, the potential is periodic and represents a potential from which electrons can be scattered via the Kapitza-Dirac effect. Rainbow scattering [21], Bragg scattering [22], and diffraction [23] of electrons from high intensity laser pulses have all been observed experimentally. In studies of laser-plasma interactions, the intensity gradients in the Guassian profile of a laser beam passing through a plasma causes electrons to be expelled from regions of high intensity (electron cavitation [65]). Ponderomotive effects in plasmas also form the basis of new charged particle accelerator methods, in which electrons can be accelerated in wake-field plasma waves created by laser pulses [10, 11]. On the low intensity side, the ponderomotive force is used to create the Paul trap for ions [12, 13]. The application of high frequency voltage signals to electrodes producing inhomogeneous electric fields, *e.g.* spherical quadrupole, produces a ponderomotive force on the

charged particles directed toward regions of smaller fields.

To gain some physical insight into the nature of the ponderomotive interaction between an oscillating electromagnetic field and a free electron, we examine the case of particular experimental interest of an electron in an applied optical standing wave, such as that which could be produced by a retro-reflected laser beam. The classical equation of motion for such an electron whose position $\mathbf{r}$ in a electric field $\mathbf{E}$ and a magnetic field $\mathbf{B}$ is given by the Coulomb and Lorentz forces such that,

$$m\ddot{\mathbf{r}} = -e(\mathbf{E} + \dot{\mathbf{r}} \times \mathbf{B}). \tag{3.2}$$

The electric and magnetic fields appropriate for an a standing wave with a propagation axis along the x-direction and the electric field polarized along the y-direction can be written

$$\begin{aligned} \mathbf{E}(\mathbf{r},\, t) = E_{\mathrm{y}}(x,t)\hat{y} &= E_{0\mathrm{y}}\left[\cos(\omega t - kx) + \cos(\omega t + kx)\right]\hat{y} \\ &= 2E_{0\mathrm{y}}\cos(\omega t)\cos(kx)\hat{y} \end{aligned} \tag{3.3}$$

$$\begin{aligned} \mathbf{B}(\mathbf{r},\, t) = B_{\mathrm{z}}(x,t)\hat{Z} &= -\hat{z}\int \frac{\partial E_{\mathrm{y}}}{\partial x}dt \\ &= \frac{2E_{0\mathrm{y}}}{c}\sin(\omega t)\sin(kx)\hat{z} \end{aligned} \tag{3.4}$$

This standing electromagnetic field is plotted in Fig 3.1. To solve equation 3.2 for the electrons motion in the field of a standing wave, we assume that the electron undergoes a driven oscillation (quiver motion) in the electric field. The resulting velocity (plotted in red in Fig. 3.1 and given in equation 3.6) is perpendicular to the magnetic field and possesses a relative phase which produces a nonzero time-averaged force along the axis of propagation normal to the standing wave planes. We begin by writing the equation of motion for the quiver motion of the electron in the oscillating

electric field:

$$\ddot{y} = -\frac{eE(x,t)}{m} = -\frac{e2E_{0y}}{m}\cos(kx)\cos(\omega t) \tag{3.5}$$

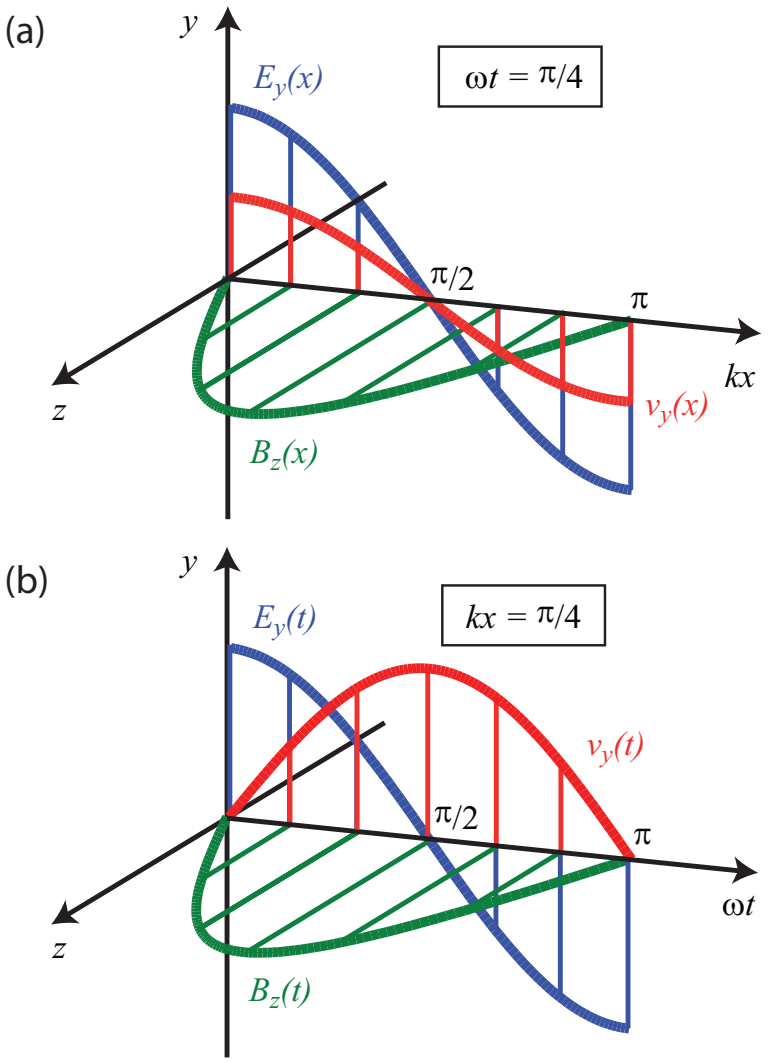

Figure 3.1: Electric field **E** (blue), magnetic field **B** (green), and velocity **v** of driven electron motion (red) in a standing wave for a point in time $\omega t = \pi/4$ (a) and a point in space $kx = \pi/4$ (b). Using the right-hand rule associated with the Lorentz force on the electron $-e\mathbf{v} \times \mathbf{B}$, these two plots can be used to understand key features of the dynamics of an electron in a standing wave light field.

Integrating with respect to time and assuming that $\dot{y}(0) = 0$, we solve for the velocity of the quiver motion,

$$\dot{y} = -\frac{2eE_{0y}}{\omega m}\cos(kx)\sin(\omega t). \tag{3.6}$$

The velocity of the quiver motion along the y-direction is set up perpendicularly to the magnetic field component of the standing wave from equation 3.4, which is along the z-direction. The result is a force perpendicular to the standing wave planes,

$$F_x = -e\dot{y}B = \frac{4e^2 E_{0\mathrm{y}}}{m\omega c}\sin^2(\omega t)\sin(kx)\cos(kx). \tag{3.7}$$

We compute the time average of this force over one period of the quiver motion which yields

$$\langle F_x\rangle_t = \frac{\omega}{2\pi}\int_0^{2\pi/\omega} F_x dt = \frac{2e^2 E_{0\mathrm{y}}}{m\omega c}\sin(kx)\cos(kx). \tag{3.8}$$

This time-averaged, spatially inhomogeneous force is nonzero and can be related to potential energy such that

$$W_{\mathrm{SW}}^{\mathrm{Q}} = -\int dx\langle F_x\rangle_t = \frac{e^2[2E_{0\mathrm{y}}\cos(kx)]^2}{4m\omega^2}, \tag{3.9}$$

which has the general form of a ponderomotive potential given in equation 3.1 after noting that $|\mathbf{E}(\mathbf{r})| = 2E_{0\mathrm{y}}\cos(kx)$ for the standing wave electric field of equation 3.3.

In solving equation 3.2 as outlined above, we have assumed that the first term in equation 3.2 is much larger than the second. Inserting equations 3.3 and 3.4 into 3.2, we find the amplitude of the electric field term is $e2E_{0\mathrm{y}}$, and the amplitude of magnetic term is $e2E_{0\mathrm{y}}\dot{y}/c$, which yields the condition $|\dot{y}/c| \ll 1$ for the validity of our asumption. Evaluating the amplitude of $\dot{y}$ in equation 3.6 for parameters typical of our experiments ($\lambda = \omega/c = 1064$ nm, $E_{0\mathrm{y}} = 1\times10^6$ V/m), we find $|\dot{y}| < 200$ m/s validating our assumption as to the relative strengths of the electric and magnetic forces.

Another quantity that will be of interest in subsequent discussions is the amplitude of the quiver motion of an electron in a ponderomotive standing wave lattice. We can calculate this amplitude y_0 by integrating $\dot{y}$ from equation 3.6 finding

$$y_0 = \frac{2eE_{0y}}{m\omega^2}. \tag{3.10}$$

For the experimental parameters listed in the previous paragraph, we compute the amplitude of the quiver motion to be about 2 pm.

From the form of equation 3.1, we see that the charged particles, regardless of the sign of the charge, are attracted to local intensity minimum in the applied electric field. For the standing wave in equation 3.9, charged particles would experience a ponderomotive force directed toward the nodes of the lattice. These points can be made graphically for the standing wave using figure 3.1. Here the standing wave fields from equations 3.3 and 3.4 are plotted as a function of x for a particlar instant in time (a) and as a function of t for a particular point in space (b). The velocity of an electron driven by the electric field is plotted in red. The force along the x-direction arises from the Lorentz force. Applying the right hand rule to the magnetic field and velocity plotted in figure 3.1(a), we can determine that the direction of the Lorentz force always points to the node of the electric field, which corresponds to the intensity minimum of the potential. If the sign of the charge is positive, the velocity solution given in the figure also changes sign, and we can infer that the potential is the same for both positively and negatively charged particles.

Examining figure 3.1 in a similar way, one finds that over the half temporal period plotted, the Lorentz force always points in the same direction. In the second half of the temporal period (not shown) the sign of the velocity and magnetic field both change such that the direction of the force remain the same as in the first half. This confirms that the force averages to a nonzero value over one optical cycle.

The ponderomotive potential can also be viewed as the time average kinetic energy of the charged particle oscillating in the applied field. Taking this view, we write down the kinetic energy by inserting equation 3.6 into the kinetic energy expression

$$W_{\mathrm{SW}}^{\mathrm{Q}} = \frac{\omega}{2\pi}\int_0^{2\pi/\omega} \frac{1}{2} m\dot{y}^2 dt = \frac{e^2[2E_{0\mathrm{y}}\cos(kx)]^2}{4m\omega^2},$$

which reproduces the correct form for the ponderomotive potential without explicitly appealing to the action of the magnetic field on the charged particle.

In this section, we have described the action of harmonically oscillating, spatially inhomogeneous electromgnetic fields on charged particles. In subsequent sections, we extend the discussion to the ponderomotive interaction between a Rydberg electron and an applied optical field.

3.2 Ponderomotive Potential for a Rydberg Electron

In this section, we outline the theoretical foundation for the ponderomotive interaction of an applied optical field and a Rydberg electron proposed in a paper by Dutta, et. al. [25] (see also reference [66] for an alternate treatment). There, they proposed forming an optical lattice for Rydberg-atom trapping using the ponderomotive interaction between a Rydberg electron and a standing wave light field, which they called a ponderomotive optical latttice.

A Rydberg atom is comprised of an electron that is weakly bound to an ionic core. The fact that the Rydberg electron is quasi-free suggests that its ponderomotive interaction would be similar to that of the free electron discussed in section 3.1. A Rydberg atom immersed in a optical field can be described by the three coordinates $\mathbf{R}$, $\mathbf{r}$, and ρ. The coordinate system is sketched in figure 3.2(a). $\mathbf{R}$ gives the position of the Rydberg atom center of mass, $\mathbf{r}$ is the relative coordinate between the Rydberg electron and the ionic core, and ρ is describes the quiver motion of the driven oscillation of the electron in the applied field.

The coordinates are chosen to reflect the various timescales of the evolution of the system shown in figure 3.2(b). The fastest evolving coordinate is the quiver coordinate ρ, which evolves at the frequency of the applied optical field (2.8×10^{14} Hz

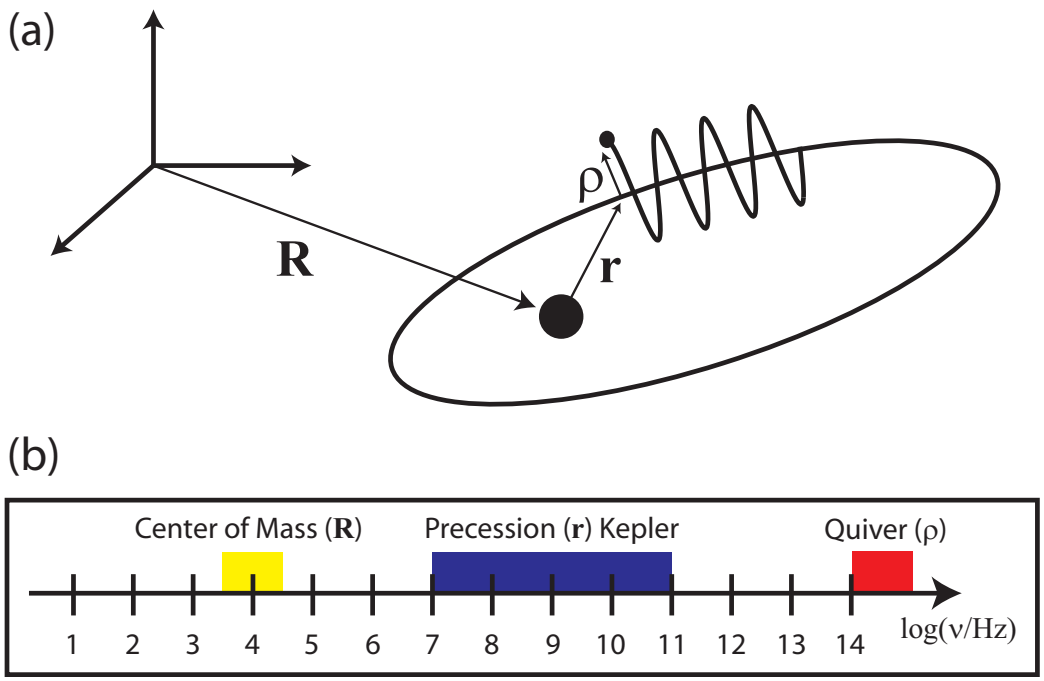

Figure 3.2: Relevant coordinates (a) and time scales (b) for a Rydberg atom immersed in an applied optical field.

for 1064 nm light). The coordinate for the relative motion of the Rydberg electron **r** evolves over a large range of timescales, the fastest of which is given by the Kepler frequency of the Rydberg electron (about 1×10^{11} Hz for $n = 40$). As a side note, some experiments involving the creation and manipulation of Rydberg electron wavepackets that exhibit classical orbiting behavior can be found in Maeda, et.al. [67].

In any case, the timescale of the quiver motion is shorter than that of the relative motion by a factor of 1000, which is enough to adiabatically separate the quiver motion from the orbital motion. Additionally, the amplitude of quiver motion of the electron is much smaller than the characteristic variation lengths of the atomic potential and external potentials. In the last section (see equation 3.10), we calculated the quiver amplitude for anticipated experimental conditions to be about 2 picometers. For an $n = 40$ Rydberg atom at half the radius of the Bohr orbit ($a_0 n^2/2$), the length over which the atomic potential varies by $10^{-4} \times$ 13.6 eV is ≈ 1 nm. Variations

in external potentials, such as those that might arise from gradients in the applied optical field, would vary over even larger length scales. Therefore on the timescale of the quiver motion, we can assume that the electron is quivering in a background potential $V_0(\mathbf{R}+\mathbf{r})$ composed of contributions from the atomic and external potentials evaluated at the average (over the quiver motion) position of the electron. The value of the constant background potential $V_0(\mathbf{R}+\mathbf{r})$ can be subtracted from the Schrödinger equation for the quiver motion, which yields

$$\left[-\frac{\hbar^2}{2m_\mathrm{e}}\nabla_\rho + e\rho\cdot\mathbf{E}(\mathbf{R}+\mathbf{r})\cos(\omega t)\right]\phi(\rho,\ t;\ \mathbf{r},\ \mathbf{R}) = i\hbar\frac{\partial}{\partial t}\phi\left(\rho,\ t;\ \mathbf{r},\ \mathbf{R}\right) \tag{3.11}$$

for the quiver wave function $\phi(\rho,\ t;\ \mathbf{r},\ \mathbf{R})$ where $\mathbf{r}$ and $\mathbf{R}$ are quasistatic parameters of the solution. Equation 3.11 is simply the time-dependent Schrödinger equation for a free electron in a plane wave with amplitude $\mathbf{E}(\mathbf{R}+\mathbf{r})$. The Volkov states [68, 69] are solutions for the $\phi(\rho,\ t;\ \mathbf{r},\ \mathbf{R})$ and the energies are given by the ponderomotive potential

$$W^\mathrm{Q} = \frac{e^2|\mathbf{E}(\mathbf{R}+r)|^2}{4m_\mathrm{e}\omega^2}\ , \tag{3.12}$$

With the adiabatic elimination of the quiver motion, the interaction between the Rydberg electron and an applied optical field can be treated by adding a static potential W^Q to the Hamiltonian of the Rydberg atom. This point verifies the initial intuition that the Rydberg electron would experience a ponderomotive shift in an applied light field like that of the free electron discussed in the previous section. The idea that a shift of the form given in equation 3.12 can be added to the atomic potential to describe the ponderomotive interaction is the starting point of setion 4.1, where driving transitions with a time-dependent ponderomotive perturbation to the Rydberg electron is discussed.

In the remainder of this section, we continue the discussion of Dutta, et.al. [25]

pertaining to the effect of a ponderomotive interaction on the evolution of the center of mass coordinate $\mathbf{R}$ and the formation of ponderomotive optical lattices. The expected order of magnitude for the evolution of the center of mass coordinate is tens of kilohertz. This is much slower than the Kepler evolution timescales of the relative motion. For Rydberg states that are sufficiently non-degenerate with other Rydberg states (energy splittings much greater than the ponderomotive shift of the Rydberg electron), the relative motion can be adiabatically separated from the center of mass coordinate. The low angular momentum states of the heavy alkalis satisfy this condition for many experimentally relevant laser field intensities. However, the high angular momentum states in the hydrogenic manifold have an $\approx n^2$ degeneracy. Small stray fields can mix these states creating energy level splittings of order 10 kHz (for an electric field of ≈ 1 mV/cm). This leads to evolution timescales for the relative coordinate that are of the same order as the expected evolution frequencies of the center-of-mass coordinate preventing simple application of a Born-Oppenheimer approximation. In this case, the application of appropriate electric and magnetic fields can lift the energy degeneracies of the hydrogenic states making them sufficiently non-degenerate for the adiabatic separation of the relative motion from the center-of-mass motion.

This point is important for a couple of reasons. First, the separation of variables and the ponderomotive potential for the center-of-mass coordinate that results is universally applicable to all Rydberg states. Further, one potential use for ponderomotive optical lattices is to suspend Rydberg atoms in high angular momentum circular states against gravity while making spectroscopic measurements of atomic properties. Circular states are desirable for spectroscopic efforts due to their long lifetimes and electric and magnetic field insensitivity, and have potential uses in

high-precision spectroscopy of the Rydberg constant [70].

Assuming that the appropriate fields have been applied in order to validate the Born-Oppenheimer approximation, the center-of-mass coordniate $\mathbf{R}$ can be considered a quasi-static parameter of the relative motion, yielding for the Schrödinger equation for the relative motion

$$\left[H_{\mathrm{F}} + W^{\mathrm{Q}}(\mathbf{R}+\mathbf{r})\right]\psi(\mathbf{r};\mathbf{R}) = W^{\mathrm{R}}(\mathbf{R})\psi(\mathbf{r};\mathbf{R}), \tag{3.13}$$

where H_{F} is the sum of the atomic Hamiltonian and the static-field-induced perturbations of the relative motion and $\psi(\mathbf{r};\mathbf{R})$ is the wavefunction for the relative motion. The solution of equation 3.13 yields energies $W_{\mathrm{j}}^{\mathrm{R}}(\mathbf{R})$ which form adiabatic potential surfaces which govern the evolution of the center-of-mass coordinate of a Rydberg atom in state $|j\rangle$. We can use nondegenerate perturbation theory to solve equation 3.13 for $W_{\mathrm{j}}^{\mathrm{R}}(\mathbf{R})$. The unperturbed Rydberg wavefunctions and the corresponding energies are defined by $H_{\mathrm{F}}\psi_{\mathrm{j}}^{0}(\mathbf{r};\mathbf{R}) = W_{\mathrm{j}}^{\mathrm{R0}}(\mathbf{R})\psi_{\mathrm{j}}^{0}(\mathbf{r};\mathbf{R})$. The energy difference $W_{\mathrm{j}}^{\mathrm{R}}(\mathbf{R}) - W_{\mathrm{j}}^{\mathrm{R0}}(\mathbf{R})$ is equal to the ponderomotive shift of the energy of Rydberg state $|j\rangle$ at location $\mathbf{R}$ and is given by

$$W_{\mathrm{j}}^{\mathrm{R}}(\mathbf{R}) - W_{\mathrm{j}}^{\mathrm{R0}}(\mathbf{R}) = \frac{e^2}{4m_{\mathrm{e}}\omega^2}\int d^3r|\mathbf{E}(\mathbf{R}+\mathbf{r})|^2|\psi_{\mathrm{j}}^{0}(\mathbf{r};\mathbf{R})|^2. \tag{3.14}$$

For low angular momentum states of the heavy alkalis, no external fields are needed to validate the adiabatic separation of relative and center-of-mass coordinates. In this case, the Rydberg wavefunctions $\psi_{\mathrm{j}}^{0}(\mathbf{r})$ and energies $W_{\mathrm{j}}^{\mathrm{R0}}$ are simply the eigenfunctions and eigenvalues of an atomic Hamiltonian $H_0 = V_{\mathrm{c}}(r) - 1/r$, where $V_{\mathrm{c}}(r)$ is a short-range potential consistent with the quantum defects of the desired atomic species. See table 1.1 for a list of quantum defects of ^{85}Rb.

Suppose a Rydberg atom is immersed in an applied optical field whose amplitude $|\mathbf{E}|$ does not vary appreciably over the extent of the atom's wavefunction. For this

case, the integral in equation 3.14 can be performed by evaluating the field amplitude at the location of the Rydberg atom's center of mass **R**. The energy shift of the Rydberg state in Equation 3.14 then reduces to the energy shift of a free electron in equation 3.1. As the extent of the Rydberg atom wavefunction increases to become appreciable compared to the spatial variation length of the applied field amplitude, the ponderomotive shift of the Rydberg level reflects a kind of spatial average of the light field weighted by the Rydberg wavefunction.

In either case, spatial inhomogeneities in the energy shift result in forces on the Rydberg atom. For a standing wave light potential, such as that formed by two laser beams propagating at a mutual angle, the periodic potential would form a ponderomotive optical lattice for Rydberg atoms [25]. A suitable geometry for holding Rydberg atoms against gravity in a one dimensional optical lattice is shown in figure 3.3. The lattice constant in this trap could be adjusted by varying α. For trap parameters using a wavelength of 1064 nm and single beam intensities of 500 W/cm^2, the trap depth is about 5 μK or 25 kHz. The trap depth scales with the intensity and wavelength squared, so higher trap depths are feasible by exploiting these parameters. However, to efficiently load photo-excited laser-cooled atoms into a ponderomotive optical lattice with these trap depths, subdoppler laser cooling techniques must be employed.

Holding Rydberg atoms in long lived, high-angular-momentum states against gravity could be used to verify the effectiveness of such a lattice. If the hold time is sufficient for untrapped atoms to fall from the detection regions, remaining atoms could be considered trapped. Another method for verifying the effectiveness of the lattice is comparing ionization rates for Rydberg atoms with and without the lattice. The lattice should inhibit collisions of the type discussed in section 2.1. Directly

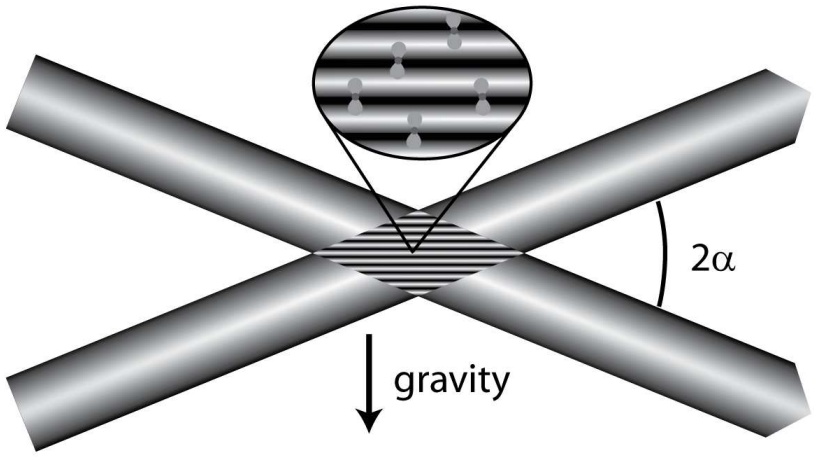

Figure 3.3: An appropriate geometry for forming a one dimensional ponderomotive optical lattice to hold Rydberg atoms against gravity.

imaging the atoms in the lattice using a spatially resolving field ionization techniques could also be used to verify the effectiveness of the lattice.

Since the application of the light field shifts the energy of the Rydberg states significantly, it should also be possible to spectroscopically probe the effects of the ponderomotive interaction with the Rydberg electron. The light shift of Rydberg states has been measured previously by examining the Rydberg excitation spectrum of rubidium atoms immersed in an intense, non-resonant optical field [24]. Spatial inhomogeneities in the applied optical field, such as the Gaussian intensity profile of a focused laser beam or a periodic standing wave formed from a retro-reflected laser beam, should have predictable and measurable effects on the spectroscopy of Rydberg atoms in these fields. In the remainder of this chapter, we discuss a variety of ways to use spectroscopy to probe the ponderomotive interaction in Rydberg atoms.

3.3 Spectroscopy of Rydberg Light Shift

In section 3.2, we discussed the ponderomotive shift of Rydberg energy levels and suggested using these shifts to spectroscopically probe the effect of a nonresonant

applied optical field on a Rydberg atom. In this section, we examine this possibility further from two perspectives, laser spectroscopy of Rydberg states proceeding from the ground state and microwave spectroscopy between two Rydberg states. In a homogeneous laser field, the ponderomotive shift of a Rydberg electron is the same for all Rydberg states, namely that of the free electron. Thus, the net frequency shift of a transition between to Rydberg states would be zero. However, if one compares the shift of the frequency of a Rydberg level relative to the ground state, the two are not equal in general and can in fact result in measurable shifts [24, 66]. By introducing inhomogeneities into the applied optical field, the resonant Rydberg laser-excitation frequency becomes position-dependent allowing a degree of control via the spatial distribution of Rydberg excitations. Examining equation 3.14, we see that if inhomogeneities are introduced in the applied optical field, the Rydberg level shifts become state-dependent. In this case, microwave spectroscopy between two Rydberg states could be used to probe the Rydberg-state-dependent ponderomotive interaction.

We begin by examining the energy shift of a transition from the $5S_{1/2}$ ground state of ^{85}Rb into a Rydberg state in a homogeneous applied optical field. The shift is the sum of light shifts for the ground state and the Rydberg state. First, we consider the ponderomotive energy shift of a free electron or quasi-free Rydberg electron in a AC electric field ($E(t) = E_0 \cos(\omega t)$) and relate the shift W^{Q} to the field amplitude E_0 through a dynamic polarizability α_{e^-} such that

$$W^{\mathrm{Q}} = \frac{e^2 E_0^2}{4m\omega^2} = -\frac{1}{2}\alpha_{\mathrm{e}^-}\langle E^2\rangle_t = -\frac{1}{4}\alpha_{\mathrm{e}^-}E_0^2 \Rightarrow \alpha_{\mathrm{e}^-} = -\frac{e^2}{m\omega^2}$$

For a comparison, we look at the classical polarizability from the classical electron oscillator model (in the limit of large detuning from a single resonance) which is

written [71]:

$$\alpha = -\frac{e^2}{m}\frac{1}{\omega^2 - \omega_0^2} \tag{3.15}$$

where ω_0 is a resonance for the electron oscillator (atomic resonance). We note here that the polarizability for the free and Rydberg electron is described by the classical oscillator model with a resonance at $\omega_0 = 0$. For our experiment, we are interested primarily in a light field with angular frequency $\omega = 2\pi c/1064$ nm. In this case for a free/Rydberg electron, we have

$$\alpha_{e^-} = \alpha_{\mathrm{Ryd}} = -1.354 \times 10^{-7}\ \frac{\mathrm{cm}^2}{\mathrm{V}^2}\mathrm{MHz} \tag{3.16}$$

Using the expression for polarizability from the classical electron oscillator (CEO) model in equation 3.15, we can estimate the polarizability of the $5\mathrm{S}_{1/2}$ ground state of ^{85}Rb which has a dominant atomic resonance at $\omega_0 = 2\pi c/780$ nm.

$$\alpha_{5\mathrm{S,CEO}} = 1.573 \times 10^{-7}\ \frac{\mathrm{cm}^2}{\mathrm{V}^2}\mathrm{MHz}$$

This estimate agrees reasonably well with a more accurate determination of the dynamic polarizability of the $5S_{1/2}$ ground state (again $\omega = 2\pi c/1064$ nm), which has been calculated by Marinescu, et. al. [72]

$$\alpha_{5\mathrm{S}} = 1.776 \times 10^{-7}\ \frac{\mathrm{cm}^2}{\mathrm{V}^2}\mathrm{MHz} \tag{3.17}$$

For our calculations, we will use this value for the ground state polarizability.

In ^{85}Rb, the energy shift of a Rydberg level relative to the ground state is given by

$$\Delta W = \frac{1}{4}\left(\alpha_{5\mathrm{S}} - \alpha_{\mathrm{Ryd}}\right) E_0^2 \tag{3.18}$$

For a value of E_0 relevant to our experiments, we look at the intensity maximum of a focused (P_1=) 5 W laser beam with a radial Gaussian profile (full width at half

maximum of $x_{\mathrm{FWHM}} = 16$ μm at the focus),

$$E_0 = \sqrt{0.89 \frac{2P_1}{c\epsilon_0 x_{\mathrm{FWHM}}^2}} = 3.62 \times 10^4 \ \frac{\mathrm{V}}{\mathrm{cm}} \tag{3.19}$$

Plugging the values from equations 3.17, 3.16, and 3.19 into the expression in 3.18 for the energy shift of the Rydberg state relative to the ground state, we find

$$\Delta W = h \times 102 \text{ MHz}$$

which is large compared to the resolution of the Rydberg laser excitation sequence. We note that approximately 43 % and 57 % of the shift comes from the ponderomotive shift of the Rydberg state and the light shift of the ground state, respectively. The analysis described above is valid for situations in which the amplitude of the applied optical field varies over length scales that are large compared to the extent of the Rydberg wavefunction. For the focused laser beam profile described above, this condition is easily satisfied for $n < 100$. This focused laser field then makes the Rydberg excitation frequency a strong function of position. Combining a spatially dependent resonant excitation frequency with high resolution laser excitation, the spatial distribution of Rydberg excitations can be controlled by tuning the frequency of the laser excitation, which is demonstrated in the spectra in figure 3.4.

To obtain the spectra in figure 3.4, ^{85}Rb ground state atoms were loaded into an optical dipole trap by focusing the dipole trap laser through a MOT. The dipole trap is formed by focusing a 5 W, 1064 nm laser beam to a spot size of 16 μm full width at half maximum as described in the example above. Prior to the Rydberg excitation sequence, the MOT lasers were switched off, and atoms not confined in the dipole trap were allowed to fall away. The Rydberg excitation proceeded via a two-photon transition from the $5S_{1/2}$ ground state to the $47S_{1/2}$ Rydberg state through the $5P_{3/2}$ intermediate state. The 5S to 5P lower step of the transition was fixed at $\approx$1.5 GHz

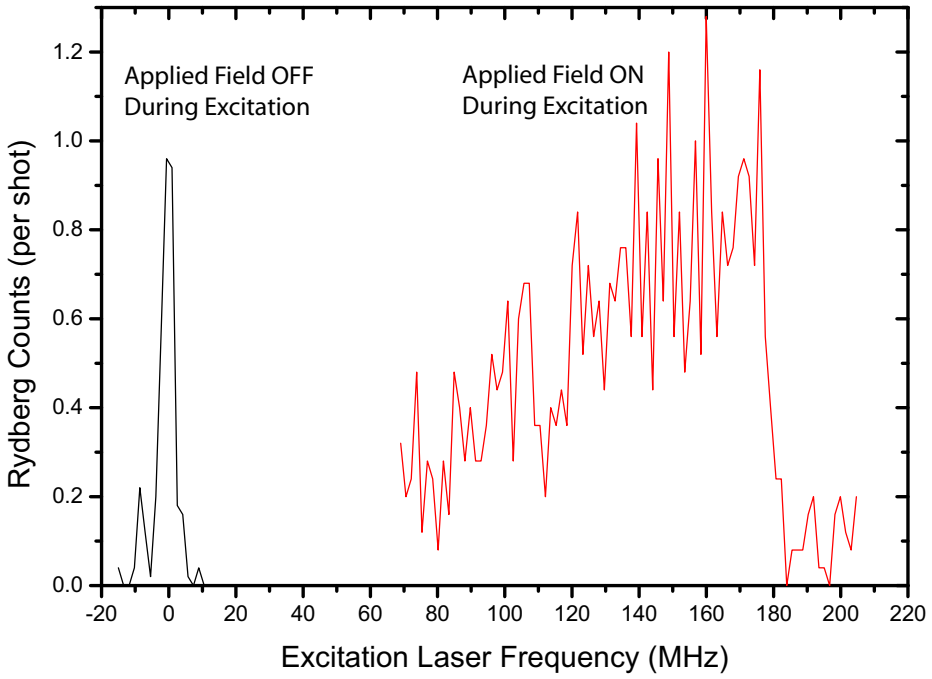

Figure 3.4: Light shift of the Rydberg excitation spectrum in a Gaussian laser focus. The black (red) curve is the spectrum in the absence (presence) of the applied optical field.

red-detuned from resonance. This is large enough that the effects arising from the intermediate state detuning, which depends on the intensity of the applied field, are insignificant. The frequency of the upper step of the two-photon transition ($\lambda \approx$ 480 nm) was scanned to obtain the spectra. The black curve showing the field free Rydberg excitation spectrum was obtained by switching off the dipole trap beam for a few microseconds prior to excitation and has a spectral width of about 6 MHz. The spectrum in red was taken with the dipole trap beam left on during the excitation sequence.

As compared to the field free spectrum, the red spectrum is significantly broadened, and its center of weight is shifted by the presence of the dipole trap light. The assymetric lineshape reflects the spatial distribution of ground state atoms within the dipole trap. The sharp cutoff on the high-frequency edge of the spectrum corresponds to the excitation of atoms at or near the intensity maximum along the axis

of the dipole trap. Taking the linewidth of the Rydberg excitation to be $\delta = 6$ MHz, the maximum shift to be $\Delta W = 175$ MHz, and the full width a half maximum of the dipole trap laser to be $x_{\mathrm{FWHM}} = 16$ μm, we can estimate the degree to which Rydberg atoms excited at the cutoff are localized near the axis to be

$$\Delta x = \frac{x_{\mathrm{FWHM}}}{2\sqrt{\ln(2)}} \ln\left(\frac{\Delta W}{\Delta W - \delta}\right) < 2 \ \mu\mathrm{m}$$

Thus, we see that spatial inhomogeneities in the light shift afford some control over the spatial distribution of Rydberg excitations. The magnitudes of the calculated shift (102 MHz) and measured shift (175 MHz) are similar. We note that the geometry of the dipole trap laser focus has not been rigorously characterized and the discrepancy between these two values could be accounted for in the uncertainty of the focal spot size.

Now, we turn our attention to estimating transition frequencies shifts between Rydberg states from these applied light fields. The estimates we have made so far ignore spatial inhomogeneities in the applied AC electric fields, and therefore give the same ponderomotive shift for all Rydberg states. The transition frequency shift between any two Rydberg states is then identically zero. In the following consideration, we account for the spatial inhomogeneities with an effective DC electric field derived from the ponderomotive force on the Rydberg electron, which is proportional to the intensity gradient of the applied field. We then use DC polarizabilities calculated for specific Rydberg states of interest to estimate transition frequency shifts.

The ponderomotive shift of a free electron in a Guassian laser focus, taken along a line through the focal spot, is given by

$$W^{\mathrm{Q}} = \frac{q^2|E(x)|^2}{4m\omega^2} = \frac{q^2|E_0|^2}{4m\omega^2} \exp\left[-\frac{2x^2}{s^2}\right]$$

where $|E_0|$ is the laser field amplitude on axis ($x = 0$) and s is the $1/e^2$ radius of the

laser focus. The force on an electron $|F^{\mathrm{Q}}| = |\nabla W^{\mathrm{Q}}|$:

$$|F^{\mathrm{Q}}| = |\frac{dW^{\mathrm{Q}}}{dx}| = \frac{q^2|E_0|^2}{4m\omega^2}\left(\frac{4x}{s^2}\right)\exp\left[-\frac{2x^2}{s^2}\right]$$

The maximal force occurs near $x = s/2$:

$$|F^{\mathrm{Q}}_{\mathrm{max}}| = |\frac{dW^{\mathrm{Q}}}{dx}|_{x=s/2} = \frac{q^2|E_0|^2}{4m\omega^2}\left(\frac{2e^{-1/2}}{s}\right)$$

The effective electric field experienced by an electron near the force maximum is written $E_{\mathrm{DC}} = |F^{\mathrm{Q}}_{\mathrm{max}}|/q$. Assuming that E_{DC} ($\propto \nabla I$) is constant over the extent of the Rydberg wavefunction, the magnitude of the shift on the Rydberg transition between states $|1\rangle$ and $|2\rangle$ is estimated to be

$$|\Delta W| = \frac{1}{2}\left|\alpha_1 - \alpha_2\right| E^2_{\mathrm{DC}}$$

where α_{i} is the DC polarizability of the Rydberg state $|i\rangle$.

We can extract DC polarizabilities for Rydberg states of interest from Stark shift calculations of these states in small electric fields, where the DC Stark shift can be written $W^{\mathrm{S}} = \frac{1}{2}\alpha_{\mathrm{i}}E^2_{\mathrm{DC}}$. Using this method, the polarizabilities for the Rydberg states 53S and 53P states are $\alpha_{53\mathrm{S}} = 76.2\ \frac{\mathrm{cm}^2}{\mathrm{V}^2}\mathrm{MHz}$ and $\alpha_{53\mathrm{P}} = 529.8\ \frac{\mathrm{cm}^2}{\mathrm{V}^2}\mathrm{MHz}$. Since the DC polarizability of a Rydberg state scales as n^7, the polarizability for nS and nP states can be written

$$\begin{aligned}\alpha_{n\mathrm{S}} &= 76.2\left(\frac{n}{53}\right)^7\ \frac{\mathrm{cm}^2}{\mathrm{V}^2}\mathrm{MHz}\\ \alpha_{n\mathrm{P}} &= 529.8\left(\frac{n}{53}\right)^7\ \frac{\mathrm{cm}^2}{\mathrm{V}^2}\mathrm{MHz}\end{aligned}$$

As in the previous estimate, we use the focus of a 5 W laser beam with a radial Gaussian profile ($x_{\mathrm{FWHM}} = 16\ \mu$m, $s = x_{\mathrm{FWHM}}/1.18$). In an experiment, one could tune the Rydberg excitation using the spatially dependent light shift such that Rydberg atoms are excited where the gradient in the applied field is largest. At the

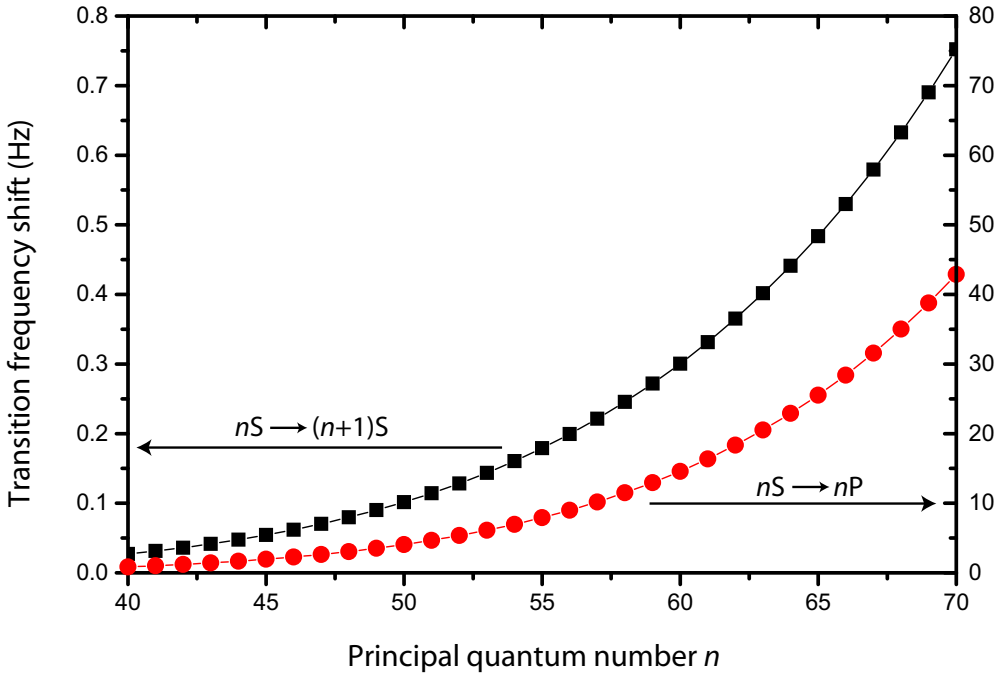

Figure 3.5: Maximal shift (magnitude) of Rydberg-Rydberg transition frequency in a Gaussian laser focus for two types of transitions vs. principal quantum number.

point of maximal gradient $x = s/2$, $E_{\mathrm{DC}} \approx 0.2$ mV/cm, which is a relatively small DC electric field despite the acute electric-field sensitivity of Rydberg atoms. Thus, transition frequency shifts between neighboring Rydberg states are quite small even though the shift of each Rydberg state is quite large. The shifts of two types of Rydberg-Rydberg transitions are plotted in figure 3.5. At $n = 60$, the frequency shifts of the two transitions are $|\Delta W(60\mathrm{S} \rightarrow 61\mathrm{S})| = 0.3$ Hz and $|\Delta W(60\mathrm{S} \rightarrow 60\mathrm{P})| = 14.6$ Hz. For a given n, the difference in the polarizabilities of the P and S states are large compared to the difference between the polarizabilities of neighboring S states. Thus, $|\Delta W(\mathrm{nS} \rightarrow (\mathrm{n}+1)\mathrm{S})| \ll |\Delta W(\mathrm{nS} \rightarrow \mathrm{nP})|$.

This estimate shows that inhomogeneities in the applied ponderomotive potential shift the transition frequencies by only a small amount. The maximum frequency shift for applied field used for this estimate (sl i.e., typical running wave dipole trap) is small compared to the natural linewidth of these states caused by their finite

lifetimes. Thus, experimentally resolving the effects of these shifts would not be feasible. However, if the gradients of the applied fields were stronger, as in a standing wave or optical lattice, the shifts would grow significantly. In such an applied field geometry, the periodicity of the lattice can be comparable to the size of the Rydberg atom. In this case, the assumption of spatially homogeneous gradients used in the above estimate breaks down. Evaluating the integral in equation 3.14 numerically can be done in order to calculate shifts for the case of large spatial gradients in the applied fields. In the section 3.4, we calculate the energy shifts in a 1D standing wave with a periodicity of 532 nm and examine the possibility of localizing Rydberg excitations within an optical lattice and spectroscopically resolving a Rydberg state dependent ponderomotive energy shift.

3.4 Rydberg State Dependent Shifts in Ponderomotive Optical Lattices

In section 3.3, we examined the ponderomotive shift of Rydberg energy levels in homogeneous and quasi-homogeneous applied optical fields. In our examples, we found that the levels were shifted by $\approx$ 100 MHz. We also estimated the effects adding weak spatial gradients (relative to the Rydberg atom size) to the applied optical field, which gives the shift some small dependence on the Rydberg state considered. In this section, we examine the energy level shifts of Rydberg atoms in a ponderomotive optical lattice. The strong gradients in the intensity profile of this applied optical field lead to a departure of the Rydberg level ponderomotive shift from that of a free electron. The nature of the Rydberg wavefunction becomes essential in determining the shift. To characterize this effect, we move beyond the simpler estimates of the previous section. The task is essentially to integrate equation 3.14 for a particular Rydberg state immersed in a standing plane wave. The formalism and

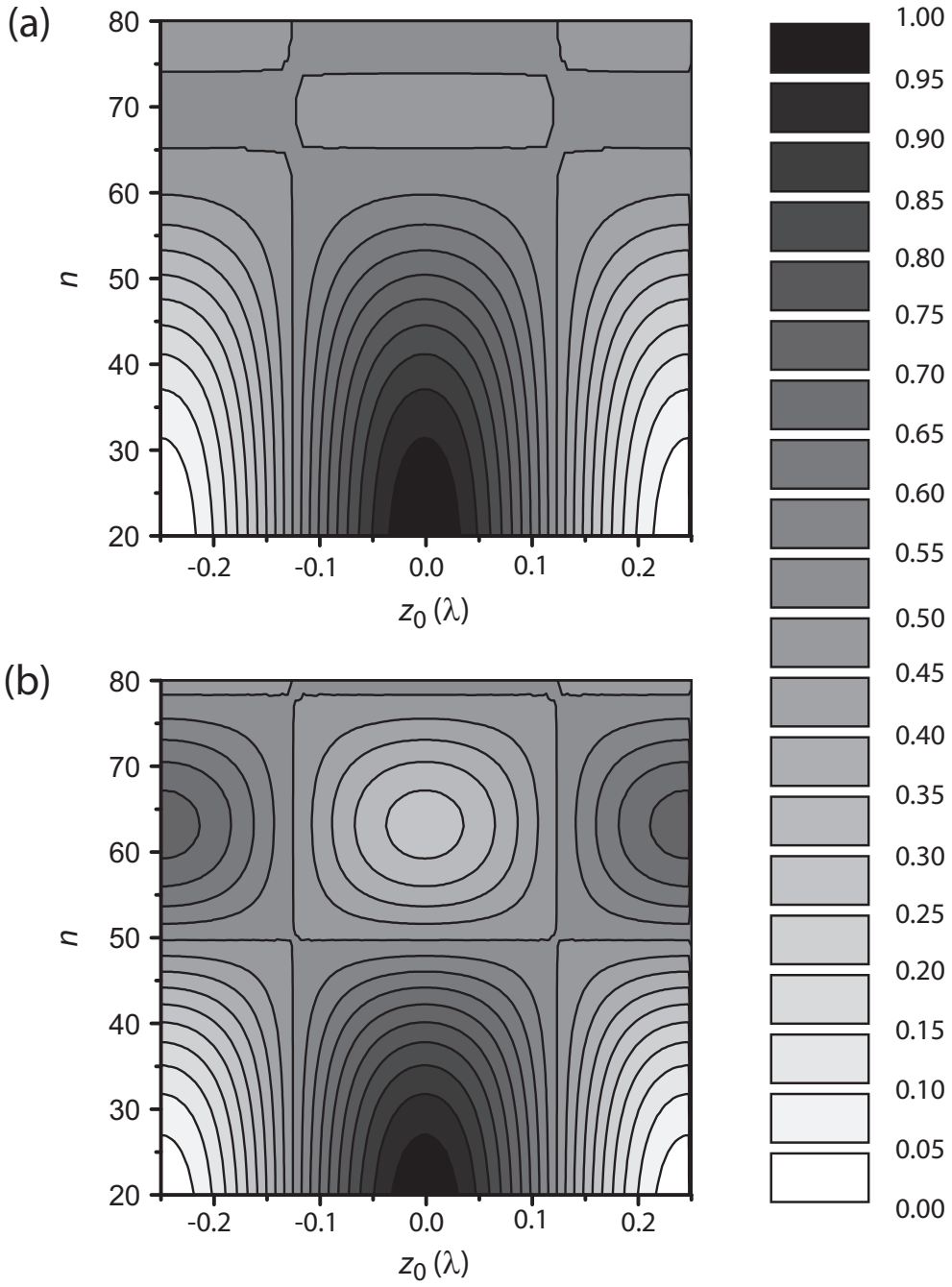

Figure 3.6: Shift of Rydberg levels nS (a) and nP (b) in a ponderomotive optical lattice with lattice constant 532 nm (retro-reflected, $\lambda = 1064$ nm laser beam). The shift is scaled in units of $\alpha_{\mathrm{Ryd}} \times |E_0|^2$, where E_0 is the single beam electric field amplitude.

procedure for carrying out this calculation is outlined extensively in section 4.1. In the discussion, we also develop tools for localizing Rydberg excitations in the lattice and spectrosopically probing the Rydberg state-dependent ponderomotive shift.

To be relevant to our experiments, we take the lattice to be formed by a $\lambda = 1064$ nm laser beam, which is retro-reflected on itself to form a standing wave. For convenience, the shifts plotted in this section are scaled by $\alpha_{\mathrm{Ryd}} \times |E_0|^2$, where E_0 is the single electric field amplitude. For a Gaussian laser focus geometry typical of our experiment, $|E_0|$ can be calculated using equation 3.19, which for a single beam power of ($P_1 =$) 1 W and $x_{\mathrm{FWHM}} = 16$ μm, $\alpha_{\mathrm{Ryd}} \times |E_0|^2 = 36$ MHz.

The 2D plots in figure 3.6 show the scaled shifts of Rydberg states nS (a) and nP, m=0 (b) as a function of principal quantum number n on the y-axis and the position of the Rydberg atom center-of-mass relative to the nearest lattice maximum z_0 on the x-axis. The quantization axis for this calculation is perpendicular to the lattice planes. At low n ($\lesssim 30$), the scaled shift approximately follows the shift of a free electron in the local intensity of the lattice. At higher n, the extent of the Rydberg atom wavefunction becomes appreciable relative to the lattice constant, and the ponderomotive shift of the Rydberg level reflects a spatial average of the light field weighted by the Rydberg wavefunction. When the extent of the wave function somewhat surpasses the lattice constant, the locations where the shift is maximal switch from the intensity maxima to the intensity minima. In this case, for a Rydberg atom whose center-of-mass is at an intensity minimum, the dominant lobes of the wavefunction sample regions of high intensity half a lattice period away, maximizing the time-averaged kinetic energy of the Rydberg electron. Figure 3.6(b) shows the level shift for the nP, $m = 0$ case, and the switch of the location of maximal shift just described occurs around $n = 63$. For the $m = 1$ case (not shown), the shift occurs at

much higher n since the dominant lobes of the wavefunction are aligned in the plane of the lattice such that the extent of the wavefunction normal to the lattice planes for a given n is less than in the $m = 0$ case (see the discussion of figure 4.4).

For a given n, the range of shifts present in the lattice with maximal and minimal shifts W^{Q}_{max} and W^{Q}_{min} can be characterized by the potential depth $\Delta W^{\mathrm{Q}} = W^{\mathrm{Q}}_{max} - W^{\mathrm{Q}}_{min}$. The ponderomotive shift as a function of z_0 can be viewed as an adiabatic potential governing the motion of the Rydberg center-of-mass as discussed in section 3.2. If the depth ΔW^{Q} is sufficient, the lattice forms a periodic array of Rydberg atom traps centered about the points of minimal ponderomotive shift [25]. The trap depth $\Delta W^{\mathrm{Q}} = 36$ MHz (e.g. low-n state in typical experimental geometry described above) corresponds to a temperature of about 1.5 mK which is sufficient to trap Rydberg atoms excited from laser-cooled ground state atoms (Doppler temperature Rb ≈ 150 μK). Additionally, for cases in which the depth ΔW^{Q} is large compared to the linewidth of the Rydberg excitation, the shifts could be used to exert some control over the spatial distribution of Rydberg excitations.

From the discussion of figure 3.6, we have seen that the shift depends strongly on the principal quantum number n, the orbital angular momentum ℓ, and the projection of the orbital angular momentum onto the axis normal to the lattice planes m. This suggests that a differential shift between neighboring Rydberg states could be observable using microwave spectroscopy of appropriate Rydberg-Rybderg transtions. Figure 3.7 shows the differential shift between neighboring Rydberg states $n\mathrm{S} \rightarrow n\mathrm{P}$ and $n\mathrm{S} \rightarrow (n+1)\mathrm{S}$ at the intensity maxima of the applied lattice. The maximal shift on the $n\mathrm{S} \rightarrow (n+1)\mathrm{S}$ transition occurring near $n = 50$ is $-0.018\alpha_{\mathrm{Ryd}} \times |E_0|^2$, which corresponds to a transition frequency shift of -650 kHz for the $P_1 = 1$ W, $x_{\mathrm{FWHM}} = 16$ μm geometry described above. Note that the shifts of the $n\mathrm{S} \rightarrow n\mathrm{P}$

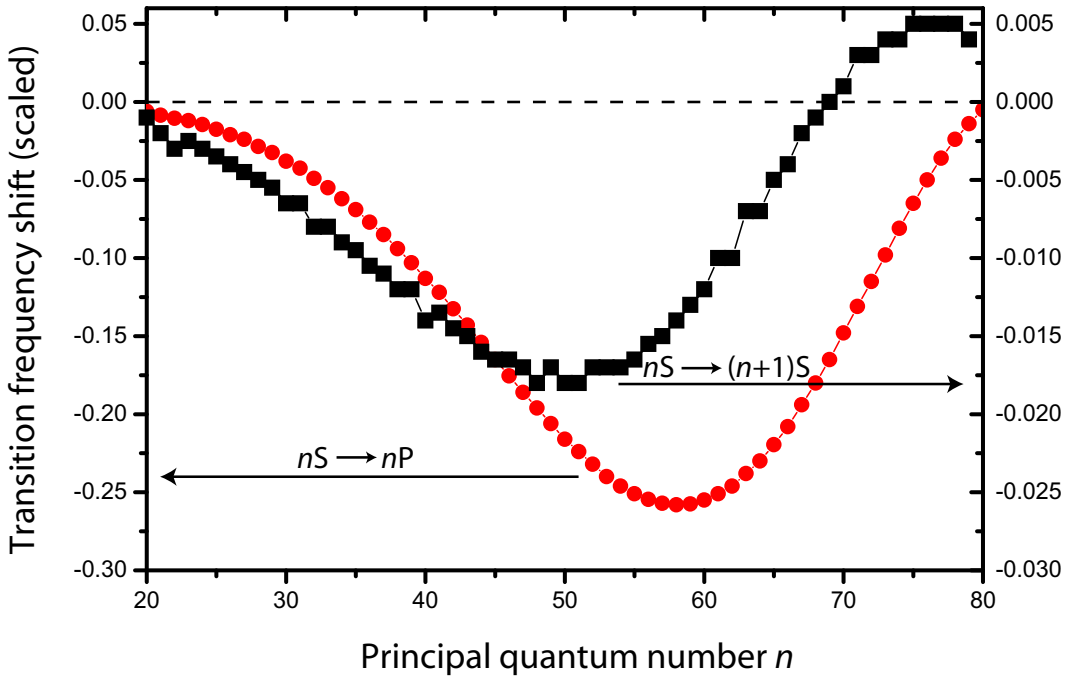

Figure 3.7: Frequency shift of Rydberg transitions nS $\rightarrow$ nP (left axis, red circles) and nS $\rightarrow$ $(n+1)$S (right axis, black squares) at the intensity maxima of a ponderomotive optical lattice with lattice constant 532 nm (retro-reflected, $\lambda = 1064$ nm laser beam). The shift is scaled in units of $\alpha_{\mathrm{Ryd}} \times |E_0|^2$, where E_0 is the single-beam electric field amplitude.

are larger in comparison to the nS $\rightarrow$ $(n+1)$S transition, and the scaling of their respective axes in figure 3.7 differs by a factor of ten.

The magnitude of this differential shift represents the amplitude of the transition frequency shift that varies sinusoidally with respect to the position of the Rydberg atom center of mass relative to the lattice maximum. For atoms uniformly distributed across the ponderomtive optical lattice, transitions to nearby states would be inhomogeneously broadened by the presence of the lattice. The width of the symmetric broadening would be comparable to the differential shift plotted in figure 3.7 for a given transition. In the vicinity of $n = 50$, readily achievable linewidths for the two-photon microwave transition nS $\rightarrow$ $(n+1)$S are on the order of 100 kHz and are often limited by the microwave interaction time (see section 5.4). Thus, the inhomogeneous line broadening should be visible under anticipated experimental

conditions.

It may also be possible to utilize the level shift of the initially laser-excited Rydberg state to localize Rydberg excitations to a particular lattice position (e.g. the intensity maximum) and subsequently probe the differential shift relative to the target Rydberg state using a microwave transition. In such a spectrum, one could expect a shift of the center of weight relative to the optical field free spectrum. There would be a couple of sources of inhomogeneous broadening. First, the line would broaden by an amount inversely proportional to the degree of localization achieved in the laser excitation, due to the range of differential shifts sampled by the Rydberg atoms. Second, motion during the microwave probe time would broaden the transition as Rydberg atoms sample various differential shifts in time. The motion would be governed by the initial kinetic energy of the Rydberg atoms, which is due to the thermal energy of the laser-cooled atoms from which they were excited and the net effect of the ponderomotive forces arising from the optical lattice. Motional effects are often important in experiments involving ponderomotive optical lattices as the distance traveled during an experimental interval can be appreciable relative to the lattice constant, and the effect of the lattice on a Rydberg atom usually depends on its relative position in the lattice.

In this chapter, we have examined the ponderomotive interaction between a Rydberg electron and an applied optical field. We started in section 3.1 by examining the interaction for a free electron, which is given simply by the time-averaged kinetic energy of its driven motion in the oscillating electric field. The intuition that the effect on the "quasi-free" Rydberg electron would be similar was placed on firm theoretical footing in section 3.2 through the separation of appropriate coordinate time-scales and the adiabatic elimination of the quiver motion that accounts for the

ponderomotive interaction with a time *independent* energy shift. In the next chapter, we examine the effects of adding time *dependence* to the ponderomotive interaction, specifically, amplitude modulation of an applied ponderomotive optical lattice.

CHAPTER IV

Rydberg Atoms in Time-Dependent Ponderomotive Potentials

4.1 Introduction

In chapter III, we introduced the ponderomotive interaction with the Rydberg electron, which can be seen as the time-averaged kinetic energy of free or quasi-free charges in electric fields that oscillate with periods much shorter than other characteristic time-scales of the particle motion. The disparity in timescales leads to the adiabatic elimination of the fast quiver motion allowing the ponderomotive interaction to be treated by adding a time-independent shift to the atomic Hamiltonian. Spatial inhomogeneities of the applied field amplitude lead to ponderomotive forces and state-dependent energy shifts.

Based on these interactions, the trapping of Rydberg atoms in the ponderomotive potentials created by standing-wave laser fields was proposed [25]. In that method, the quasi-free Rydberg electron is trapped in the periodic ponderomotive potential of a standing-wave laser field, and the entire atom is trapped due to weak Coulomb binding of the atomic nucleus to the trapped Rydberg electron. The spatial periods and the depths of ponderomotive standing-wave Rydberg-atom traps can be quite similar to those of standard optical lattices for atoms in atomic ground states. Due to this compatibility, ponderomotive optical lattices may become useful in recently

proposed quantum-information processing schemes that involve Rydberg levels [2, 4]. Regularly-spaced arrays of Rydberg atoms would also be useful in studying the random walk problem in quantum systems [73]. Furthermore, since trap-induced level shifts in ponderomotive Rydberg-atom traps are quite small, these traps are ideal for high-precision spectroscopy of Rydberg transitions. Perfect periodicity, micron-size trap dimensions, and small trap-induced level shifts set ponderomotive traps apart from other static-field Rydberg-atom traps that have been proposed or realized [16, 74–76].

In this chapter, we discuss the effects of adding harmonic time-dependence to the ponderomotive interaction. In particular, we focus on electric multipole transitions between Rydberg levels in amplitude-modulated standing-wave ponderomotive potentials [18]. We find that, by modulating the intensity of the applied optical field at an appropriate frequency, internal states of the Rydberg atom can be coupled, so driving transitions between Rydberg states using a time-dependent ponderomotive interaction should also be achievable. Due to sub-micron spatial period, the modulated potential is effective in driving a wide range of multipole transitions. As disucssed in section 3.4, the shifts in the transition frequencies should be measurable, but can be quite small in cases appropriate for spectroscopy with time-dependent ponderomotive potentials. Since crossed, focused laser beams may be used to form the standing-wave ponderomotive potential, the transitions can be induced with a high spatial selectivity (in the μm-range). This new method of driving microwave transitions between Rydberg levels could be useful for high-precision spectroscopy, studies of coherent interactions between Rydberg atoms, and quantum information processing applications.

4.2 Qualitative Picture of Rydberg-Rydberg Transitions in an Amplitude-Modulated Ponderomotive Optical Lattice

Before delving into the analysis of a more rigorous model the dynamics of a Rydberg atom immersed in a amplitude-modulated ponderomotive optical, we consider the simple time-domain picture of the interaction shown in figure 4.1, which captures many of the essential conclusions obtained in the rest of the chapter. The figure is illustrated such that a ponderomotive lattice is of a certain strength and the corresponding Rydberg wavefunctions are color-coded.

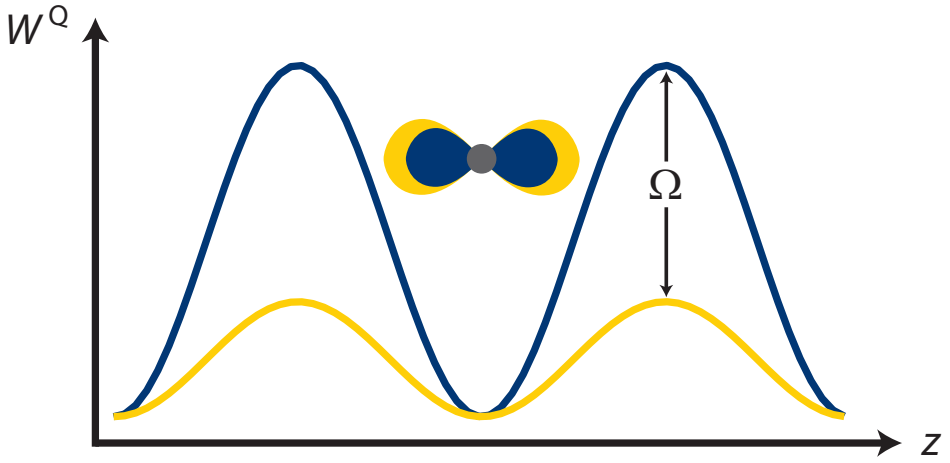

Figure 4.1: Qualitative picture of using amplitude-modulated ponderomotive optical lattices to drive multipole transitions between Rydberg states.

The blue curve represents the ponderomotive potential created by a standing plane wave whose lattice planes are perpendicular to the z-axis. A Rydberg atom located at an intensity minimum in the potential has a electronic wavefunction (also shown in blue) whose spatial distribution is determined by the Coulomb interaction with the ionic core (shown in gray) and the confinement of the lattice potential. If the ponderomotive potential is relaxed (shown in maize), the Rydberg wavefunction would expand somewhat to fill the volume also shown in maize. If the intensity of the light field creating the ponderomotive lattice were harmonically modulated at a

frequency Ω, then the electronic charge distribution in this picture would undergo a breathing-mode oscillation at this frequency. Charge oscillations with appropriate symmetries at a frequency resonant with the energy splitting between the initial Rydberg state and a target state result in population transfer from the initial to the target state (see section 9.11 in reference [77]). In this case, the charge oscillation has a breathing-mode character, which would be indicative of an even transition between states possessing the same parity.

The scale of the Rydberg electron wavefunction relative to the lattice constant in figure 4.1 is realistic for many Rydberg states of interest. The familiar dipole approximation for the interaction of an atomic electron and applied radiation field is based on the fact that the extent of the atomic wavefunction is small compared to the wavelength of the impinging radiation (see, *e.g.*, section 5.1 in reference [78]). This is not true for the case of a Rydberg atom in a ponderomotive optical lattice. In fact, many nonlinear terms in the transition matrix elements have similar magnitudes and make appreciable contributions to the coupling of relevant Rydberg states.

4.3 Quantitative Model of Rydberg Atom in Amplitude-Modulated Ponderomotive Optical Lattice

In this section, we develop a quantitative model to describe the ponderomotive interaction of a Rydberg atom with an applied standing plane wave whose intensity is harmonically modulated. As discussed in section 3.2, the fast quiver motion of the driven electron can be adiabatically eliminated from the Rydberg atom plus applied field system by adding the eigenvalues of equation 3.11 to the atomic Hamiltonian. Thus, an optical wave of angular frequency ω with a position-dependent, slowly

varying electric-field amplitude $\mathbf{E}(\mathbf{r},t)$ adds a ponderomotive potential

$$W^{\mathrm{Q}}(\mathbf{r},t) = \frac{e^2|\mathbf{E}(\mathbf{r},t)|^2}{4m_e\omega^2} \ , \tag{4.1}$$

to the inner-atomic Coulomb potential ($-e$ and m_{e} are the electron charge and mass, respectively). Assuming that the optical wave is a one-dimensional standing plane wave in z-direction and that it is amplitude-modulated at an angular frequency, Ω, the Rydberg-electron potential is, in atomic units,

$$V = -1/r + V_c(r) + (A + B\cos(\Omega t))(1 + \cos(2k(z - z_0))) \quad , \tag{4.2}$$

where $V_c(r)$ is a short-range core potential consistent with the quantum defects of the atom (see table 1.1 for ^{85}Rb), $2B$ is the temporal modulation amplitude of the depth of the ponderomotive lattice potential, $2A$ is its time-averaged depth (A and B are positive, and $A \geq B$), z_0 is the location of the peak of the lattice potential closest to the center of mass of the Rydberg atom (which is at $r = 0$), and $k = \omega/c$ (see figure 4.2). The spatial part of the lattice potential can be expanded about $z = 0$, leading to

$$V = -1/r + V_c(r) + (A + B\cos(\Omega t))\sum_{p=0}^{\infty} C_p z^p \tag{4.3}$$

with coefficients

$$C_p = \frac{(2k)^p}{p!}\begin{cases} (-1)^{p/2}\cos(2kz_0) + \delta_{p,0} & , \quad p\,\mathrm{even} \\ (-1)^{(p-1)/2}\sin(2kz_0) & , \quad p\,\mathrm{odd} \end{cases} \ , \tag{4.4}$$

where $\delta_{p,0}$ is a Kronecker-δ.

Ignoring the spin degree of freedom of the Rydberg electron, in the bound energy range the Hamiltonian can be represented in the spherical basis $\{|n,l,m\rangle\}$ and has elements

$$\begin{aligned} &H_{n,l,m}^{n',l',m'} = E_{n,l}\delta_{n,n'}\delta_{l,l'}\delta_{m,m'} \\ &+(A + B\cos(\Omega t))\sum_{p=0}^{\infty} C_p \left(r^p\right)_{n,l}^{n',l'} \left(\cos^p\theta\right)_{l,m}^{l',m'}\delta_{m,m'} \end{aligned} \tag{4.5}$$

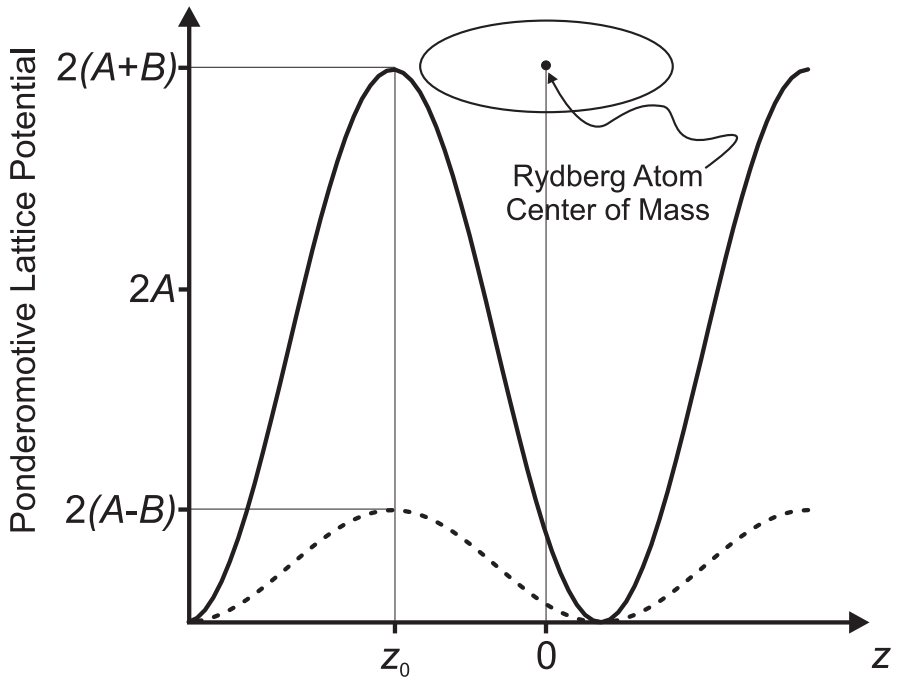

Figure 4.2: Ponderomotive optical lattice potential amplitude-modulated at frequency Ω for $\Omega t = 0$ (solid) and $\Omega t = \pi$ (dotted) vs. the Rydberg-electron coordinate in the center of mass frame z, where z_0 is the location of the lattice potential peak nearest to the Rydberg atom center of mass. Equipotential surfaces for the ponderomotive potential are planes perpendicular to the z-direction, which is chosen to be the quantization axis.

with perturbation-free energy levels, $E_{n,l}$, and radial and angular matrix elements, $(r^p)_{n,l}^{n',l'}$ and $(\cos^p\theta)_{l,m}^{l',m'}$, respectively.

The radial matrix elements depend on the quantum defects of the atom (see table 1.1 for ^{85}Rb); here, we compute the radial matrix elements numerically using a method described previously (see section II in reference [32]).

Since the m-quantization axis in equation 4.2 is transverse to the equipotential surfaces of the ponderomotive lattice potential, the Hamiltonian equation 4.5 does not depend on the azimuthal coordinate and, therefore, does not couple states of different m (see figure 4.2). Using Wigner 3j symbols, the angular matrix elements can be written as

$$(\cos^p\theta)^{l',m}_{l,m} = (-1)^m\, p! \sum_{\tilde{l}=p,p-2,\ldots,0} \frac{(2\tilde{l}+1)\sqrt{(2l+1)(2l'+1)}}{2^{(p-\tilde{l})/2}(\frac{p-\tilde{l}}{2})!(p+\tilde{l}+1)!!} \times \begin{pmatrix} l' & \tilde{l} & l \\ 0 & 0 & 0 \end{pmatrix} \begin{pmatrix} l' & \tilde{l} & l \\ -m & 0 & m \end{pmatrix} \quad (4.6)$$

equation 4.5 is then written as $H^{n',l',m'}_{n,l,m} = E_{n,l}\delta_{n,n'}\delta_{l,l'}\delta_{m,m'} + (A + B\cos(\Omega t))D^{n',l',m}_{n,l,m}\delta_{m,m'}$ with

$$\begin{aligned} D^{n',l',m}_{n,l,m} &= (-1)^{m+\frac{\tilde{l}_{\min}-\eta}{2}} \sum_{p=\tilde{l}_{\min},\tilde{l}_{\min}+2,\ldots} (-1)^{\frac{p-\tilde{l}_{\min}}{2}} (2k)^p (r^p)^{n',l'}_{n,l} \left[\cos(2kz_0 - \frac{\eta\pi}{2}) + \delta_{p,0}\right] \\ &\times \left[\sum_{\tilde{l}=p,p-2,\ldots,0} \frac{(2\tilde{l}+1)\sqrt{(2l+1)(2l'+1)}}{2^{\frac{p-\tilde{l}}{2}}\,(\frac{p-\tilde{l}}{2})!\,(p+\tilde{l}+1)!!} \begin{pmatrix} l' & \tilde{l} & l \\ 0 & 0 & 0 \end{pmatrix} \begin{pmatrix} l' & \tilde{l} & l \\ -m & 0 & m \end{pmatrix}\right] \end{aligned} \quad (4.7)$$

where $\tilde{l}_{\min} = |l - l'|$, the parameter $\eta = 0$ for even $\tilde{l}_{\min}$, and $\eta = 1$ for odd $\tilde{l}_{\min}$. We assume that the atoms are initially prepared in a state $|1\rangle = |n, l, m\rangle$. The off-diagonal terms $(A + B\cos(\Omega t))D^{n',l',m}_{n,l,m}$ will drive a multipole transition into state $|2\rangle = |n', l', m\rangle$ if the modulation frequency $\Omega \approx \Omega_A = (E_{n',l'} - E_{n,l})/\hbar$. The dynamics remains restricted to the space $\{|1\rangle, |2\rangle\}$ if both states $|1\rangle$ and $|2\rangle$ are sufficiently non-degenerate, *i.e.* if $|E_{n,l} - E_{n'',l''}| \gg A$ and $|E_{n',l'} - E_{n'',l''}| \gg A$ for all states $|n'', l'', m\rangle \notin \{|1\rangle, |2\rangle\}$ (note that $A > B$ always). This requirement largely means that the quantum defects of the states $|1\rangle$ and $|2\rangle$ differ from those of other l-states by $\gg n^3\, A$ (with A in atomic units). For transitions between lower-angular-momentum states of heavy alkali atoms ($l \lesssim 6$) these assumptions are satisfied under anticipated experimental conditions. The Hamiltonian within the subspace of coupled states,

$\{|1\rangle, |2\rangle\}$,

$$H = \begin{pmatrix} 0 & 0 \\ 0 & \hbar\Omega_A \end{pmatrix} + (A + B\cos(\Omega t)) \begin{pmatrix} D_{11} & D_{12} \\ D_{12} & D_{22} \end{pmatrix} \tag{4.8}$$

Defining the wave-function $|\psi\rangle = c_1|1\rangle + c_2|2\rangle$ and transformed coefficients $\tilde{c}_k = c_k \exp(-\mathrm{i}\phi(\mathrm{t}))$ with $\phi(t) = -\mathrm{i}\int^t \left[AD_{11} + B\frac{(D_{11}+D_{22})}{2}\cos(\Omega t')\right] dt'$ for $k = 1, 2$, the Hamiltonian transforms into

$$\tilde{H} = \begin{pmatrix} -B\frac{D_{22}-D_{11}}{2}\cos(\Omega t) & (A + B\cos(\Omega t))D_{12} \\ (A + B\cos(\Omega t))D_{12} & \hbar\Omega_A + A(D_{22} - D_{11}) + B\frac{D_{22}-D_{11}}{2}\cos(\Omega t) \end{pmatrix} \tag{4.9}$$

Defining $\delta = (\Omega_A - \Omega) + A(D_{22} - D_{11})/\hbar$, the Rabi frequency $\chi = BD_{12}/\hbar$, and the auxiliary variables $\epsilon = B\frac{(D_{22}-D_{11})}{2\hbar}$ and $\mu = AD_{12}/\hbar$, and transforming $\check{c}_1 = \tilde{c}_1$ and $\check{c}_2 = \tilde{c}_2 \exp(-\mathrm{i}\Omega t)$, the Hamiltonian transforms into

$$\check{H} = \hbar \begin{pmatrix} -\epsilon\cos(\Omega t) & \mu\mathrm{e}^{-\mathrm{i}\Omega t} + \frac{\chi}{2}\left[1 + \mathrm{e}^{-\mathrm{i}2\Omega t}\right] \\ \mu\mathrm{e}^{\mathrm{i}\Omega t} + \frac{\chi}{2}\left[1 + \mathrm{e}^{\mathrm{i}2\Omega t}\right] & \delta + \epsilon\cos(\Omega t) \end{pmatrix} \tag{4.10}$$

The terms $\propto \mathrm{e}^{\pm\mathrm{i}2\Omega t}$ cause a Bloch-Siegert shift of the resonance from $\delta = 0$ by an amount $\chi^2/(4\Omega)$ [79]. Since $\Omega \gg \chi$, for the purpose of the present discussion the Bloch-Siegert shift is negligible. Because $\Omega \gg \epsilon$ and $\Omega \gg \mu$, the rapidly oscillating terms $\propto \cos(\Omega t)$ and $\mathrm{e}^{\pm\mathrm{i}\Omega t}$ also do not cause significant shifts of the resonance from $\delta = 0$. We have confirmed this by numerical simulations. Consequently, the Hamiltonian

$$\check{H} \approx \hbar \begin{pmatrix} 0 & \frac{\chi}{2} \\ \frac{\chi}{2} & \delta \end{pmatrix} \quad . \tag{4.11}$$

An amplitude-modulated ponderomotive lattice therefore has two main effects. First, the lattice drives multipole transitions if the modulation frequency, Ω, is in the vicinity of an atomic transition frequency, $\Omega_A = |E_{n',l'} - E_{n,l}|/\hbar$. The Rabi frequency

of these transitions is

$$\chi = BD^{n',l',m}_{n,l,m}/\hbar \tag{4.12}$$

with B defined in equation 4.2 and $D^{n',l',m}_{n,l,m}$ in equation 4.7. Second, the resonance $\delta = 0$ occurs at a frequency Ω that is shifted from Ω_A by an amount

$$\Delta W = \Omega_{\mathrm{A}} - \Omega = A(D^{n',l',m}_{n',l',m} - D^{n,l,m}_{n,l,m})/\hbar \tag{4.13}$$

with A defined in equation 4.2.

4.4 Relating the Model to Experimental Parameters

In this section, we calculate realistic values for A and B based primarily on the capabilities of current electro-optic modulator technology and the laser beam geometry in our experiment. Broadband fiber-coupled modulators [80] have a modulation-frequency range $0 \lesssim \Omega \lesssim 2\pi\times 40$ GHz, which covers many transitions between Rydberg levels. This imposes a restriction on the states that can be experimentally coupled using this techinique. However, neighboring Rydberg states ($n \gtrsim 45$) have transition frequencies in this range. Furthermore, this is not a fundamental limitation, and the applicability of the method will expand with the modulator technology. Typically, the modulators are usable for optical powers up to a few 100 mW (at a wavelength $\lambda = 2\pi c/\omega \approx 1064$ nm) and they allow for close to 100% amplitude modulation (*i.e.* $A = B$ in equation 4.2).

In our experiment, the ponderomotive optical lattice is formed by a retro-reflected laser beam with a single beam intensity of $P_1 = 150$ mW, which is determined by the power limitations of the modulator. To achieve appropriate intensities, the incoming and return beams are focused to a full width at half maximum of $x_{\mathrm{FWHM}} = 15$ μm.

The electric field maximum achieved with such a beam geometry is given by

$$E_0 = \sqrt{0.89 \times 8P_1/(c\epsilon_0 x_{\mathrm{FWHM}}^2)} = 1.34 \times 10^4 \ \frac{\mathrm{V}}{\mathrm{cm}} \tag{4.14}$$

From equation 4.1 it follows that the standing-wave ponderomotive potential for this beam geometry has a peak value of $W^{\mathrm{Q,max}} = \frac{e^2 E_0^2}{4 m_e \omega^2} = -\frac{\alpha_{\mathrm{Ryd}}}{4}|E_0|^2 = h \times 6.1$ MHz. For the case of 100% amplitude modulation it follows from equation 4.2 that

$$A = B = W^{\mathrm{Q,max}}/4 = -\frac{\alpha_{\mathrm{Ryd}}}{16}|E_0|^2. \tag{4.15}$$

For convenience in interpreting the plots presented in the remainder of this chapter for a variety of lattice configurations (power, focal spot size), many of them will be scaled by the factor $W^{\mathrm{Q,max}}/4h$ (except for figure 4.6, which is an energy shift simply scaled by scaled by $W^{\mathrm{Q,max}}$). Determination of Rabi frequencies or transition frequency shifts from the scaled quantities presented in the figures for specific geometries can be made using equations 4.14 and 4.15. In many of the numerical examples, we will use $A = B = h \times 500$ kHz as a somewhat conservative estimate based on the strength of the ponderomotive optical lattices anticipated using the beam geometry just described above.

4.5 Computational Results

To exhibit the trends of the Rabi frequencies χ with the change in angular momentum and principal quantum number, in figure 4.3 we show the magnitude $|\chi|$ for the transitions $|n, l = 0, m = 0\rangle \leftrightarrow |n+1, l', m = 0\rangle$ as a function of n and lattice position, z_0, for l' ranging from 0 to 5. In the calculation of the radial matrix elements, $(r^p)_{n,l}^{n',l'}$, all quantum defects δ_l are assumed to be small ($\delta_l \leq 0.01$ for all l) but sufficiently large and distinct from one another such that the non-degeneracy condition for the coupled states (discussed above) is satisfied. First and foremost, it

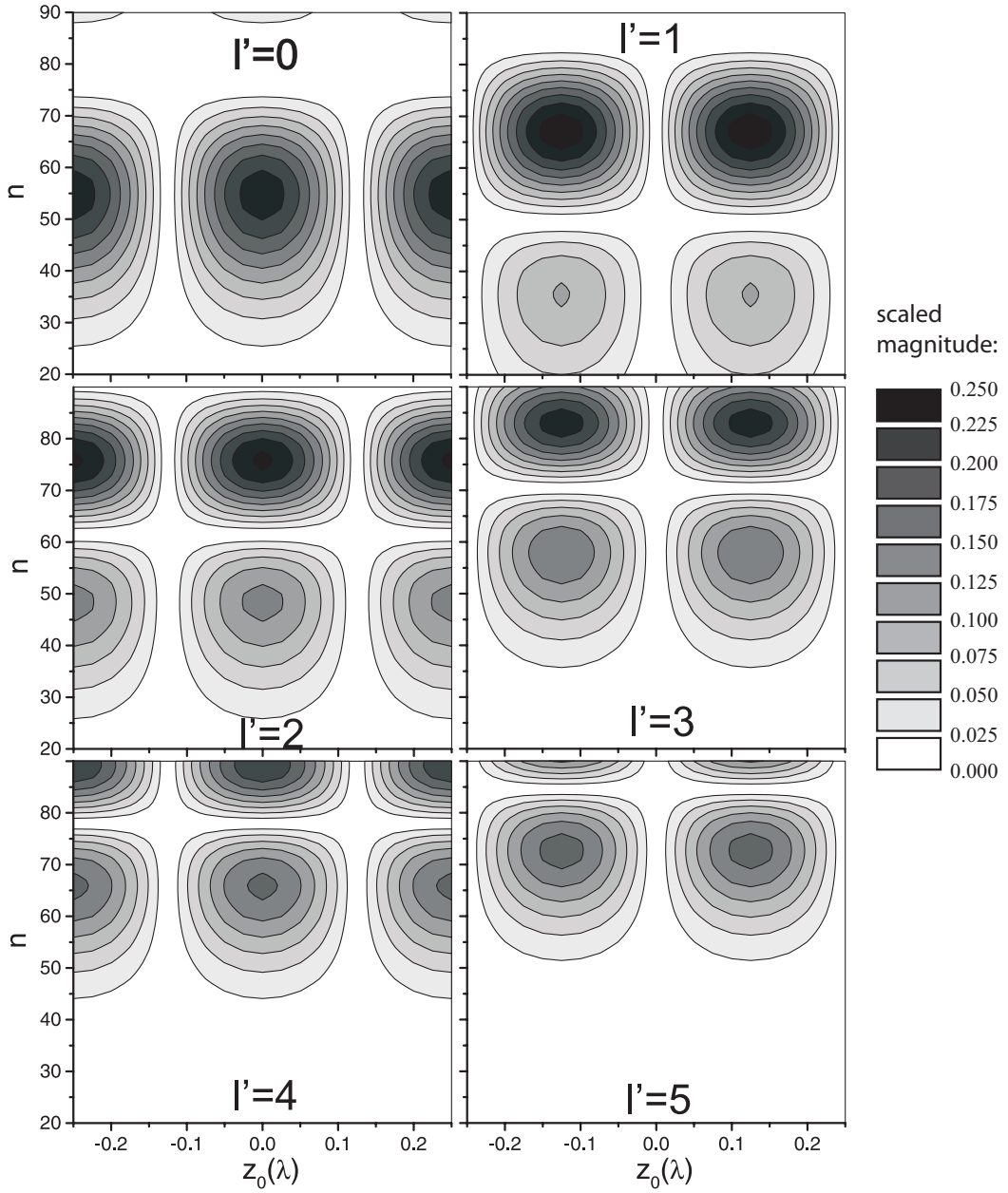

Figure 4.3: Rabi frequencies $|\chi|$ (scaled by $B/h = W^{\mathrm{Q,max}}/4h$ from equation 4.15) of the transitions $|n, l = 0, m = 0\rangle \leftrightarrow |n + 1, l', m = 0\rangle$ for the indicated values of l' vs principal quantum number, n, and lattice position, z_0. If we take the underlying amplitude-modulated ponderomotive lattice to have temporal modulation amplitude of $B = h \times 500$ kHz, the grayscale for the Rabi frequencies ranges from 0 to 125 kHz. (Note that $l' = \tilde{l}_{\mathrm{min}} = |l - l'|$ for the cases shown in this figure.)

is noted in figure 4.3 that the largest Rabi frequencies are of order 125 kHz. Thus, the interaction time t_π required to effect a π-pulse, for which $(\chi/2)t_\pi = \pi$, is $t_\pi \sim 8$ μs. This is considerably less than typical Rydberg-atom lifetimes. Furthermore, laser-cooled atoms excited into Rydberg states have speeds of only a few cm/s and move only about one period of the standing-wave ponderomotive potential during t_π. At the same time, the value of χ contains equal positive and negative domains over one lattice period, so this motion can cause appreciable cancellation of net transition probability. The mitigating effects are discussed in detail in section 5.6. However, we will see that given anticipated experimental conditions, these motional effects are manageable. Multipole transitions in modulated ponderomotive standing-wave potentials should therefore be readily observable in experiments.

Since in equation 4.7 it is $\eta = 0$ ($\eta = 1$) for even (odd) $\tilde{l}_{\min} = |l - l'|$, the Rabi frequencies have a cosine-like (sine-like) dependence on z_0, corresponding to cases depicted in the left column (right column) of figure 4.3. These dependencies reflect the parity behavior of the transitions. At the maxima and minima of the ponderomotive potential, corresponding to locations $z_0 = \pm\lambda/4$ and $z_0 = 0$ in figure 4.3, the perturbation has even parity, and consequently only even-$\tilde{l}_{\min}$ transitions occur while odd-$\tilde{l}_{\min}$ transitions vanish. At the midpoints between adjacent maxima and minima of the ponderomotive potential, corresponding to locations $z_0 = \pm\lambda/8$ in figure 4.3, the perturbation has odd parity, and consequently only odd-$\tilde{l}_{\min}$ transitions occur while even-$\tilde{l}_{\min}$ transitions vanish.

At fixed z_0, the Rabi frequencies are modulated as a function of n. Since $\hbar\chi = B\langle n', l', m|\cos(2k(z-z_0))|n, l, m\rangle$, this modulation reflects an interplay of the spatial dependencies of the perturbation, $B\cos(2k(z-z_0))$, and the involved wavefunctions. Qualitatively, Rabi frequencies tend to vanish at principal quantum numbers for

which the dominant lobes of the wavefunctions overlap in equal parts with positive and negative domains of $\cos(2k(z - z_0))$. Near-perfect cancellation can only occur if the atom diameter, which is $\approx 4n^2$, covers or exceeds one period of the standing-wave ponderomotive potential. In figure 4.3, the standing-wave period $4n^2 \gtrsim \lambda/2 = 532$ nm for $n \gtrsim 50$. In accordance with this estimate, the lowest principal quantum number at which $|\chi|$ undergoes a cancellation varies from $n \approx 50$ for $l' = 1$ to $n \approx 85$ for $l' = 5$. Formally, the dependence of $|\chi|$ on n becomes evident from equation 4.7 as follows. Since initial and final states are different and therefore orthogonal, the radial matrix element $((2kr)^p)_{n,l}^{n',l'}$ vanishes for $p = 0$, and the cosine-term can be factored out. The terms remaining under the p-sum have alternating signs, allowing one to write the sum as a difference $P_{\text{even}} - P_{\text{odd}}$, where P_{even} (P_{odd}) denotes the partial p-sum over even (odd) p-terms. Since the radial matrix elements scale as $(2kn^2)^p$, with increasing n increasingly higher-p terms dominate in the p-sums. The factorials in equation 4.7 scale even faster in p than the radial matrix elements, and consequently the p-sums converge quickly. For parameters as in figure 4.3, the p-sums can be truncated at p-values ranging from about $\tilde{l}_{\text{min}} + 10$ to $\tilde{l}_{\text{min}} + 40$, depending on the ratio between the atom size and the period $\lambda/2$ of the ponderomotive lattice. As n increases, the weight in the p-sums gradually shifts from lower to higher p, and the difference $P_{\text{even}} - P_{\text{odd}}$ slowly alternates between positive and negative values. At certain n-values, $P_{\text{even}} \approx P_{\text{odd}}$, and the Rabi frequencies practically vanish.

In figure 4.3, the domains where Rabi frequencies are large gradually shift to larger n with increasing $\tilde{l}_{\text{min}}$ (except for the special case $\tilde{l}_{\text{min}} = 0$, which will be discussed separately). Qualitatively, this trend reflects the fact that the factorials in equation 4.7 generally increase with $\tilde{l}_{\text{min}}$. Therefore, with increasing $\tilde{l}_{\text{min}}$ larger matrix elements $((2kr)^p)_{n,l}^{n',l'}$ are required to result in appreciable Rabi frequencies.

Hence, the observed shift of the domains of large Rabi frequencies to larger n with increasing $\tilde{l}_{\min}$. It is noted that the case $\tilde{l}_{\min} = 0$ does not fit into the pattern followed by all other $\tilde{l}_{\min}$. In the case $\tilde{l}_{\min} = 0$, the first term under the p-sum in equation 4.7, $p = 0$, vanishes because the radial matrix element $(r^p)^{n',l}_{n,l} = 0$ for $p = 0$ and $n \neq n'$ (due to the orthonormality of the involved radial wavefunctions). The lack of the first term under the p-sum makes the case $\tilde{l}_{\min} = 0$ an exception. It is indeed seen in figure 4.3 that the Rabi frequencies in the case $\tilde{l}_{\min} = 0$ are largest at n-values at which the Rabi frequencies of the next case, $\tilde{l}_{\min} = 1$, are smallest.

In section 4.3, we saw that if we choose the quantization axis along the z-direction, the azimuthal symmetry prevents the ponderomotive optical lattice from coupling states of different m. The effects of the lattice, however are not the same for differing m states, and the differences stem mainly from how the dominant lobes of a particular wavefunction align relative to the z-axis of the optical lattice. Figure 4.4 can be divided into two columns. The left-hand column shows hydrogenic wavefunction probability distributions $|\psi_{n,\ell,m}|^2$ in the $x - z$ plane and a corresponding Rabi frequency plot for a transition between neighboring states in rubidium in which $m = 0$. The right-hand column contains the corresponding information for the $m = 1$ case, with all other parameters the same.

The wavefunctions illustrated in the plots are the spherical $|n, \ell, m >$ states which are solutions to the hydrogen atom problem [81] and are meant to give qualitative feel for the properties of the Rydberg wavefunctions relevant in this discussion. The wavefunction plots in part a clearly show that for states with same n and ℓ the state with the lowest m has the greatest average extent along the z-axis (normal to the lattice planes). In more compact notation, $m < m' \Rightarrow \langle z^2 \rangle_m > \langle z^2 \rangle_{m'}$. This is an important point when considering the ponderomotive interaction of a Rydberg

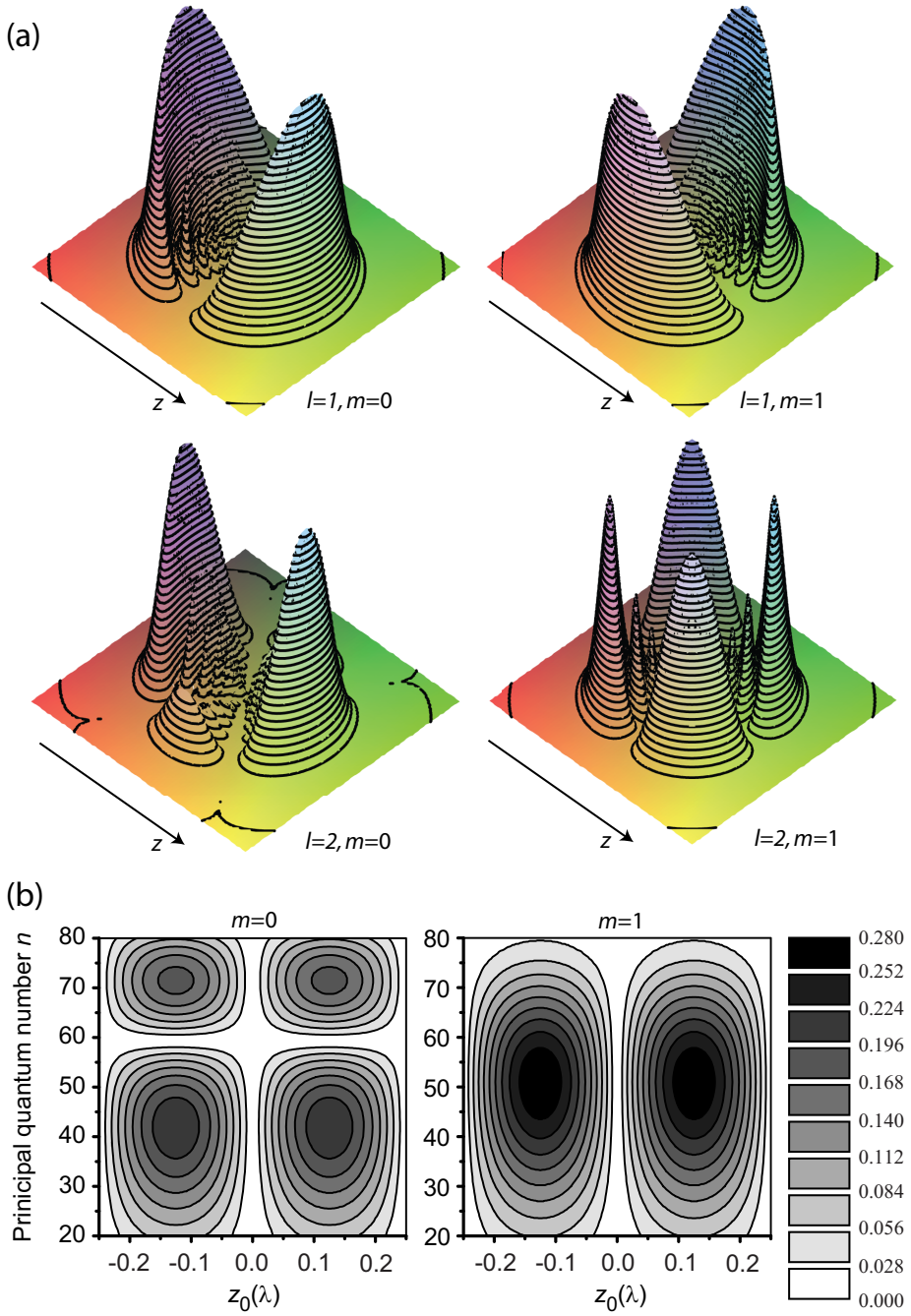

Figure 4.4: (a) Hydrogenic wavefunctions $|\psi_{n,\ell,m}|^2$ in the $x-z$ plane for $n = 10$ and the angular momentum quantum numbers listed in the figure. (b) The Rabi frequency $|\chi|$ (scaled by $B/h = W^{\mathrm{Q,max}}/4h$ from equation 4.15) on the left (right) hand for the $|nP, m = 0\rangle \rightarrow |(n-1)D, m = 0\rangle$ ($|nP, m = 1\rangle \rightarrow |(n-1)D, m = 1\rangle$) transition in rubidium. The figure is arranged in columns such that the left-hand (right-hand) column shows the wavefunctions and Rabi frequency plot for an m=0 (m=1) case.

electron, since the interaction of the Rydberg level reflects the spatial average of the light field weighted by the Rydberg wavefunction (see equation 3.14). The $m = 0$ wavefunction has a fairly small weighting near the location of the center-of mass and extends predominately along the z-axis (normal to the lattice planes). The Rabi frequencies in the lattice for the $m = 0$ case go to zero near $n = 60$, which occur, as discussed above, when the dominant lobes of the wavefunction sample equal parts of the domains of positive and negative Rabi frequencies in the lattice. The $m = 1$ case does not display such a minimum over the plotted range since their orientation relative to the lattice planes prevents them from sampling a sufficient range in the lattice ($>$ 1 lattice period) for the cancellation to occur.

When performing experiments, one should make sure to account for the effects of the Rydberg atom's "orientation" relative to the lattice planes. In principle, this can be controlled by using proper external fields and the application of appropriately polarized light during the photo-excitation of Rydberg atoms in the lattice. As a final note, this example highlights the effects of the m quantum number on the Rabi frequencies, but similar inferences can also be made regarding the energy level shifts. The use of nS states simplifies the situation by limiting the initial state and all states coupled by the lattice to the $m = 0$ case. Initial experiments, described in chapter 5.1, begin with optical excitation into a spherically symmetric nS state.

In section 5.4, we present the analysis relevant to the nS states (in addition to the discussion of energy shifts found in chapter III), so we focus here on another experimentally relevant example, the transitions of rubidium atoms in the nD-state into higher-angular-momentum states with principal quantum numbers $n-1$. Due to the quantum defects of Rb (see table 1.1 for ^{85}Rb; $\delta_{l=2} = 1.34$, $\delta_{l=3} = 0.02$, $\delta_{l\geqslant 4} \sim 0$), for these transitions the change in effective quantum number is only ≈ 0.34, leading

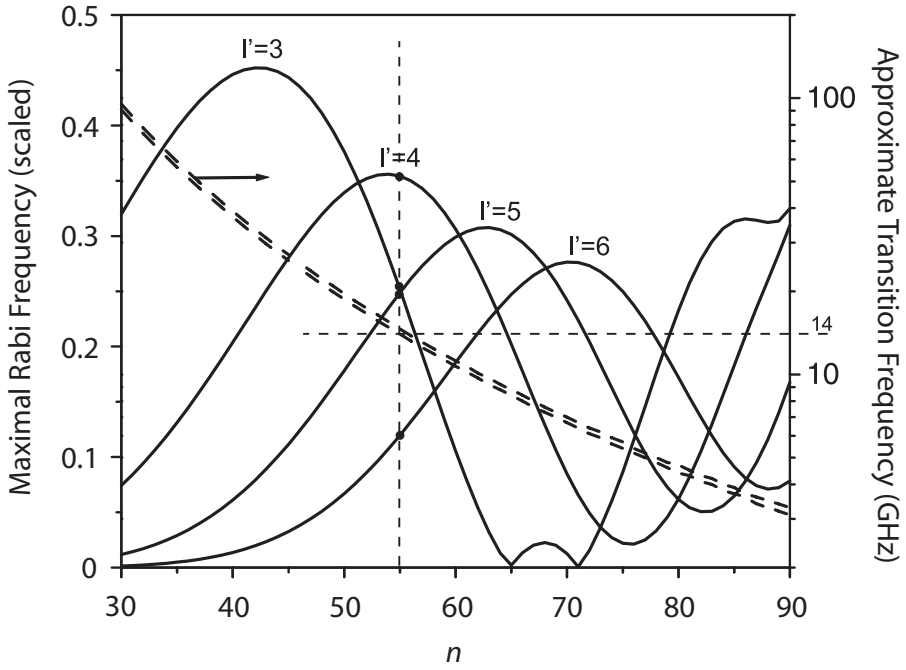

Figure 4.5: Maximal Rabi frequencies $|\chi|$ (scaled by $B/h = W^{\mathrm{Q,max}}/4h$ from equation 4.15) of the transitions $|n, l = 2, m = 0\rangle \leftrightarrow |n-1, l', m = 0\rangle$ of Rb Rydberg atoms the indicated values of l' vs principal quantum number n. The heavy dashed lines delineate the range of the transition frequencies of all transitions in the plot. For $n \sim 50$, all Rabi frequencies are large ($\gtrsim 100$ kHz for $B = h \times 500$ kHz), and the transition frequencies are in a range that is favorable for experimental studies.

to large radial matrix elements and Rabi frequencies exceeding those in the other rubidium examples presented in this thesis. As seen in figure 4.5 for an amplitude-modulation parameter $B = h \times 500$ kHz, Rabi frequencies exceeding 100 kHz can be achieved for all multipole transitions with $3 \leqslant l' \leqslant 6$. The transition frequencies, Ω_A, are in intervals $0.32/n^3 \lesssim \hbar\Omega_A \lesssim 0.34/n^3$, which for principal quantum numbers $n \sim 50$ are in a convenient range ($\sim$ 20 GHz). Experimentally, the transitions could be detected via state-selective electric-field ionization. While atoms in the initial (nD) state tend to ionize adiabatically, at electric fields of about $1/(16n^4)$ in atomic units, the higher-angular-momentum states tend to ionize non-adiabatically, at considerably higher electric fields [1]. This differential behavior should allow one to measure spectra of the transitions $nD \to (n-1)\, l'$, with $l' > 2$, as a function of

the modulation frequency Ω. In similar spectroscopy experiments between initial and final states that both ionize adiabatically, state selective field ionization can resolve the states in certain cases, as discussed in 5.4.

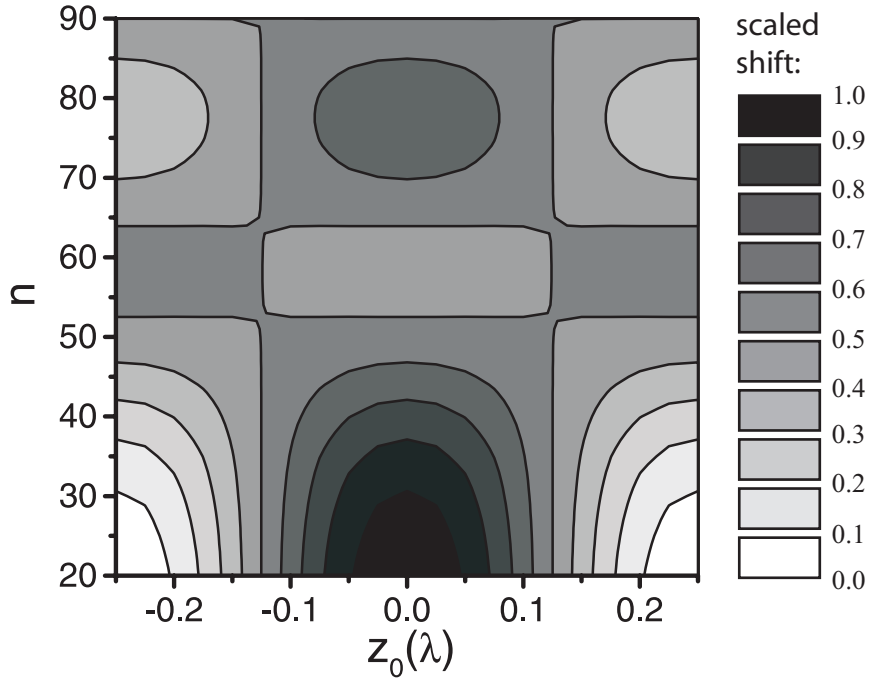

Figure 4.6: Level shift of the state $|nD, m = 0\rangle$ of Rb (scaled by $W^{\mathrm{Q,max}}$ from equation 4.15) in a ponderomotive potential with $B = 0$ and $A = W^{\mathrm{Q,max}}/2$ (factor of two change in scaling evident from equation 4.2 for the $B = 0$ case) and in equation 4.2. The shift ranges from 0 (white) to $W^{\mathrm{Q,max}}$ (black) and is displayed on a ten-point linear gray scale.

The time-averaged level shifts, $A\, D^{n,l,m}_{n,l,m}(z_0)$, represent effective potentials for the center-of-mass motion of Rydberg atoms in state $|n, l, m\rangle$. These potentials may be used to trap the Rydberg atoms [25]. In an electromagnetic transition driven by a modulated ponderomotive lattice, the transition energy is shifted from its unperturbed value, $\hbar\Omega_A = E_{n',l'} - E_{n,l}$, by the difference of the effective potentials of the initial and final states. The transition frequency is therefore shifted by $A\,(D^{n',l',m}_{n',l',m} - D^{n,l,m}_{n,l,m})/\hbar$. As an example, in Figs. 4.6 and 4.7 we analyze the transitions $nD \rightarrow (n-1)F$ and $nD \rightarrow (n-1)G$ of Rb.

Figure 4.6 shows the level shifts, $A\, D^{n,l=2,m=0}_{n,l=2,m=0}$, of the initial state in the transition,

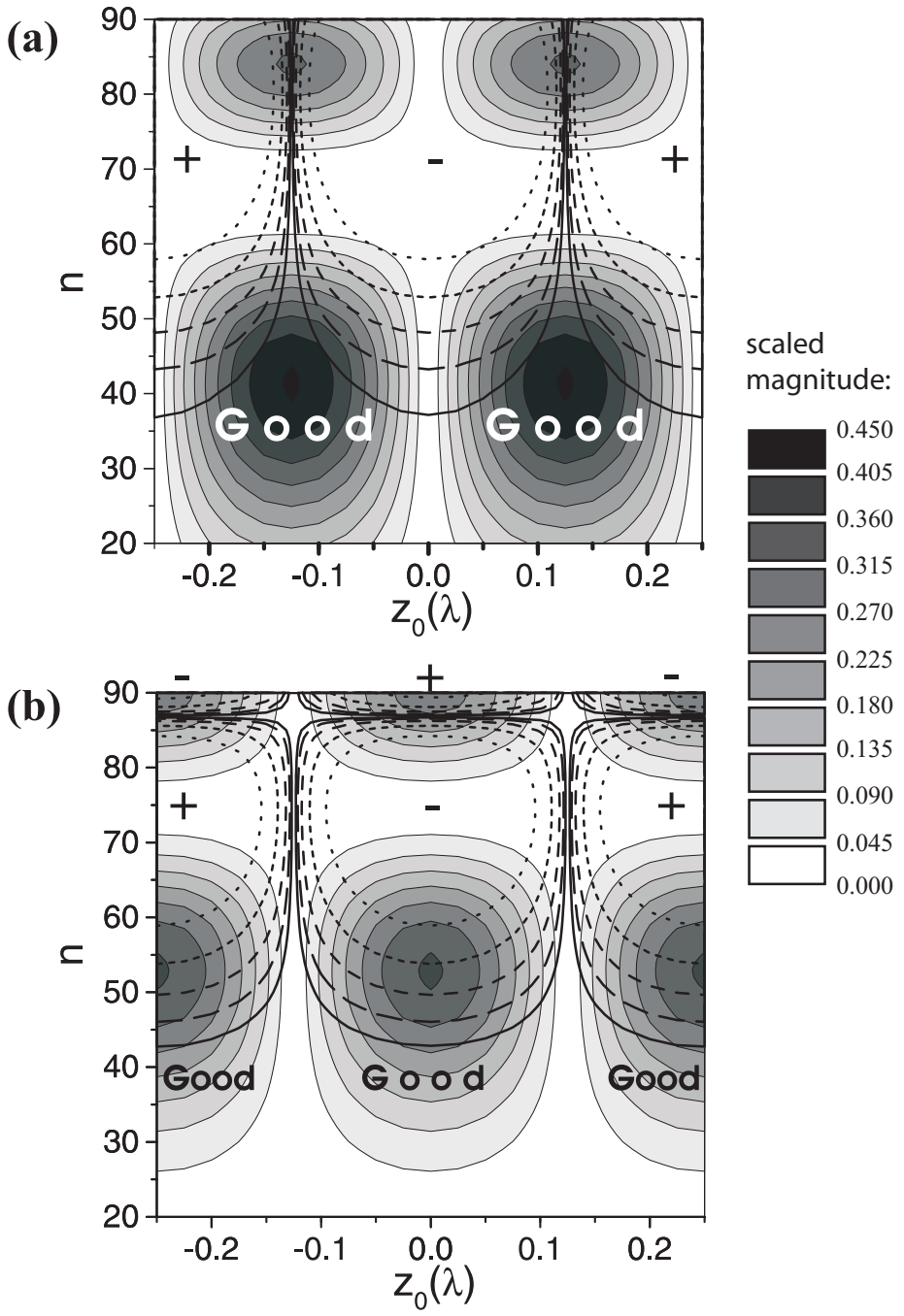

Figure 4.7: (a) Rabi frequencies $|\chi|$ (scaled by $B/h = W^{\mathrm{Q,max}}/4h$ from equation 4.15) for the case $A = B$ of the transition $|nD, m = 0\rangle \leftrightarrow |(n-1)F, m = 0\rangle$ of Rb Rydberg atoms. If we take the underlying amplitude-modulated ponderomotive lattice to have temporal modulation amplitude of $B = h \times 500$ kHz, the grayscale for the Rabi frequencies ranges from 0 (white) to 225 kHz (black). The overlaid lines indicate the frequency shift of the transition induced by the ponderomotive potential. For the case of $A = B = h\times$ 500 kHz, the scale is as follows: solid = 2.5 kHz, long-dashed = 5 kHz, dashed = 10 kHz, short-dashed = 20 kHz, dotted = 40 kHz). The + and - signs indicate the sign of the shift in various domains. (b) Same as (a) for the transition $|nD, m = 0\rangle \leftrightarrow |(n-1)G, m = 0\rangle$.

$|nD, m = 0\rangle$, vs. n and lattice position z_0. In the computation of $D^{n,l,m}_{n,l,m}$, the radial matrix element $(r^p)^{n,l}_{n,l} = 1$ for $p = 0$, and the term $p = 0$ in the p-sum in equation 4.7 does not vanish. (For this reason we have kept the $\delta_{p,0}$ in equation 4.7). For small n, the atoms are much smaller than the period of the ponderomotive potential, and consequently the shift is practically identical with the ponderomotive potential itself. At large n, the atoms are larger than the period of the ponderomotive potential, and the shifts are close the the spatial average of the ponderomotive potential ($\hbar \times 10^6$ rad/s in figure 4.6).

The shifts of the transition frequency, $A\,(D^{n',l',m}_{n',l',m} - D^{n,l,m}_{n,l,m})/\hbar$, are usually much lower than $A\,D^{n,l=2,m=0}_{n,l=2,m=0}/\hbar$ because Rydberg states that are close in energy tend to have have similar values of D. As seen in figure 4.7, domains exist in which the Rabi frequency exceeds $2\pi \times 50$ kHz while the transition shift is less than $2\pi \times 1$ kHz (domains labeled "Good"). Odd transitions are particularly favorable, because the maxima of the Rabi frequency coincide with locations where the transition shift vanishes (see, *e.g.*, figure 4.7 (a)). Also, for a sample of randomly placed atoms the transition shifts are equally likely to be positive or negative by same amounts (note the signs in figure 4.7). Thus, in spectroscopic measurements the transition shifts should mostly cause line broadening with little net shift.

4.6 Summary

In this chapter, we have investigated the effects of making the perturbation caused by the ponderomotive interaction time-dependent. In particular, we examined resonant transitions of Rydberg atoms in amplitude-modulated standing-wave ponderomotive potentials. We have found that such potentials are suited to drive multipole transitions up to high order. For changes in the angular-momentum quantum num-

ber up to about five and for realistic laser parameters, we find Rabi frequencies on the order of 100 kHz, which should be sufficient to observe them experimentally. Varying the amplitude-modulation frequency of the standing-wave ponderomotive potential, it should be possible to obtain spectra of many multipole transitions and to determine atomic parameters, including quantum defects for fairly high angular momenta. In contrast to the direct application of microwave radiation, the method has high spatial selectivity, because the modulated light fields giving rise to the ponderomotive potential can be focused to a spot size of a few μm. This property may become useful in future applications where localized coherent interactions between Rydberg atoms are of interest, such as in quantum information processing. In the next chapter, we discuss experimental progress toward studying both the time-independent aspects of the ponderomotive interaction with a Rydberg atom discussed in chapter III and the time-dependent aspects (driving resonant transitions with modulated ponderomotive optical lattices) discussed in this chapter.

CHAPTER V

Rydberg Atoms in Ponderomotive Potentials - Experiments

In this chapter, we discuss the techniques developed for use in experiments probing the ponderomotive interaction between a Rydberg electron and an applied optical field. Additionally, strategies for probing various aspects of the interaction, including transitions induced by amplitude-modulated lattice potentials and Rydberg atom trapping in a 1D lattice, are proposed.

5.1 Preparating Cold Rydberg Atoms

In this section, we discuss the preparation of cold Rydberg atoms for use in ponderomotive optical lattice experiments. The atoms first undergo a two-stage laser-cooling scheme to remove excess kinetic energy that can cause unwanted motional effects in lattice experiments (see section 5.6). Once the atoms are cooled, a two-photon laser excitation sequence transfers population from the ground state to a Rydberg state. In initial experiments, we are primarily interested in the interaction of the applied ponderomotive optical lattice and the Rydberg atom. Therefore, we excite atoms at low densities in order to minimize the effects of Rydberg-Rydberg interactions.

To begin, ^{85}Rb is cooled and trapped in a pyramidal low-velocity intense source (LVIS) [38] that forms a beam of cold, slow atoms that is recaptured in a six-beam

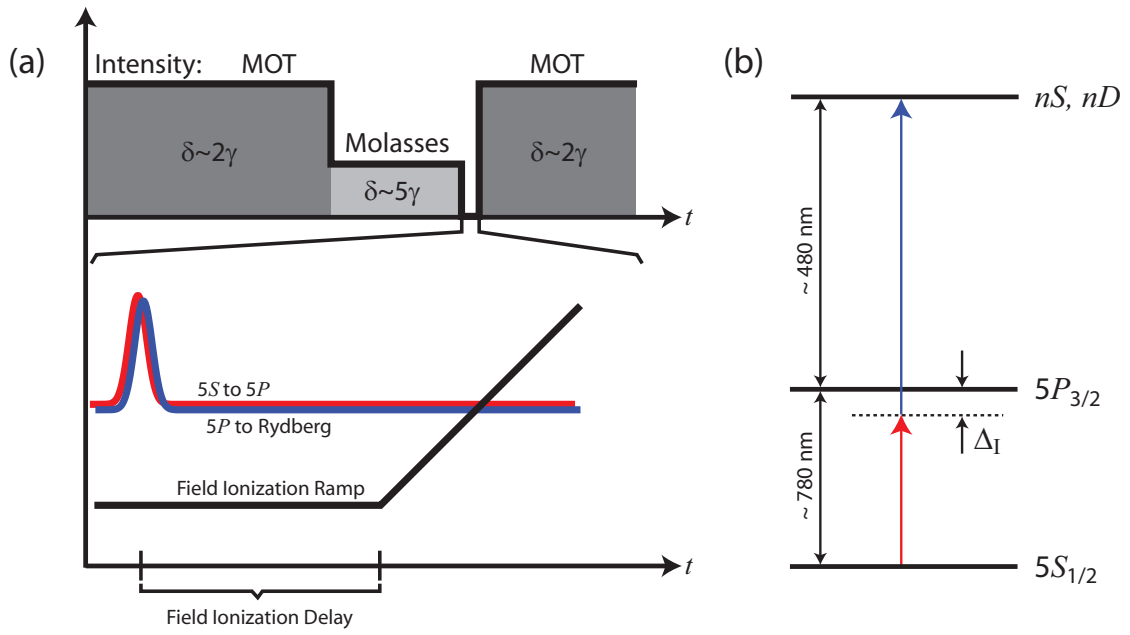

Figure 5.1: Timing sequence for laser-cooling and Rydberg atom experiments (a) and Rydberg excitation energy level scheme (b).

magneto-optical trap (MOT). The MOT is located at the geometric center of the electrode stack as shown in figure 1.2. The typical magnetic field gradient for a MOT is about 20 G/cm; however for the experiments described in this section, we operate at a low gradient of 1-2 G/cm. The low gradient magnetic field configuration allows substantial sub-doppler cooling without switching the magnetic field coils, while providing sufficient atomic densities to achieve the desired number of Rydberg atoms for our experiments. Figure 5.1(a) shows the intensity and detuning from the $5S_{1/2}$ to $5P_{3/2}$ resonance of the laser-cooling beams for the MOT. The MOT cooling phase utilizes laser intensities and detunings appropriate for efficient loading and cools atoms to near the Doppler limit. During the molasses phase, the laser is red-detuned from the MOT cycling transition resonance by about five linewidths ($\approx$ 30 MHz). At the same time, the intensity of the trapping light is reduced. For the low-gradient MOT, significant sub-doppler cooling occurs in the large-detuning, low-intensity limit. For the polarization employed in the MOT ($\sigma_- - \sigma_+$), the sub-

doppler cooling mechanism is known as a cork-screw molasses since the polarization gradient cooling arises from the rotating orientation of the resultant linearly polarized light [82]. The intensity level for the molasses phase is adjusted to minimize the temperature of the atomic sample. The temperature of the atomic distribution is reduced from the Doppler temperature of the MOT phase (≈ 150 μK) to its lower, steady-state temperature (≈ 30 μK) in $\lesssim 3$ ms, at which time the trapping light can be turned off and experiments are performed. When the trapping light is off, the atomic distribution will expand. The rate of the expansion can be measured and related to the temperature. This is done by measuring the density profile of the sample at various times during the expansion as shown in Fig 5.2.

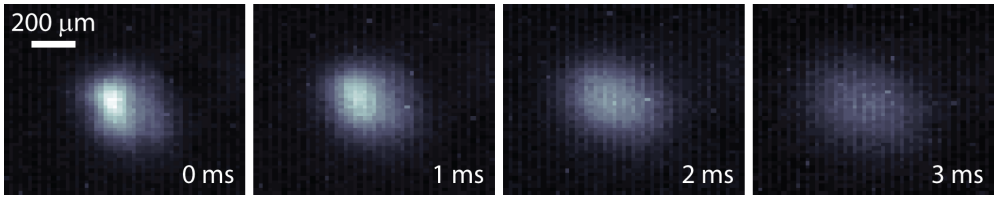

Figure 5.2: Fluorescence images of atomic sample after various time intervals of free expansion.

Assuming a thermal velocity distribution and self-similar Gaussian expansion, the standard deviation of the spatial distribution has the form $\sigma(t_f) = \sqrt{\sigma^2(0) + v^2 t_f^2}$, where t_f is the time interval over which the cloud expands. The thermal velocity (in 1D) $v = \sqrt{k_B T/M}$ relates $\sigma(t_f)$ to the temperature T of the atomic sample. Fig 5.2(a) shows fluorescence images of the atomic distribution at various times during its free expansion. From the expansion of the sample, we infer a temperature of 30 μK after the molasses phase compared to the roughly 150 μK Doppler temperature characteristic of the MOT. As a final note, the temperature in this type of molasses ($\sigma_- - \sigma_+$) is dependent on stray bias magnetic fields, and thus tuning three pairs of magnetic field compensation coils were required to reach this 30 μK mark.

After the laser-cooling process has reduced the temperature of the atoms sufficiently, the trapping light is switched off, and Rydberg atoms are then created via a two-photon excitation from the $5S_{1/2}$ ground state to a Rydberg state as shown in figure 5.1(b). Photons from two narrow band sources (one at ≈ 780 nm and the other at ≈ 480 nm) effect the transition. This transition can proceed resonantly through the $5P_{3/2}$ intermediate state or with a detuning Δ_{I} with respect to the intermediate state, such that the population is restricted to the ground and Rydberg states. In the limit of no saturation, the linewidth of the excitation process is typically on the order of 6 MHz.

Since the excitation proceeds via a two-photon excitation from the $5S$ ground state, the initial Rydberg states coupled are nS and nD states. However, by applying small electric fields, other states (*e.g.*, nP states) can be laser-excited. Additionally, circular states, which are of particular interest for their long lifetimes and high-precision spectroscopy potential [1, 70], can be laser-excited in dynamic crossed electric and magnetic fields [83]. For initial experiments involving Rydberg atoms in ponderomotive optical lattices, we focus on preparing Rydberg atoms in nS states. Using nS states simplifies matters for a few reasons. First, the S states are less sensitive to stray electric and magnetic fields, which practically elimates broadening in microwave spectra between neighboring S states (as discussed in section 5.4). The nS state is a spherically symmetric $m = 0$ state. Since the 1D ponderomotive optical lattice does not couple states of differing m, level shifts and Rabi frequencies in the optical lattice are not subject to the "orientational" effects discussed in section 4.5. Finally, the nS states over the n-range of interest ($45 < n < 75$) exhibit relatively small, repulsive binary interactions with other nS Rydberg atoms, as compared to nD Rydbergs states' larger and attractive interactions, which can lead to collisions

as discussed in chapter II. Thus, the choice of nS states helps isolate the Rydberg-Rydberg interaction effects from the Rydberg-ponderomotive potential interactions of interest.

In the interval of time between the Rydberg excitation sequence and the application of the field ionization ramp, the Rydberg atoms can be subjected to a combination of ponderomotive potentials and microwave probes. In experiments designed to probe the ponderomotive shift of the Rydberg energy levels, a standing wave lattice creates the shift and a microwave probe is applied to measure the effect. In experiments geared toward driving multipole transitions with an amplitude-modulated lattice, the applied lattice is modulated at appropriate microwave frequencies (by applying microwaves to an electro-optic modulator as shown in figure 5.3). In any case, the Rydberg atoms are field ionized after exposure to the external fields to determine the final distribution of Rydberg states.

5.2 Creating a Ponderomotive Optical Lattice Potential

In this section, we discuss the experimental setup of the ponderomotive optical lattice, which is the standing wave formed by a focused, retro-reflected 1064 nm laser beam as shown in figure 5.3. The ponderomotive optical lattice itself refers to the roughly cylindrical volume where the standing wave intersects the MOT. A properly aligned lattice corresponds to the case where the focus of the incident lattice beam coincides with the focus of the return lattice beam at the location of the atomic distribution. Additionally, the incident and return beam must interfere efficiently and have sufficient intensity to achieve measurable effects from Rydberg level shifts and Rabi frequencies according to the descriptions in chapters III and IV.

The laser source used for the lattice is a 1064 nm fiber laser (P/N: YLR-10-1064-

LP-SF, IPG Photonics) which produces up to 10 W of linearly polarized output with quoted linewidth of $\Delta\nu = 70$ kHz. The coherence length of the output beam $l = c/\Delta\nu \approx 4$ km. The path length difference over which the return beam is to interfere with the incoming beam to form a standing wave is $\lesssim 1$ m. To verify this interference experimentally, the Michelson interferometer (shown in the right dashed box in figure 5.3) interferes the incident (split to the M3 arm) and return (propragates to the M2 arm) beams on the photodiode detector, PD, over a path length difference of ≈ 2 m. The resulting visibility $(I_{\max} - I_{\min})/(I_{\max} + I_{\min})$ measured is over 90 %.

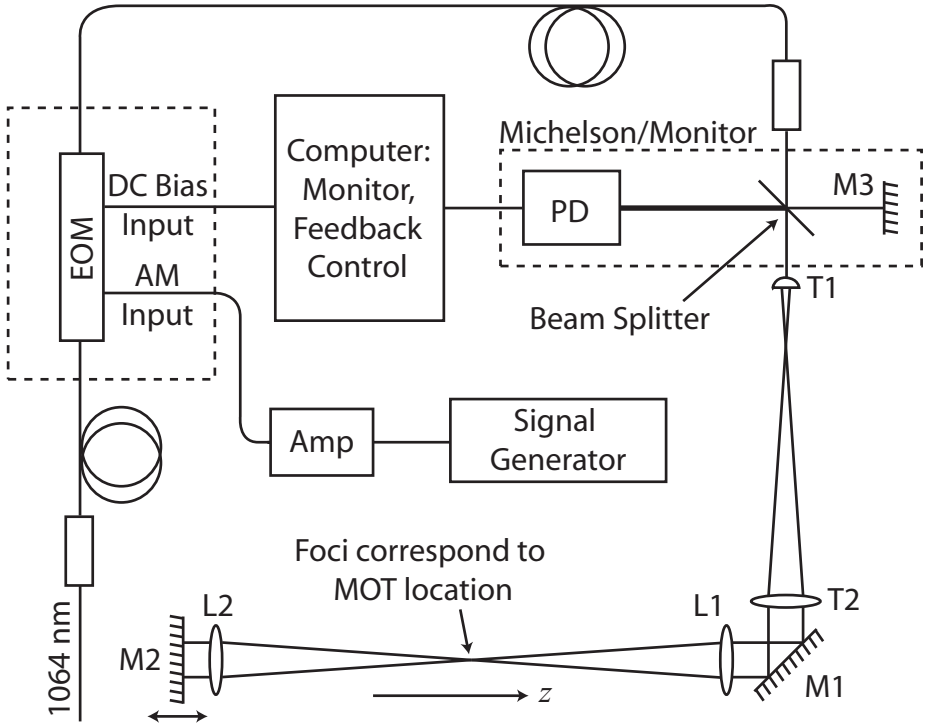

Figure 5.3: Schematic diagram of the ponderomotive optical lattice experimental setup.

The Michelson can also be used to measure the temporal phase stability of the optical standing wave. Mechanical vibrations of the optical elements that make up the Michelson interferometer cause the phase of the interference sampled at the photodiode to vary continuously over a range that is substantially larger than 2π. The timescale over which the phase changes by less than 10 % (of 2π) is on the order of

50 μs. Since more optical elements in the interferometer are contributing to the phase noise than are used to form the lattice, this measurement represents a lower limit on the phase stability of the lattice. Many Rydberg atom experiments, especially those of interest initially, can be performed on timescales under 50 μs, over which time the lattice is phase-stable. Experiments occurring over longer timescales, such as spectroscopic probes of long-lived circular Rydberg states, may require additional mechanical stability or active phase-stabilization.

The lattice light is delivered to the experiment through a fiber optic cable whose output is roughly collimated by a short focal length aspheric lens. The diagram shows the light passing through an electro-optic modulator, which is the case for experiments involving amplitude-modulated ponderomotive optical lattices. Since the throughput of the modulator is limited to about 200 mW of cw power, the modulator is replaced by polarization maintaining fiber for experiments requiring more power. As is discussed in the next section, 780 nm light is often coupled into the fiber together with the 1064 nm light. To ensure single mode operation at both wavelengths, a fiber optimized for operation near 850 nm is suitable.

After the fiber collimator, the Gaussian beam is then expanded to full width at half maximum of ≈ 30 mm using a telescope formed by lenses T1 and T2. A focal spot size of $x_{\mathrm{FWHM}} = 15$ μm is achieved using focusing lens L1 with a focal length of 30 cm. The focal length of L1 is chosen to be 30 cm, so that the lens can sit just outside the vacuum chamber. The focal spot has been characterized using a CCD camera with 6.7 μm pixel size. The focal spot characterization also confirms that the intensity profile of the beam at the focal spot is essentially Gaussian. Use of two inch optics for elements T2, M1, L1, L2 and M2 is required to avoid diffractive effects (*e.g.*, doughnut shaped intensity profiles) at or near the focus resulting from clipping

the beam. Additionally, high numerical aperture fiber output collimation, such as that provided by a short focal length aspheric collimation package, is required to avoid these aperture effects.

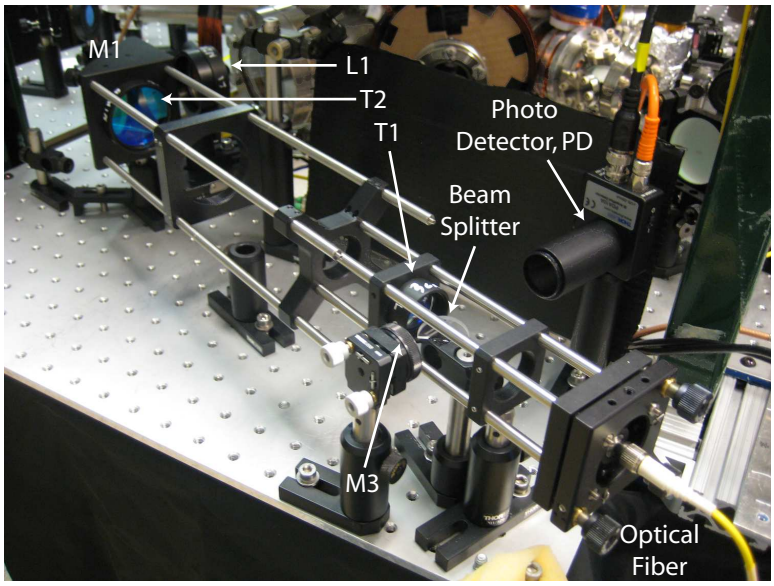

Figure 5.4: Picture of ponderomotive optical lattice optics used to monitor the lattice beam and focus it into the MOT with the appropriate spot size.

The Rayleigh length has been also been measured to be $\lesssim$ 1 mm. Since the diameter of the MOT is about 500 μm, the width of the lattice beam will be uniform across the atomic distribution for the case of a well-aligned lattice. The Rayleigh length also determines the sensitivity of the alignment of the lattice to the positions of lenses L1 and L2. The first step to locating the position of L1 and L2 is to determine the effective focal length of the lens system {T1, T2, L1}. This effective focal length can be set by adjusting the collimation of the beam after the the telescope T1:T2 and determined by accurately measuring the distance between L1 and the resulting focus. The telescope T1:T2 and focusing lens L1 should then be transferred to the experiment without changing the distance between T1 and T2. L1 is placed at a distance equal to the measured effective focal length of lens system {T1, T2,

L1} from the expected MOT location (assumed to be the geometrical center of the chamber). L2 can be roughly located by placing it such that it collimates lattice beam.

Placing L1 and L2 on translation stages streamlines the fine tweaking process, which is accomplished via laser spectroscopy of the light shift on the Rydberg excitation sequence. The nature of these shifts is described in sections 3.3 and 3.4. The fine alignment begins by adjusting the location of L1 with the return beam blocked. This creates conditions equivalent to that for which the data taken in figure 3.4 was obtained. When the focal spot corresponds to the location of the atoms, the high-frequency cutoff of the spectrum (see figure 3.4) will be maximal. If the position of the lens is one Rayleigh length from the optimal position, the shift will be reduced by a factor of two. Thus, this method provides an accurate way to place L1.

After L1 is in place, the return beam should be unblocked, and the retro-mirror M2 should be adjusted such that the lattice beam is maximally coupled back into the fiber. Again, we turn to laser spectroscopy techniques to finely adjust the position of L2. Interpreting the spectrum, in this case, will be somewhat more complicated than in the running wave case because the shift will reflect the inhomogeneity of the applied lattice field, which could also have some significant running wave component. The situation can be simplified by exciting to lower Rydberg states near $n = 40$ where the shift reflects the local lattice intensity. In this case, the position of L2 can then be adjusted by again maximizing the position of the high frequency cutoff as in the alignment of L1.

5.3 Preparing Rydberg Atoms in a Ponderomotive Optical Lattice

One important experimental challenge is localizing Rydberg excitations to within a volume subjected to the externally applied ponderomotive optical lattice. Spurious Rydberg excitations external to the lattice volume reduce the signal-to-noise ratio for any experiments in which we attempt to probe the effects of the lattice. In this section, we discuss schemes for creating Rydberg atoms in a volume that intersects the applied ponderomotive potential and limiting these excitations to that volume. In some cases, it may also be possible to have some control over the location of Rydberg excitations within this volume using spatially inhomogeneous light shifts. The production of Rydberg atoms procees via a two-photon excitation process, requiring one photon at 780 nm ($5S$-$5P$) and one at 480 nm ($5P$-Rydberg). These photons come from two different laser sources, which are focused separately into the atomic sample at a 45° angle relative to one another such that Rydberg excitations can be created in the intersection volume of these two beams as shown figure 5.5.

The red $5S$-$5P$ beam is coupled into the same fiber as the 1064 nm ponderomotive optical lattice beam. This ensures that the two beams propagate colinearly. One advantage of this arrangement is that the $5S$-$5P$, which interacts strongly with atoms in the ground state, can be used to direct the optical lattice beam through the center of the ground state atom distribution by observing the effects of the colinearly propagating $5S$-$5P$ laser on the MOT. Next, the 5S-5P and optical lattice beam overlap in space. Figure 5.5 depicts how these to beams overlap assuming the focusing optics shown in figure 5.3. Due to chromatic aberrations in this optical system, the $5S$-$5P$ focal spot lies about 5 mm nearer to L1 than the optical lattice focal spot. Thus, the full width at half maximum of this beam is about 150 μm at the location

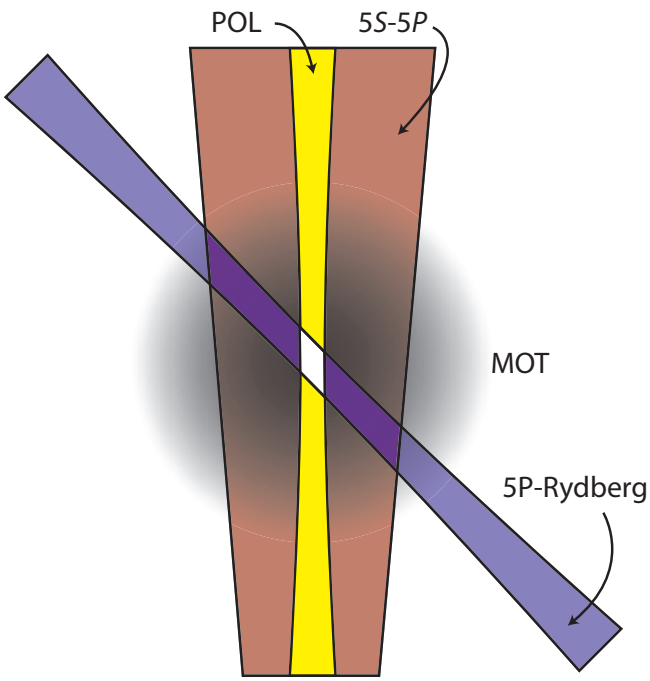

Figure 5.5: Diagram of Rydberg excitation (red and blue) and ponderomotive optical lattice (yellow) laser beams and intersection regions (purple and white). The atomic distribution is shown in a grayscale.

of the lattice beam focus which has a 15 μm width. The blue $5P$-Rydberg laser is focused to a 25 μm width. Therefore, the ponderomotive optical lattice potential intersects only about 5 % of the total Rydberg excitation volume defined by the intersection of the two Rydberg excitation lasers and the MOT.

In order to increase the signal-to-noise in the lattice, the volume mismatch between the Rydberg excitation region and the ponderomotive optical lattice must be reduced. One way to achieve this is by using the light shift from the optical lattice potential to spatially modulate the resonant frequency for Rydberg excitations as discussed previously (see sections 3.3 and 3.4). In this case, the distribution of Rydberg excitations can be determined by tuning the sum frequency of the two-photon Rydberg excitation sequence. For this procedure, two-photon excitation, which proceeds off-resonantly with respect to the intermediate state, is advantageous since it isolates the sum frequency light shift from the spatial modulation of the $5S$ to $5P$ res-

onance frequency. A convenient excitation scheme for ^{85}Rb used in our experiments involves stabilizing the $5S$-$5P$ laser frequency to the near ^{87}Rb ($F = 2 \rightarrow F' = 3$)cycling transition ($\Delta_{\mathrm{I}} \approx 1.5$ GHz red detuned) while scanning the $5P$-Rydberg laser frequency over the sum frequency resonance. This method should work quite well for high-intensity lattice experiments such as those investigating the energy level shifts caused by ponderomotive optical lattices. For experiments involving lower-intensity lattices, such as driving transitions using amplitude-modulated ponderomotive optical lattices, the light shift on the Rydberg state is reduced significantly, so the ability to localize transitions using the spatially modulated light shift is correspondingly reduced.

Another perhaps more straightforward approach to spatially localizing the Rydberg excitations to a volume corresponding to the ponderomotive optical lattice is to address the chromatic aberration in the optical system that leads to the focusing mismatch of the $5S - 5$P and lattice beams. At the output of the fiber, these beams are polarized linearly and orthogonally with respect to one another. This configuration suggests the use of a birefringent lens, which could be designed with a differential focal length for two orthogonal axes appropriate for compensating the chromatic aberration in this lens system. Such a lens could be incorporated into the system (replacing, *e.g.*, L1 in figure 5.3) such that the $5S$-$5P$ and lattice beams focused at the same distance from L1. In this case, the focal spot of the $5S$-$5P$ beam would be slightly smaller than that of lattice beam (by a factor of $\approx 780/1064$). In this way, the Rydberg excitations would be confined to a volume that coincides well with the high intensity axis of the Gaussian plane wave ponderomotive optical lattice potential.

5.4 Microwave Spectroscopy Techniques

As discussed in section 3.4, microwave spectroscopy of transitions between neighboring Rydberg states is a potentially useful tool for investigating the ponderomotive interaction with a Rydberg electron. In general, precision microwave Rydberg spectroscopy requires a high degree of control over external fields due to the Rydberg atom's sensitivity to these fields. In certain cases, however, the states can be chosen such that the transition frequency is quite insensitive to perturbing fields. The nS to $(n+1)S$ Rydberg transition is a useful instance of this type of transition that is relatively insensitive to external fields. For experiments performed in a MOT, utilizing this type of transition is essential since the inhomogeneous fields of the MOT would tend to broaden and split spectral line profiles. In this section, we focus the discussion on the microwave spectroscopy of the nS to $(n+1)S$ transition in a MOT.

Figure 5.1(a) shows the timing diagram for a typical Rydberg atom experiment. In microwave spectroscopy applications, microwaves are applied to the Rydberg atoms in the interval of time between the photo-excitation and state selective field ionization. In our experiments, microwaves are delivered to the Rydberg atoms via a horn placed outside the vacuum chamber at a distance of about 40 cm for the MOT. The horn directs radiation onto the Rydberg atoms through large glass viewports. The chamber and electrodes do shield the atoms from the radiation to some degree, but a sufficient amount impinges on the atoms to transfer population efficiently between Rydberg states.

After the application of microwaves, a field ionization ramp is applied to determine the Rydberg state distribution. For spectroscopy between neighboring Rydberg states, states must be chosen such that the initial and target states are resolvable

in the field ionization spectrum. Since the energy spacing of the initial and target states for many experiments of interest is less than 40 GHz, the ionizing fields will not differ by a large amount. In this case, certain states are distinguishable in field ionization spectra while others with similar energy separation are not.

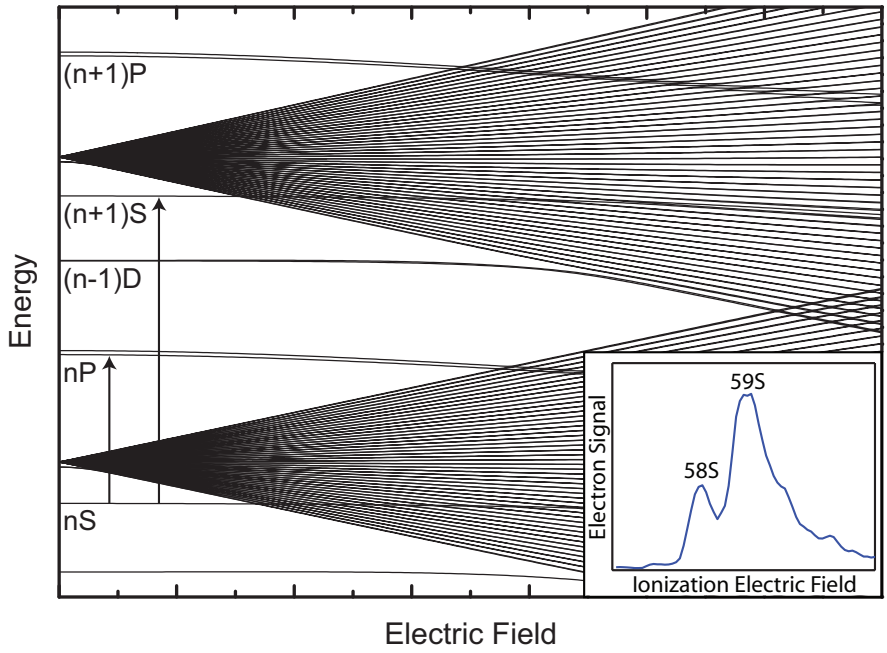

Figure 5.6: Rydberg energy level structure as a function of applied electric field (Stark map). The zero field state labels are shown for some of low angular momentum states, which are separated from the degenerate hydrogenic manifolds because of their quantum defects. Inset shows field ionization signal for two states which are nearby in energy yet resolvable in the spectrum.

With our electric field ionization ramps (slew rates in the 20 V/μs range), the low-angular-momentum states (S, P, and D) traverse the Stark map adiabatically, meaning that the zero-field energy ordering of the states is preserved as the electric field is increased and states are ionized [1]. Thus, the energy of states between two hydrogenic fans will tend to converge as the electric field is increased and subsequently ionize at similar electric fields (see figure 5.6). Meanwhile, the energy splitting of states separated by a hydrogenic fan tend to increase, subsequently ionizing at distinct electric fields (see figure 5.6). Note, the nS and nP states appear to cross the

hydrogenic states in figure 5.6. At low fields the coupling is weak, but it grows with electric field and the states are deflected as just described. The inset shows the field ionization spectrum for the latter case for an nS to $(n+1)S$ transition. These are clearly distinguishable while the $(n+1)S$ to nP, for example, would not be. The nS to nP field ionization signals would also be distinguishable.

In order to obtain a microwave spectrum for a Rydberg transition, the experimental sequence shown in figure 5.1 is used with microwave radiation at given frequency applied in the time interval between Rydberg excitation and field ionization. Two gates of a photon counter counting pulses from the micro-channel plate detector are used to determine (Gate A) the total number of counts and (Gate B) the number of counts corresponding to population in the target state of the Rydberg transition. Using the information from these gates, the fraction of population transferred to the target state is determined at a particular frequency. By repeating this process over a range of frequencies, the target state population fraction (Gate B / Gate A) as a function of microwave frequency, which corresponds to the spectral line of the Rydberg transition, can be constructed.

Figure 5.7 shows spectra recorded in this way for the $58S \rightarrow 59S$. This is a two-photon transition resulting from the absorbtion of two photons from a single frequency source. The frequency displayed on the x-axis in figure 5.7 is the frequency of the source. This transition can be described fairly well by the solution to the two-level Rabi problem (see, *e.g.*, section 3.3 of reference [84]). Following this reference and assuming the population starts in the initially laser-excited state, the target state probability is given by

$$|c_{\text{target}}(t)|^2 = \frac{\chi^2}{\delta^2+\chi^2}\sin\left(\frac{\sqrt{\delta^2+\chi^2}}{2}t\right) \tag{5.1}$$

where χ is the Rabi frequency of the transition (as in equation 4.11) and δ is the

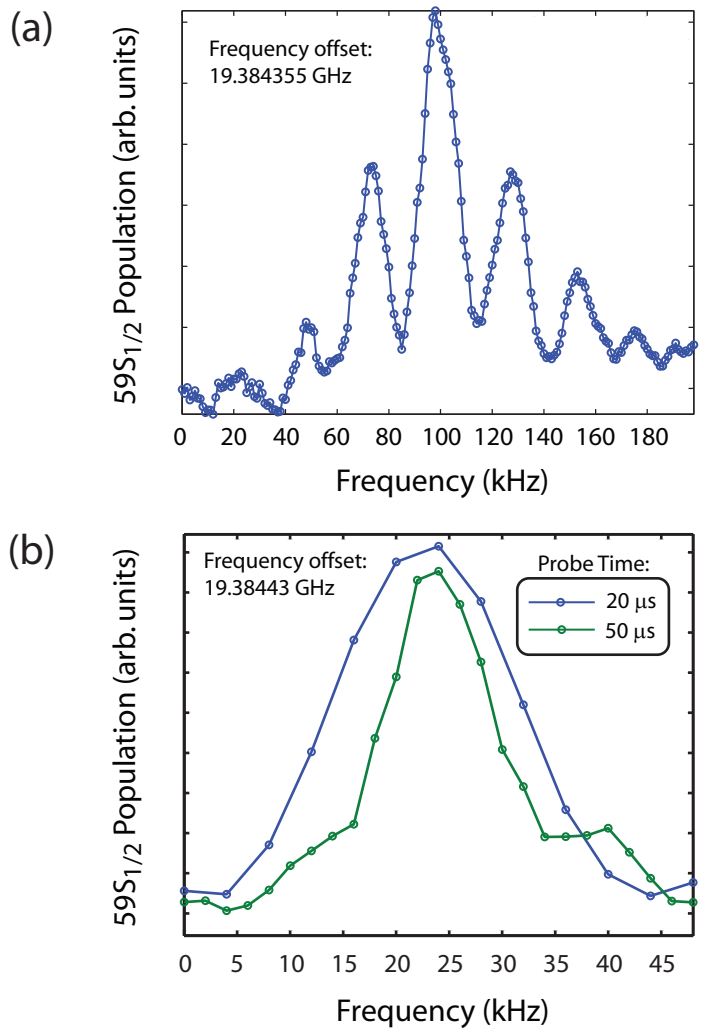

Figure 5.7: Microwave spectra for the Rydberg transition $58S \rightarrow 59S$ for (a) a relatively large Rabi frequency ($\approx$ 100 kHz) and (b) intensities yielding a Rabi frequency about a factor of five smaller than in (a).

detuning from resonance. While this model succeeds in describing the basic features of the microwave spectra in figure 5.7, it is based on a one-photon transition. For a more rigorous treatment of the two-photon Rabi problem based on three-level system where the two-photon transition proceeds off-resonantly through the intermediate state (which would be $58P$ for the $58S \rightarrow 59S$ transition) see reference [85].

The spectrum in figure 5.7(a) is typical of microwave spectra on this transition for a nominal microwave output of around -20 dBm directed onto the Rybderg atoms as described above. The field ionization delay (see figure 5.1), which is the same

as the microwave interaction time, for this spectrum was 20 μs. In this parameter range, equation 5.1 predicts the presence of substantial side peaks and a central peak magnitude which is strongly modulated as a function of the Rabi frequency (*i.e.*, applied microwave power) and microwave interaction time t. This strong modulation is also observed experimentally in response to varying these parameters.

The spectra in figure 5.7(b) were taken at a microwave power of about -27 dBm (low intensity limit). The blue and green spectra were taken for two different microwave interaction times. The scale of the frequency axis has been reduced to show the central feature. Note, the relative magnitude of the side peaks are substantially smaller in the low-intensity limit than at higher intensities. The spectral width of the transition is strongly dependent on the length of the microwave interaction time. The blue spectrum was taken for a 20 μs interaction time and has a width of about 25 kHz, which is essentially transform limited. The green spectrum was taken for 50 μs interaction time and has a width of about 15 kHz, which is only slightly larger than the transform limit.

The spectral widths of these transitions are nearly transform limited in spite of the presence of perturbing electric and magnetic fields. The insensitivity to stray electric fields results from the similarity in the polarizabilities of neighboring S states. The energy levels of the nS and $(n+1)S$ states would both be shifted by by similar amounts such that the differential level shift is quite small. The spectral profile of the $nS \rightarrow (n+1)S$ transition also shows no discernable effect from the 2 G/cm magnetic field gradient from the MOT trapping fields. The presence of a small magnetic field splits the both the nS and $(n+1)S$ levels into two levels each due to the interaction of the electron spin with the external field. Since the Landé g-factor of the two states is the same and the radiation field does not couple states

of opposite spin, the transition frequency is unperturbed by the magnetic field. A similar argument can be made for the apparent magnetic field insensitivity of other two-photon transitions of the type $nL \rightarrow (n+1)L$ (see reference [28]).

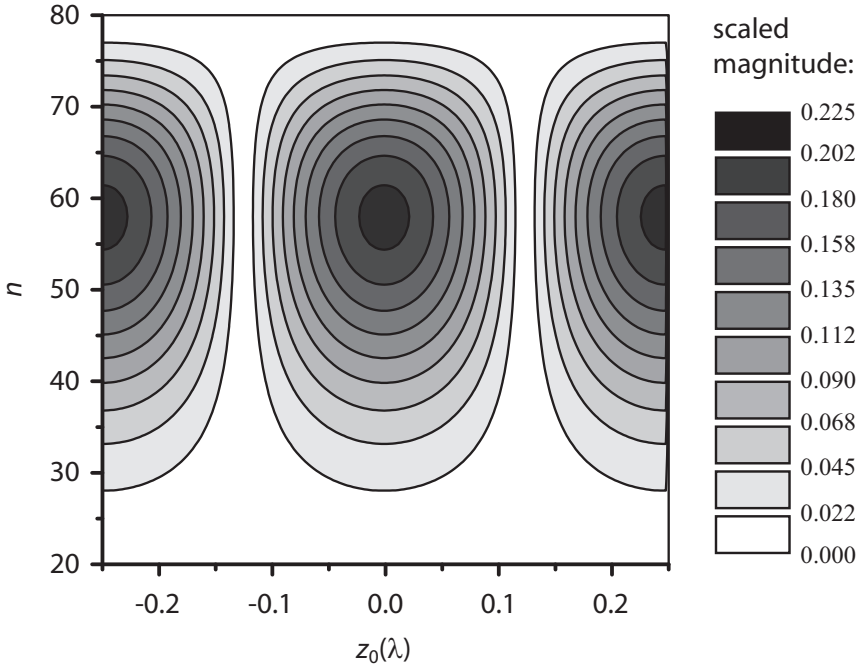

Figure 5.8: Rabi frequencies $|\chi|$ (scaled by $B/h = W^{\mathrm{Q,max}}/4h$ from equation 4.15) of the transitions $nS \leftrightarrow (n+1)S$ vs principal quantum number, n, and lattice position, z_0. If we take the underlying amplitude-modulated ponderomotive lattice to have temporal modulation amplitude of $B = h \times$ 500 kHz, the grayscale for the Rabi frequencies ranges from 0 to 112 kHz.

In figure 5.8, we present the Rabi frequency plot (see discussion in chapter IV) for the $nS \rightarrow (n+1)S$ transition in an amplitude modulated ponderomotive optical lattice. Rabi frequencies of order 100 kHz have been calculated for anticipated experimental conditions. This Rabi frequency compares favorably with the measured spectral widths of this transition in figure 5.7. Thus, it should be possible to transfer significant population from the initial to the target state using the amplitude-modulated lattice. The spectral width of the $53S \rightarrow 53P$ transition is broadened to about 5 MHz by external fields (see figure 5.9). Since anticipated Rabi frequencies are significantly smaller than the broadened linewidths of these transitions, transfer

of significant population to the target state in this case would not be possible. This contrast highlights a significant advantage of working with the $nS \rightarrow (n+1)S$ transitions for initial demonstrations of driving transitions with an amplitude-modulated ponderomotive optical lattice.

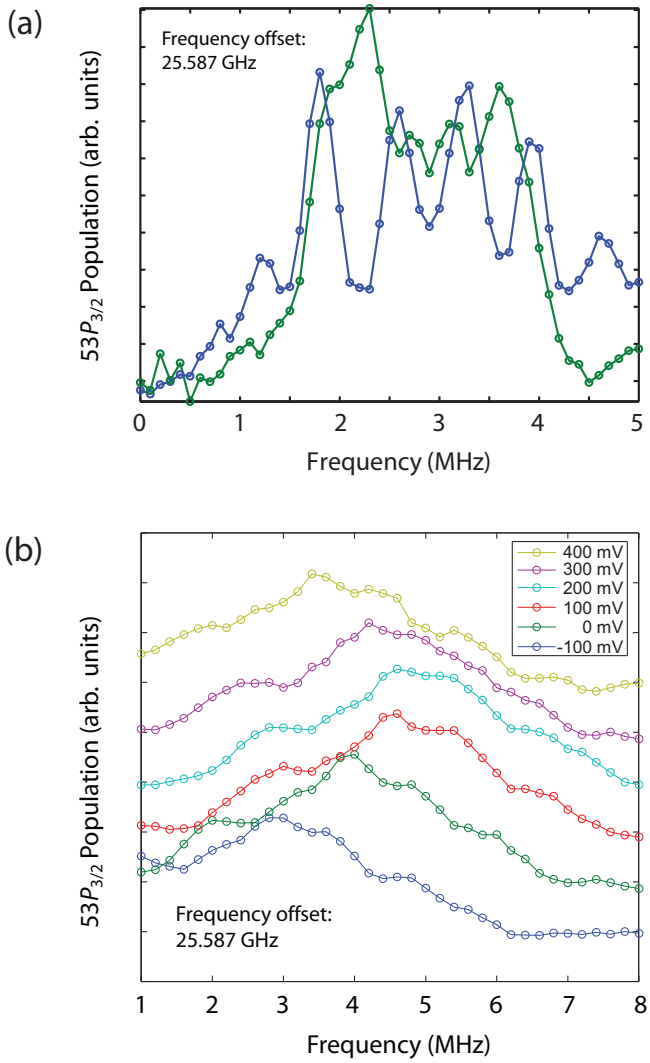

Figure 5.9: Microwave spectra for the Rydberg transition $53S \rightarrow 53P$ for varying magnetic fields (a) and electric fields (b).

Figure 5.9 shows microwave spectra taken on the $53S_{1/2} \rightarrow 53P_{3/2}$ transition. The line profile in (a) is split into six separate lines. The presence of small magnetic fields splits the $53S_{1/2}$ states into two states corresponding to the two electron spins while the $53P_{3/2}$ splits into four states. Due to differing g-factors of the $53S_{1/2}$ and $53P_{3/2}$

states, the dipole selection rules allow for six distinct transition frequencies, which are clearly evident in the blue spectrum in figure 5.9(a). After adjusting magnetic field compensation coils, the splitting can be significantly reduced as seen in the green spectrum in figure 5.9(a). Switching off the MOT magnetic field ($\approx$ 2 G/cm gradient) would further reduce the linewidth and will be required to reach linewidths in the range of 100-200 kHz.

The magnitude of the electric polarizability of the $53P$ state is significantly larger than the polarizability of the $53S$ state (see equation 3.20), and the quadratic Stark shift of these states is to lower energy. Thus, the presence of small electric fields effects a substantial net transition frequency shift which reduces the transition frequency as the field strength increases. This can be seen clearly in the Stark map in figure 5.6 and is demonstrated experimentally in figure 5.9(b). In these spectra, the voltage on the MCP semi-circular electrode (see figure 1.2) is held at various voltages shown in the legend. A voltage difference of 100 mV between the this electrode and the LVIS semi-circular electrode corresponds to an electric field of $\approx$ 26 mV/cm at the location of the MOT. The electric field experienced by the atoms is minimized when the center frequency of the spectral line is maximized. In the experiments in figure 5.9(b), the maximum value of the center frequency occurs between 100 mV and 200 mV. Using this method, the electric field component defined by the geometry of the electrode pair can easily be minimized to less than 10 mV/cm.

5.5 Amplitude Modulating a Ponderomotive Optical Lattice

In chapter IV, we discussed inducing transitions in Rydberg atoms by resonantly amplitude-modulating the ponderomotive optical lattice in which they were immersed. To provide this intensity modulation of the applied optical field, which

must be highly tunable over a range of tens of GHz, we use a broadband, fiber-coupled, lithium niobate electro-optic modulator (P/N: AZ-AV1-40-PFA-PFA-106-UL-S, EOSPACE, Inc.). In this section, we discuss techniques appropriate for using this device to modulate the output over a range of frequencies with close to 100 % temporal modulation depth.

The modulator listed above is a Mach-Zehnder type, polarization maintaining, z-cut, lithium niobate modulator which operates from DC to 40 GHz at peak powers up to about 200 mW. Additionally, it has the following specifications: 2.0 dB optical insertion loss, $V_\pi(1\text{ GHz}) = 3.2$ V, DC bias $V_\pi(0) = 1.2$ V, and a 19 dB extinction ratio. At 40 GHz, the frequency response of the modulator is down about 3 dB compared to the 1 GHz response, which smoothly decreases by this 3 dB amount over the range of operating frequencies.

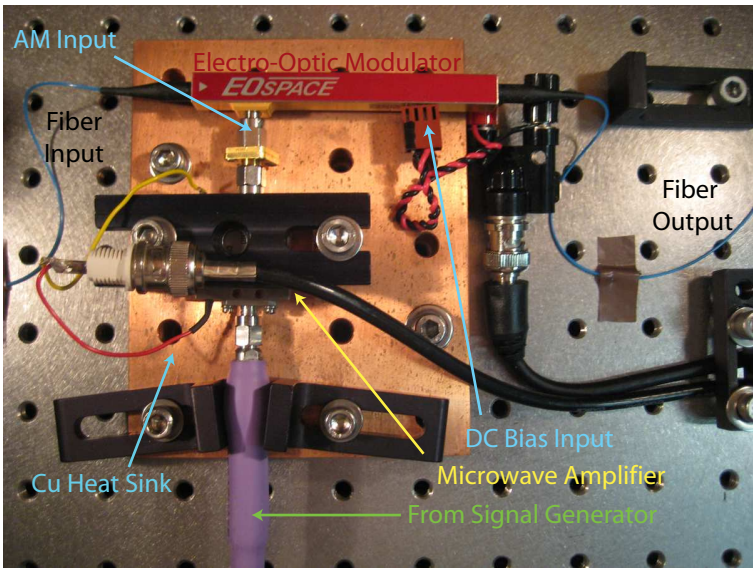

Figure 5.10: Picture of electro-optic modulator setup used to created amplitude modulated ponderomotive potentials.

The physical setup of the modulator is represented schematically in figure 5.3 and shown in the picture in figure 5.10. The DC bias input is used to set the point on the transmission curve (see figure A.1) about which the modulation signal is applied.

For our application, this is normally the quadrature point which corresponds to 50 % transmission. The AM input is a high frequency input that controls the amplitude modulation of the output. For our application, the AM signal is an amplified, single frequency, sinusoidal microwave signal from a signal generator (P/N: N5183A-540-1E1-UNT-UNW, Agilent Technologies) which produces a power output up to 7 dBm. The RF $V_\pi = 3.2$ V as quoted above, which corresponds to a microwave power of 20.1 dBm. To achieve powers in this range, the microwaves from the signal generator are amplified by a medium-power, solid-state amplifier (*e.g.*, P/N: ALS02406, Aldetec, Inc.) before being applied to the AM input. For our application, the nominal modulation amplitude corresponds to the RF $V_\pi/2$.

The transmission T through the modulator as a function of applied voltage V_{applied} is given by

$$T(V_{\text{applied}}) = \sin^2\left(\frac{\pi}{2}\frac{V_{\text{applied}}}{V_\pi}\right) \tag{5.2}$$

For our applications, the applied voltage consists of the sum of a DC voltage V_{bias} and an RF signal at frequecy Ω_{m} with amplitude V_{A} such that

$$T(V_{\text{bias}}, V_{\text{A}}, t) = \frac{1}{2} - \frac{1}{2}\cos\left[\pi\left(\frac{V_{\text{bias}}}{V_\pi(0)} + \frac{V_{\text{A}}}{V_\pi(\Omega_{\text{m}})}\sin(\Omega_{\text{m}}t)\right)\right] \tag{5.3}$$

where the use of two values of $V_\pi(0)$ and $V_\pi(\Omega_{\text{m}})$ reflects the frequency response of the modulator. Assuming that the signal is monitored on a slow detector that time averages over the fast modulation at frequencies Ω_{m}, the time average transmitted output is measured to be (see appendix A)

$$T(V_{\text{bias}}, V_{\text{A}}, t) = \frac{1}{2}\left[1 - J_0\left(\frac{\pi V_{\text{A}}}{V_\pi(\Omega_{\text{m}})}\right)\cos\left(\frac{\pi V_{\text{bias}}}{V_\pi(0)}\right)\right] \tag{5.4}$$

where J_0 is the zeroth order Bessel function. This equation provides a good description for the output of the modulator measured in figure 5.11.

The output of the modulator can be monitored on the photodiode PD in figure 5.3 with the beam reflected from M3 blocked to eliminate interference effects. The bias point can be easily set by dithering the DC bias input and noting the voltage corresponding to the maximum or minimum output (for modulation about an extremum of the transmission curve) or the voltage corresponding to where the output is the average of the maximum and minimum outputs (for modulation about the quadrature point). In our setup, computer generated analog modulation output is routed to the DC bias input of the modulator and the photodiode monitor signal is routed to an analog input on the computer allowing this process to be computer controlled.

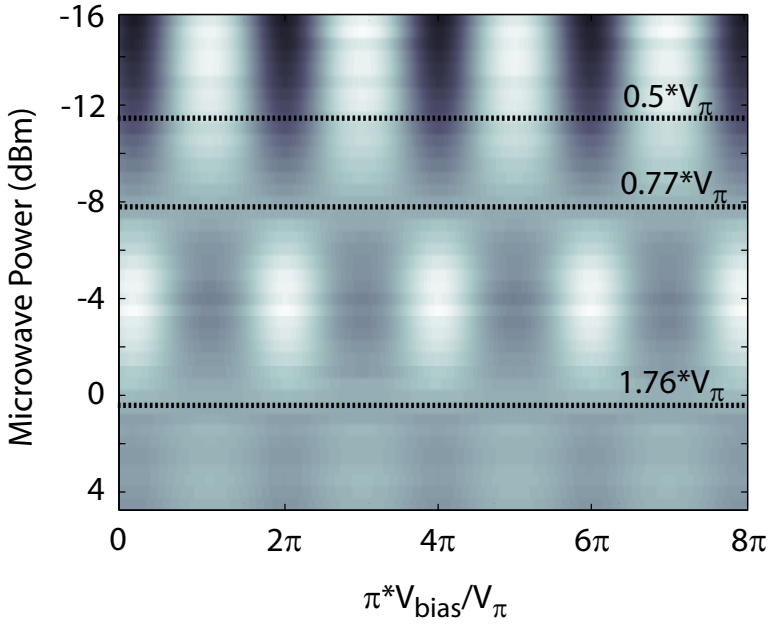

Figure 5.11: Transmission profile through the electro-optic modulator as a function of bias voltage and microwave power (*i.e.*, the amplitude of AM signal). For this data, $\Omega_{\mathrm{m}} = 25.5$ GHz.

The temporal modulation depth is dependent on the amplitude V_{A} of the AM signal, and must be set precisely at $V_{\pi}(\Omega_{\mathrm{m}})/2$ at the quadrature point for a depth of 100 %. The following is a technique for using a slow detector to appropriately calibrate the microwave power required to produce the desired modulation. Figure 5.11 shows the transmission through the modulator as a function of the DC bias voltage

V_{bias} and the microwave power output from the signal generator, which is amplified by $\approx$ 30 dBm and sent to the AM input of the modulator. We notice at two microwave powers (near -8 dBm and 0 dBm) the transmission through the modulator is independent of the DC bias voltage V_{bias}. This behavior is predicted by equation 5.4 to occur when the argument of the Bessel function is equal to a zero of the zeroth order Bessel function ($J_0(x_{0\text{k}}) = 0$) such that the corresponding amplitude V_{A} is given by

$$V_{\text{A}} = \frac{x_{0\text{k}}}{\pi} V_\pi(\Omega_{\text{m}}) \tag{5.5}$$

Since $x_{01} = 2.4048$, this condition is first satisfied at an amplitude of $V_{\text{A}} \approx 0.77 \times V_\pi(\Omega_{\text{m}})$. The target amplitude of $V_\pi(\Omega_{\text{m}})/2$ can be achieved by locating the $V_{\text{A}} \approx 0.77 \times V_\pi(\Omega_{\text{m}})$ point where the output is constant over the full range of bias voltages and reducing the microwave power by $\approx$ 3.75 dBm, as shown in figure 5.11.

The transmission curve (see figure A.1) displays a temperature dependence such that a change in temperature will displace the curve with respect to the applied voltage. This results in a temperature drift of the bias voltage V_{bias} appropriate for a particular type of modulation (*e.g.*, the quadrature point). For steady-state operating conditions, the bias voltage is stable over the timescale of several minutes. However, changes to the operating conditions that change the heat load on the device will cause an abrupt drift of the bias voltage which stabilizes as the modulator reaches a constant temperature. An important example of this is the drift that occurs when the microwave power sent to the modulator's AM input is changed. Usually the bias voltage will stabilize within thirty seconds of changing the power. In general, the time required for stabilization grows with the magnitude of the change in power.

The z-cut modulators are susceptible to a parasitic chirp on the modulator's output which is often quantified in terms of the chirp parameter [86]. We have not

determined the total effect of this parasitic chirp on the standing wave produced with the output of the modulator. Note that resonant phase modulation of a ponderomotive optical lattice can also drive transitions and should be a manageable effect if the phase modulation of the lattice is significantly less than 2π. However, a reduction in the interference of the lattice beams at the location of the atoms would reduce Rabi frequencies. We have observed that the visibility of the interference, measured using the Michelson interferometer described in section 5.2, remains quite large during the operation of the modulator at frequencies near 20 GHz.

The lattice is produced by retro-reflecting a beam, which is amplitude-modulated at high frequencies (*e.g.*, 20 GHz), from a mirror placed roughly $d_{\mathrm{retro}} = 40$ cm from the location where the beam must interfere with itself. The high-frequency modulation produces pulses of light lasting for a time $2\pi/\Omega_{\mathrm{m}}$ and covering a spatial extent of $L_{\mathrm{pulse}} = 2\pi c/\Omega_{\mathrm{m}}$. For $\Omega_{\mathrm{m}} = 2\pi \times 20$ GHz, $L_{\mathrm{pulse}} = 15$ mm, which is small compared to $d_{\mathrm{retro}} = 40$ cm. In order for the beams to interfere properly at the MOT location, the condition which must be satisfied is $2d_{\mathrm{retro}} = NL_{\mathrm{pulse}}$, where N is an odd integer. Experimentally, this distance d_{retro} would be optimized (over a distance L_{pulse}) by maximizing the Rabi frequency of transitions occuring in amplitude-modulated lattices. It may also be possible to set d_{retro} using a scheme that probes the state-dependent nature of the lattice induced shift. In the misaligned case, no lattice is formed at the location of the atoms, and the ponderomotive shift would be not be observable on a transition between Rydberg states.

5.6 Effects of Rydberg Atom Motion in a Ponderomotive Optical Lattice

For most Rydberg states, the energy level shift in a ponderomotive optical lattice strongly depends on the position of the Rydberg atom in the lattice. For the case of an

amplitude modulated lattice, the level shifts and Rabi frequencies are lattice-position dependent. Rydberg-atom motion in the lattice (normal to the lattice planes) arises primarily from two sources, thermal motion and ponderomotive forces caused by inhomogeneities in the applied optical field. Thermal motion will be important for cases where the lattice trap depth is smaller than average thermal energy $k_{\mathrm{B}}T$ of the ground state atoms (from which the Rydberg atoms are created). Typical Rydberg atom experiments in optical lattices (*e.g.*, driving transitions with an AM lattice) occur over a timescale of 5 μs. In this time, an atom moving freely with the average thermal velocity characteristic of $T = 30$ μK moves ≈ 270 nm (normal to the lattice planes), which is more than half a lattice period (532 nm) in a 1064 nm standing wave lattice. Motion on this scale during a lattice experiment would cause the Rydberg atom to sample a variety of energy level shifts or Rabi frequencies significantly altering the outcome of the experiment relative to stationary atoms.

We first consider the effects of motion on coupling Rydberg states using amplitude-modulated lattices. In figure 5.12, we present the target state population accounting for effects of motion using the following simple model. Experiments of this type anticipated to fall in the regime where the thermal energy is comparable to or exceeds the depth of the ponderomotive optical lattice. Therefore in this consideration, we assume the atoms move freely at a constant velocity and ignore the forces arising from the lattice. For a case of considerable interest ($58S$, AM lattice parameters leading to 100 kHz Rabi frequency), the thermal energy equals the lattice depth around 20 μK. For a Rydberg atom sampling a variety of Rabi frequencies over the duration t_{int} of a time-dependent perturbation which resonantly couples an initial and target state, the target state population is given by

$$P(t_{\mathrm{int}}) = \sin^2\left(\frac{1}{2}\int_0^{t_{\mathrm{int}}} \chi(t)dt\right) \tag{5.6}$$

The Rabi frequency in a ponderomotive optical lattice has the form $\chi(z) = \chi_0 \cos(2kz)$, where $k = 2\pi/1064$ nm. For an atom moving freely through the lattice with velocity v, the position of the atom is given by $z(t) = z(0) + vt$. Therefore, the time dependent Rabi frequency experienced by this atom is $\chi(t) = \chi_0 \cos[2k(z(0) + vt)]$.

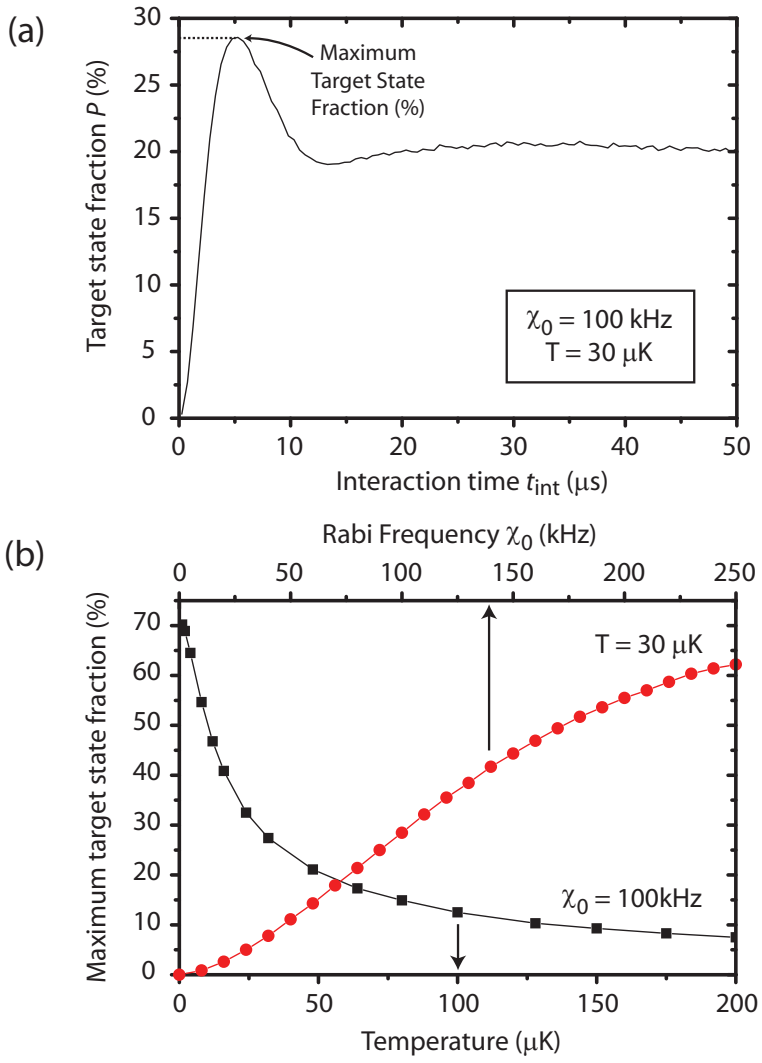

Figure 5.12: Target state fraction accounting for thermal motion of atoms as a function of (a) interaction time for given Rabi frequency and temperature and (b) Rabi frequency for given temperature (red circles) and temperature for a given Rabi frequency (black squares).

The plots in figure 5.12 were constructed by calculating the target state population from equation 5.6 averaging over trajectories in which $z(0)$ is distributed uniformly over a lattice period and v is chosen from a thermal velocity distribution

($v = v_{\rm rms}\sqrt{-2\ln x}$, where $v_{\rm rms} = \sqrt{k_{\rm B}T/M}$ and x is a random number uniformly distributed over the interval (0,1)). Figure 5.12(a) shows the target state population $P(t_{\rm int})$ for anticipated experimental parameters, $\chi_0 = 100$ kHz and temperature $T = 30$ μK. The target state probability increases to its maximum value of ≈ 27 % in a time $1/2\chi_0$ and proceeds to a slightly lower steady state value of ≈ 20 % in a time $2/\chi_0$. No Rabi oscillations are visible due to the significant range of Rabi frequencies sampled in the lattice. However, Rabi oscillations for even order transitions should, in principle, be observable in experiments with very cold atoms (whose thermal energy is much less than the lattice depth) that are created near the minima of the lattice potential and localized near the minima by ponderomotive forces.

In figure 5.12(b), the maximum target state population (defined in figure 5.12(a)) is plotted as a function of temperature T for a Rabi frequency $\chi_0 = 100$ kHz (black squares) and as a function of Rabi frequency χ_0 for a temperature $T = 30\mu$K (red circles). The maximal target state fraction becomes larger as the temperature decreases (black squares), which motivates the use of sub-Doppler laser-cooling techniques that are employed in our experiments (see section 5.1). Note that as the temperature drops below 30 μK the assumption that the lattice potential can be ignored becomes increasingly invalid. The maximal target state fraction grows as a function of Rabi frequency χ_0 (red circles) eventually saturating near 70 % due to the assumption in the model that atoms are uniformly distributed in the lattice.

Another important case is the limit in which the thermal energy of the atoms is negligible compared to the depth of the applied ponderomotive optical lattice. In this case, the energy level shift of a given Rydberg state as a function of lattice position (see, *e.g.*, figure 3.4) is the potential which governs the motion of Rydberg atoms over the duration of experiments. In this consideration, we describe a qualitative

picture of the effects of this motion on experiments spectroscopically probing the Rydberg-state dependent level shifts on microwave transitions between neighboring Rydberg states. The following consideration could be made more quantitative using a model analogous to the one used to construct figure 5.12. For this case, the model would need to track the average differential shift (with respect to the initial and target state) experienced by an atom accounting for its motion, which is governed by the ponderomotive optical lattice potential.

Atoms excited near the lattice potential maxima are created with enough potential energy to allow the range of motion to nearly cover the extent of a lattice period. Since the differential shift between two neighboring states (labeled $|\mathrm{i}\rangle$ and $|\mathrm{j}\rangle$) is of the form $\Delta W_{\mathrm{ij}}^{\mathrm{Q}}(z) = W_{\mathrm{ij}}^{\mathrm{Q}}(0)\cos(2kz)$, motion over a lattice period covers a range of energy shifts (both positive and negative) which would tend to broaden the microwave transition between states $|\mathrm{i}\rangle$ and $|\mathrm{j}\rangle$ and mitigate to a degree any overall energy shift. Meanwhile, atoms excited near the lattice potential minima are created with little potential energy and are thus confined to points in the lattice near their respective minima. These atoms sample a small range of differential shifts which are either positive or negative depending on the Rydberg states $|\mathrm{i}\rangle$ and $|\mathrm{j}\rangle$. The spectral line for this transition should exhibit a net frequency shift with little overall broadening. From the discussion in sections 3.3 and 3.4, it should be possible to control the initial potential energy of Rydberg atoms in a lattice by tuning the Rydberg excitation laser frequency. Given the ability to control the initial potential energy of Rydberg atoms in a lattice, demonstrating the potential-energy dependent effects on the $|\mathrm{i}\rangle$ to $|\mathrm{j}\rangle$ microwave transition as described above would provide substantial proof of Rydberg atom trapping in ponderomotive optical lattice.

CHAPTER VI

Outlook

In this thesis, we have examined the ponderomotive interaction between a Rydberg atom and an applied optical field. In particular, we focused on the case where the applied field is a 1D standing wave optical lattice. Using this field geometry, Rydberg atom motion (normal to the lattice planes) is governed by ponderomotive forces arising from spatial inhomogeneities in the applied field. Furthermore, amplitude modulation of this type of applied field at appropriate frequency couples Rydberg states allowing control of the internal states. Our theoretical investigations have produced a well-defined parameter space for producing measurable ponderomotive interactions with Rydberg atoms. These considerations have informed the development of techniques and the design of experiments to demonstrate control of Rydberg atom center-of-mass motion and internal states.

The next step is to utilize the techniques developed in chapter V to look for spectroscopic evidence of Rydberg-state dependent shifts on microwave transitions between neighboring Rydberg states (see figure 3.7). This type of measurement can be extended to demonstrate 1D Rydberg atom trapping as discussed in section 5.6. The key to these experiments is localizing Rydberg excitations to the volume subjected to the ponderomotive potential. With this capability in place, coupling Rydberg

states with a modulated optical lattice should be possible by applying the amplitude modulation techniques described in section 5.5 to the lattice beams and looking for population transfer from the initial to target state.

For initial experiments, the transition, $nS \rightarrow (n+1)S$, is the best candidate for obtaining clean results. In order to work with other transitions of interest (*e.g.*, measuring quantum defects on the nD to nf or nG transitions), a new apparatus, which is tailored to microwave spectroscopy applications (see the description of apparatus used in reference [28, 29]), is required. For microwave spectroscopy on most Rydberg transitions, precise control of electric and magnetic fields is essential. This will require MOT magnetic fields to be switched off [87–89] during the microwave probe. The apparatus should also be designed to maximize optical access to accommodate multiple lattice beams (for 2D and 3D lattices).

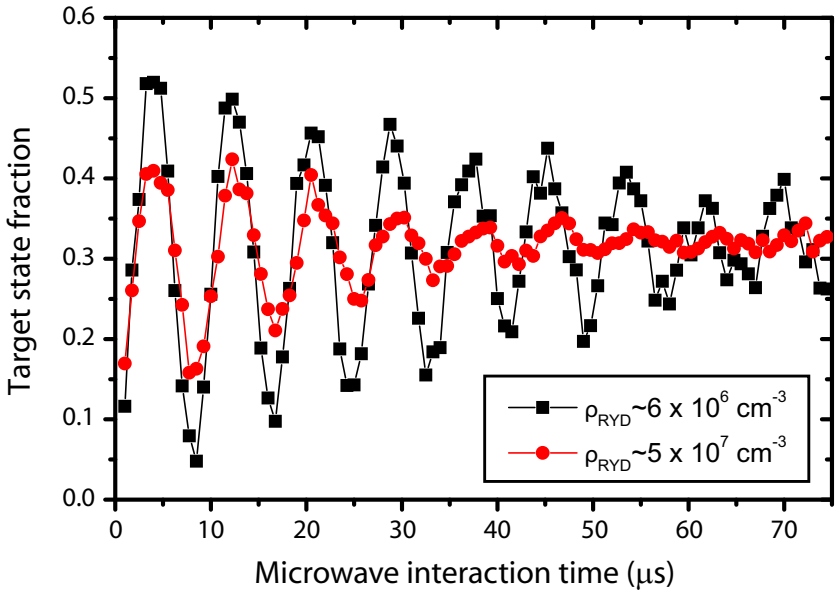

Figure 6.1: Target state fraction vs. Microwave interaction time for two different densities.

Development of an apparatus tailored to microwave spectroscopy could also be useful in studying interactions between Rydberg atoms [88, 90]. Figure 6.1 shows Rabi oscillations of the target state population on the $65S_{1/2} \rightarrow 66S_{1/2}$ for two differ-

ent Rydberg atom densities. While the frequency of the Rabi oscillation is the same for both densities, the decay rate of the oscillation amplitude is larger for the high density case (red circles). The increased damping most likely reflects decoherence in the Rydberg atom gas due to interactions among Rydberg atoms in the many-body system. Studies of this type, over a variety of timescales, densities, and Rydberg states may shed light on the decoherence processes in cold Rydberg gases. Similar observations have been made using a variant of the Ramsey method [91].

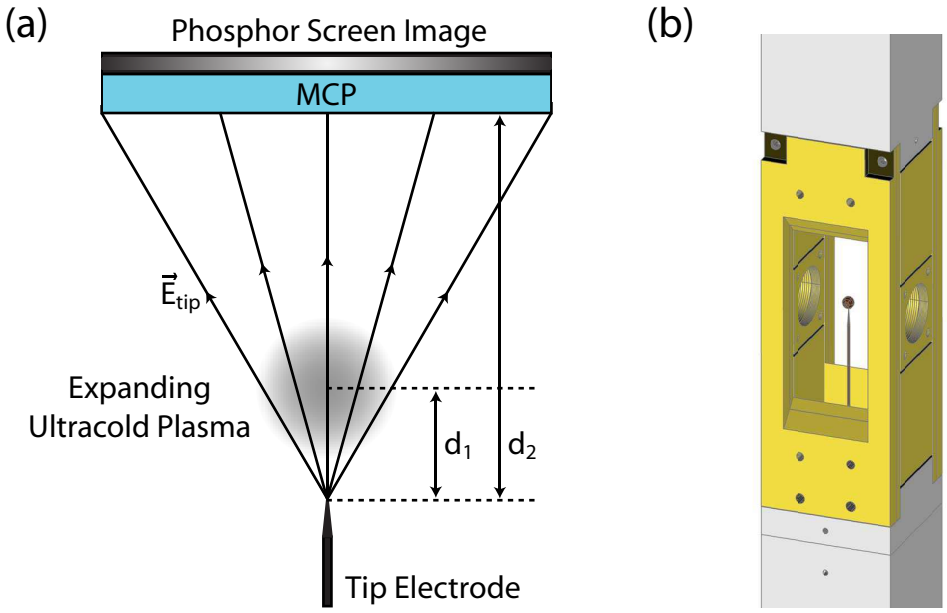

Figure 6.2: (a) Diagram of charged particle imaging using a tip electrode and (b) electrode package for controlling electric fields.

Figure 6.2(a) shows a schematic representation of a charged-particle imaging technique currently being developed in our group. By applying a voltage to the tip electrode, the resulting radial electric field projects charged particles originating, in this case, from the ultracold plasma located a distance d_1 from the tip. A magnified image of the ionic distribution of the ultracold plasma is projected onto the detector at a distance d_2 from the tip with a magnification factor of $M = d_2/d_1$. Such an apparatus is well-suited for time-resolved studies of plasma expansion and can also

be adapted to imaging Rydberg atom distributions in expanding plasmas. This capability would be useful in the studies of Rydberg atom formation in ultracold plasmas described in section 2.3.2. Another exciting possibility for this apparatus is imaging Rydberg excitations in the so-called dipole-blockade regime (see section 7.2.1 in reference [92]). A primary objective of this type of investigation would be to observe anticorrelation in the distribution of Rydberg excitations.

APPENDIX

APPENDIX A

Bessel Function Expansion of Electro-Optic Modulator Transmission Function

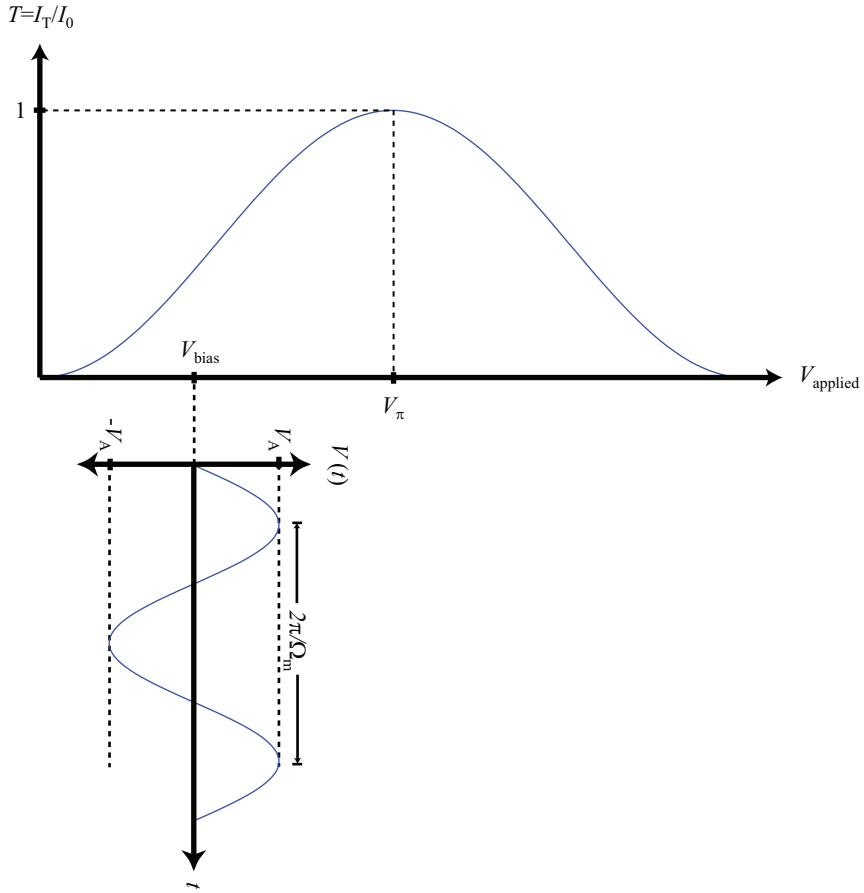

Figure A.1: Transmission through EOM as a function of applied voltage.

The transmission through an electro-optic modulator as a function of the applied

voltage is given by [93]:

$$T(V_{\text{applied}}) = \sin^2(\frac{\pi}{2}\frac{V_{\text{applied}}}{V_\pi})$$

$$V_{\text{applied}} = V_{\text{bias}} + V_{\text{A}}\sin(\Omega_{\text{m}}t)$$

$$T(V_{\text{A}}, V_{\text{bias}}, t) = \frac{1}{2} - \frac{1}{2}\cos[\frac{\pi}{V_\pi}(V_{\text{bias}} + V_{\text{A}}\sin(\Omega_{\text{m}}t))]$$

$$x = \frac{\pi V_{\text{A}}}{V_\pi(0)}, \phi = \frac{\pi V_{\text{bias}}}{V_\pi(\Omega_{\text{m}})}, \theta = \Omega_{\text{m}}t$$

where the use of $V_\pi(0)$ and $V_\pi(\Omega\text{m})$ reflects the frequency response of the modulator.

$$T(x, \phi, \theta) = \frac{1}{2} - \frac{1}{2}\cos(x\sin\theta + \phi)$$

To evalulate $T(x, \phi, \theta)$, perform Bessel function expansion of T, we begin with the Bessel generating function is given by [94]

$$e^{(x/2(t-1/t))} = \sum_{n=-\infty}^{\infty} J_n(x)t^n$$

$$t = e^{i\theta} \Rightarrow e^{ix\sin\theta} = \sum_{n=-\infty}^{\infty} J_n(x)e^{in\theta}$$

$$t = e^{-i\theta} \Rightarrow e^{-ix\sin\theta} = \sum_{n=-\infty}^{\infty} J_n(x)e^{-in\theta} = \sum_{n=-\infty}^{\infty} (-1)^n J_n(x)e^{in\theta}$$

$$\begin{aligned}\cos(x\sin\theta + \phi) &= (e^{i\phi}e^{ix\sin\theta} + e^{-i\phi}e^{-ix\sin\theta})/2 \\ &= \frac{1}{2}\sum_{n=-\infty}^{\infty}(e^{i\phi} + (-1)^n e^{-i\phi})J_n(x)e^{in\theta}\end{aligned}$$

$$\begin{aligned} n = 0 &\rightarrow \cos\phi J_0(x) \\ n \in \mathbb{Z}_{even} &\rightarrow cos\phi \sum_{n_{\text{even}}=-\infty}^{\infty} J_n(x)e^{in\theta} = 2\cos\phi \sum_{n_{\text{even}}=2}^{\infty} J_n(x)\cos(n\theta) \\ n \in \mathbb{Z}_{odd} &\rightarrow sin\phi \sum_{n_{\text{odd}}=-\infty}^{\infty} J_n(x)e^{in\theta} = -2\sin\phi \sum_{n_{\text{odd}}=0}^{\infty} J_n(x)\sin(n\theta) \end{aligned}$$

$$T(x,\phi,\theta) = \frac{1}{2}(1-J_0(x)\cos\phi) + \sin\phi \sum_{n_{\text{odd}}=1}^{\infty} J_n(x)\sin(n\theta) - \cos\phi \sum_{n_{\text{even}}=2}^{\infty} J_n(x)\cos(n\theta)$$

From this expression, the frequency spectrum of the modulated light field is evident. If a slow detector is used to monitor the output of the modulator, then the relevant time averaged intensity output can be obtained from

$$T(x,\phi,\theta) = \frac{1}{2}(1 - J_0(x)\cos\phi)$$

In terms of the physical parameters in the system,

$$T(V_{\text{A}}, V_{\text{bias}}) = \frac{1}{2}\left[1 - J_0\left(\frac{\pi V_{\text{A}}}{V_\pi(\Omega_{\text{m}})}\right)\cos\left(\frac{\pi V_{\text{bias}}}{V_\pi(0)}\right)\right]$$

The output intensity of the modulator is independent of the bias voltage when the microwave power input to the modulator is set such that

$$V_A = \frac{V_\pi}{\pi} x_{0\text{k}}$$

where $x_{0\text{k}}$ is the kth root of the $J_0(x)$ Bessel function.

BIBLIOGRAPHY

BIBLIOGRAPHY

[1] T. F. Gallagher. *Rydberg Atoms*. Cambridge University Press, New York, 1994.

[2] M. D. Lukin, M. Fleischhauer, R. Côté, L. M. Duan, D. Jaksch, J. I. Cirac, and P. Zoller. Dipole blockade and quantum information processing in mesoscopic atomic ensembles. *Phys. Rev. Lett.*, 87:037901, 2001.

[3] A. Gaëtan, Y. Miroshnychenko, T. Wilk, A. Chotia, M. Viteau, D. Comparat, P. Pillet, A. Browaeys, and P. Grangier. Observation of collective excitation of two individual atoms in the rydberg blockade regime. *arXiv:0810.2960v1*, 2008.

[4] D. Jaksch, J. I. Cirac, P. Zoller, S. L. Rolston, R. Côté, and M. D. Lukin. Fast quantum gates for neutral atoms. *Phys. Rev. Lett.*, 85:2208, 2000.

[5] P. J. Tanner, J. Han, E. S. Shuman, and T. F. Gallagher. Many-body ionization in a frozen rydberg gas. *Phys. Rev. Lett.*, 100:043002, 2008.

[6] A. Reinhard, T. Cubel Liebisch, K. C. Younge, P. R. Berman, and G. Raithel. Rydberg-rydberg collisions: Resonant enhancement of state mixing and penning ionization. *Phys. Rev. Lett.*, 100:123007, 2008.

[7] A. Walz-Flannigan, J. R. Guest, J.-H. Choi, and G. Raithel. Cold-rydberg-gas dynamics. *Phys. Rev. A*, 69:063405, 2004.

[8] B. Knuffman and G. Raithel. Emission of fast atoms from a cold rydberg gas. *Phys. Rev. A*, 73(020704(R)), 2006.

[9] T. C. Killian, S. Kulin, S. D. Bergeson, L. A. Orozco, C. Orzel, and S. L. Rolston. Creation of an ultracold neutral plasma. *Phys. Rev. Lett.*, 83(23):4776, 1999.

[10] D. Umstadter, J. K. Kim, and E. Dodd. Laser injection of ultrashort electron pulses into wakefield plasma waves. *Phys. Rev. Lett.*, 76:2073, 1996.

[11] Y. Kitigawa, T. Matsumoto, T. Minamihata, K. Sawai, K. Matsuo, K. Mima andK Nishihara, H. Azechi, K. A. Tanaka, H. Takabe, and S. Nakai. Beat-wave excitation of plasma wave and observation of accelerated electrons. *Phys. Rev. Lett.*, 68:48, 1992.

[12] W. Paul. Electromagnetic traps for charged and neutral particles. *Rev. Mod. Phys.*, 62(3):531, 1990.

[13] C. E. Wieman, D E. Pritchard, and D. J. Wineland. Atom cooling, trapping, and quantum manipulation. *Rev. Mod. Phys.*, 71(2):S253, 1999.

[14] M. Lewenstein, Ph. Balcou, M. Yu. Ivanov, A. LHuillier, and P. B. Corkum. Theory of high-harmonic generation by low-frequency laser fields. *Phys. Rev. A*, 49:2117, 1994.

[15] J. M. Raimond, M. Brune, and S. Haroche. Manipulating quantum entanglement with atoms and photons in a cavity. *Rev. Mod. Phys.*, 73:565, 2001.

[16] J. H. Choi, J. R. Guest, A. P. Povilus, E. Hansis, and G. Raithel. Magnetic trapping of long-lived cold rydberg atoms. *Phys. Rev. Lett.*, 95:243001, 2005.

[17] S. D. Hogan and F. Merkt. Demonstration of three-dimensional electrostatic trapping of state-selected rydberg atoms. *Phys. Rev. Lett.*, 100:043001, 2008.

[18] B. Knuffman and G. Raithel. Multipole transitions of rydberg atoms in modulated ponderomotive potentials. *Phys. Rev. A*, 75:053401, 2007.

[19] I. Mourachko, D. Comparat, F. de Tomasi, A. Fioretti, P. Nosbaum, V. M. Akulin, and P. Pillet. Many-body effects in a frozen rydberg gas. *Phys. Rev. Lett.*, 80(2):253, 1998.

[20] W. R. Anderson, J. R. Veale, and T. F. Gallagher. Resonant dipole-dipole energy transfer in a nearly frozen rydberg gas. *Phys. Rev. Lett.*, 80(2):249, 1998.

[21] Phil H. Bucksbaum, D. W. Schumacher, and M. Bashkansky. High-intensity kaptiza-dirac effect. *Phys. Rev. Lett.*, 61:1182, 1988.

[22] D. L. Freimund, K. A. Aflatooni, and H. Batelaan. Observation of the kapitza-dirac effect. *Nature*, 413:42, 2001.

[23] D. L. Freimund and H. Batelaan. Bragg scattering of free electrons using the kapitza-dirac effect. *Phys. Rev. Lett.*, 89(28):283602, 2002.

[24] S. Liberman, J. Pinard, and A. Taleb. Experimental study of stimulated radiative corrections on an atomic rydberg state. 1983.

[25] S. K. Dutta, J. R. Guest, D. Feldbaum, A. Walz-Flannigan, and G. Raithel. Ponderomotive optical lattice for rydberg atoms. *Phys. Rev. Lett.*, 85(26):5551, 2000.

[26] J. E. Sansonettia. Wavelengths, transition probabilities, and energy levels for the spectra of rubidium (rbi through rbxxxvii). *J. Phys. Chem. Ref. Data*, 35(1):301, 2005.

[27] D. A. Steck. Rubidium 85 d line data. *available online at http://steck.us/alkalidata (revision 0.2)*, 2008.

[28] W. Li, I. Mourachko, N. W. Noel, and T. F. Gallagher. Millimeter-wave spectroscopy of cold rb rydberg atoms in a magneto-optical trap: Quantum defects of the ns, np, and nd series. *Phys. Rev. A*, 67:052502, 2003.

[29] J. Han, Y. Jamil, D. V. L. Norum, P. J. Tanner, and T. F. Gallagher. Rb nf quantum defects from millimeter-wave spectroscopy of cold ^{85}rb rydberg atoms. *Phys. Rev. A*, 74:054502, 2006.

[30] S. K. Dutta, D. Feldbaum, A. Walz-Flannigan, J. R. Guest, and G. Raithel. High-angular-momentum states in cold rydberg gases. *Phys. Rev. Lett.*, 86(18):3993, 2001.

[31] Wenhui Li, Paul J. Tanner, and T. F. Gallagher. Dipole-dipole excitation and ionization in an ultracold gas of rydberg atoms. *Phys. Rev. Lett.*, 94:173001, 2005.

[32] A. Reinhard, T. Cubel Liebisch, B. Knuffman, and G. Raithel. Level shifts of rubidium rydberg states due to binary interactions. *Phys. Rev. A*, 75:032712, 2007.

[33] F. Robicheaux. Ionization due to theinteraction between two rydberg atoms. *J. Phys. B*, 38: S333, 2005.

[34] K. L. Bell, A. Dalgarno, and A. E. Kingston. Penning ionization by metastable helium atoms. *J. Phys. B*, 1:1, 1968.

[35] H. Nakamura. Theoretical considerations on penning ionization processes. *Journal of the Physical Society of Japan*, 26(6):1473, 1969.

[36] W. H. Miller. Theory of penning ionzation i. atoms. *Journal of Chemical Physics*, 52(7):3563, 1970.

[37] E. Illenberger and A. Niehaus. Velocity dependence of total penning ionization cross sections. *Z. Physik B*, 20:33, 1975.

[38] Z. T. Lu, K. L. Corwin, M. J. Renn, M. H. Anderson, E. A. Cornell, and C. E. Weiman. Low-velocity intense source of atoms from a magneto-optical trap. *Phys. Rev. Lett.*, 77(16): 3331, 1996.

[39] A. Walz-Flannigan, D. Feldbaum, S. K. Dutta, J. R. Guest, and G. Raithel. l-changing collisions in cold rydberg gases. In J. Burgdoerfer, J. S. Cohen, S. Datz, and C. R. Van, editors, *Photonic, Electronic and Atomic Collisions (XXII ICPEAC Proceedings)*. Rinton Press, 2002.

[40] T. C. Killian, M. J. Lim, S. Kulin, R. Dumke, S. D. Bergeson, and S. L. Rolston. Formation of rydberg atoms in an expanding ultracold neutral plasma. *Phys. Rev. Lett.*, 86(17):3759, 2001.

[41] M. P. Robinson, B. Luburthe Tolra, M. W. Noel, T. F. Gallagher, and P. Pillet. Spontaneous evolution of rydberg atoms into an ultracold plasma. *Phys. Rev. Lett.*, 85(21):4466, 2000.

[42] Nicolas Vanhaecke, D. Comparat, Duncan A. Tate, and P. Pillet. Ionization of rydberg atoms embedded in an ultrcold plasma. *Phys. Rev. A*, 71:013416, 2005.

[43] S. Kulin, T. C. Killian, S. D. Bergeson, and S. L. Rolston. Plasma oscillations and expansion of an ultracold neutral plasma. *Phys. Rev. Lett.*, 85(2):318, 2000.

[44] D. Feldbaum, N. V. Morrow, S. K. Dutta, and G. Raithel. Coulomb expansion of laser-excited ion plasmas. *Phys. Rev. Lett.*, 89(17):173004, 2002.

[45] F. Robicheaux and James D. Hanson. Simulated expansion of an ultra-cold, neutral plasma. *Phys. Plasmas*, 10(6):2217, 2003.

[46] S. Mazevet, L. A. Collins, and J. D. Kress. Evolution of ultracold neutral plasmas. *Phys. Rev. Lett.*, 88(5):055001, 2002.

[47] T. C. Killian, T. Pattard, T. Pohl, and J. M. Rost. Ultracold neutral plasmas. *Physics Reports*, 449:77, 2007.

[48] P. Mansbach and J. Keck. Monte carlo trajectory calculations of atomic excitation and ionization by thermal electrons. *Physical Review*, 181(1):275, 1969.

[49] M. E. Glinsky and T. M. O'Neil. Guiding center atoms: Three-body recombination in strongly magnetized plasmas. *Phys. Fluids B*, 3(5):1279, 1991.

[50] F. Robicheaux and James. D. Hanson. Simulation of the expansion of an ultracold neutral plasma. *Phys. Rev. Lett.*, 88(5):055002, 2002.

[51] F. Robicheaux and J. D. Hanson.

[52] R. S. Fletcher, X. L. Zhang, and S. L. Rolston. Using three-body recombination to extract electron temperatures of ultracold plasmas. *Phys. Rev. Lett.*, 99:145001, 2007.

[53] Y. Hahn. Improved rates for three-body recombination at low temperature. *Physics Letters A*, 264(6):465, 2000.

[54] T. Pohl, D. Vrinceanu, and H. R. Sadeghpour. Rydberg atom formation in ultracold plasmas: Small energy transfer with large consequences. *Phys. Rev. Lett.*, 100:223201, 2008.

[55] M. S. Murillo. Using fermi statistics to create strongly coupled ion plasmas in atom traps. *Phys. Rev. Lett.*, 87(11):115003, 2001.

[56] P. Gupta, S. Laha, C. E. Simien, H. Gao, J. Castro, T. C. Killian, and T. Pohl. Electron-temperature evolution in expanding ultracold neutral plasmas. *Phys. Rev. Lett.*, 99:075005, 2007.

[57] D. H. E. Dubin and T. M. O'Neil. Trapped nonneutral plasmas, liquids, and crystals (the thermalequilibrium states). *Rev. Mod. Phys.*, 71:87, 1999.

[58] M. Amoretti e.t. al. Production and detection of cold antihydrogen atoms. *Nature*, 419:456, 2002.

[59] G. Gabrielse e.t. al. Background-free observation of cold antihydrogen with field-ionization analysis of its states. *Phys. Rev. Lett.*, 89(21):213401, 2002.

[60] J.-H. Choi, B. Knuffman, X. H. Zhang, A. P. Povilus, and G. Raithel. Trapping and evolution dynamics of ultracold two-component plasmas. *Phys. Rev. Lett.*, 100:175002, 2008.

[61] J. R. Guest, J.-H. Choi, A. P. Povilus, E. Hansis, and G. Raithel. Laser cooling and magnetic trapping at several tesla. *Phys. Rev. Lett.*, 94:073003, 2005.

[62] G. Raithel, B. Knuffman, M. H. Shah, C. Hempel, E. Paradis, R. Mhaskar, X. Zhang, J.-H. Choi, A. P. Povilus, and J. R. Guest. Atoms and plasmas in a high-magnetic-field trap. In Y. Kanai and Y. Yamazaki, editors, *Cold Antimatter Plasmas and Application to Fundamental Physics (AIP Conference Proceedings)*, volume 1037, page 178, 2008.

[63] T. Pohl, T. Pattard, and J. M. Rost. Kinetic modeling and molecular dynamics simulation of ultracold neutral plasmas including ionic correlations. *Phys. Rev. A*, 70:033416, 2004.

[64] George Schmidt. *Physics of High Temperature Plasmas*. Academic Press, Inc., 1979.

[65] D. Umstadter. Relativistic laserplasma interactions. *J. Phys. D: Appl. Phys.*, 36:R151, 2003.

[66] P. Avan, C. Cohen-Tannoudji, J. Dupont-Roc, and C. Fabre. Effect of high frequency irradiation on the dynamical properties of weakly bound electrons. 1976.

[67] H. Maeda, D. V. L. Norum, and T. F. Gallagher. Microwave manipulation of an atomic electron in a classical orbit. *Science*, 307:1757, 2005.

[68] Harald Friedrich. *Theoretical Atomic Physics*. Springer-Verlag, New York, 1991.

[69] Jean-Patrick Connerade. *Highly Excited Atoms*. Cambridge University Press, Cambridge, U. K., 1998.

[70] J. Liang, M. Gross, P. Goy, and S. Haroche. Circular rydberg-state spectroscopy. 1986.

[71] Anthony E. Siegman. *Lasers*. University Science Books, 1986.

[72] M. Marinescu, H. R. Sadeghpour, and A. Dalgarno. Dynamic dipole polarizabilities of rubidium. 1994.

[73] F. Robicheaux, J. V. Hernández, T. Topçu, and L. D. Noordam. Simulation of coherent interactions between rydberg atoms. *Phys. Rev. A*, 70:042703, 2004.

[74] J.-H. Choi, B. Knuffman, T. Cubel-Liebisch, A. Reinhard, and G. Raithel. Cold rydberg atoms. *Advances in Atomic, Molecular, and Optical Physics*, 54:132, 2007.

[75] I. Lesanovsky, J. Schmiedmayer, and P. Schmelcher.

[76] I. Lesanovsky and P. Schmelcher. Magnetic trapping of ultracold rydberg atoms. 2005.

[77] J. D. Jackson. *Classical Electrodynamics*. John Wiley & Sons, Inc., New York, 1998.

[78] M. O. Scully and M. S. Zubairy. *Quantum Optics*. Cambridge University Press, Cambridge, 1997.

[79] L. Allen and J. H. Eberly. *Optical Resonance and Two-Level Atoms*. John Wiley & Sons, Inc., New York, 1975.

[80] see, e.g., eospace, inc., http://www.eospace.com/.

[81] E. Merzbacher. *Quantum Mechanics*. John Wiley & Sons, Inc., New York, 1998.

[82] H. J. Metcalf and P. van der Straten. *Laser Cooling and Trapping*. Springer-Verlag New York, Inc., New York, 1999.

[83] J. Hare, M. Gross, and P. Goy. Circular atoms prepared by a new method of crossed electric and magnetic fields. *Phys. Rev. Lett.*, 61:1938, 1988.

[84] P. Meystre and M. Sargent. *Elements of Quantum Optics*. Spring-Verlag, Inc., Berlin, 2007.

[85] T. R. Gentile, B. R. Hughley, D. Kleppner, and T. W. Ducas. Experimental study of one- and two-photon rabi oscillations. *Phys. Rev. A*, 40:5103, 1989.

[86] T. Kawanishi, K. Kogo, S. Oikawa, and M. Izutsu. Direct measurement of chirp parameters of high-speed mach-zehnder-type opitcal modulators. *Optics Communications*, 195:399, 2001.

[87] C. J. Dedman, K. G. H. Baldwin, and M. Colla. Fast switching of magnetic fields in a magneto-optic trap. *Review of Scientific Instruments*, 72:4055, 2001.

[88] K. Afrousheh, P. Bohlouli-Zanjani, J. D. Carter, A. Mugford, and J. D. D. Martin. Resonant elecrtic dipole-dipole interactions between cold rydberg atoms in a manetic field. *Phys. Rev. A*, 73:063403, 2006.

[89] M. Harvey and A. J. Murray. Cold atom trap with zero residual magnetic field: The ac magneto-optical trap. *Phys. Rev. Lett.*, 101:173201, 2008.

[90] K. Afrousheh, P. Bohlouli-Zanjani, D. Vasale, A. Mugford, M. Federov, and J. D. D. Martin. Spectroscopic observation of resonant electric dipole-dipole interactions between cold rydberg atoms. *Phys. Rev. Lett.*, 93:233001, 2004.

[91] P. Pillet, D. Comparat, M. Muldrich, T. Vogt, N. Zahzam, V. M. Akulin, T. F. Gallagher, W. Li, P. Tanner, M. W. Noel, and I. Mourachko. Coherence and decoherence in rydberg gases. In V. M. Akulin et al., editor, *Decoherence, Entanglement and Information Protection in Complex*. Springer, 2005.

[92] A. Reinhard. Cold rydberg-atom interactions. *Ph. D. Thesis, University of Michigan*, 2008.

[93] A. Yariv and P. Yeh. *Optical Waves in Crystals*. John Wiley & Sons, Inc., New York, 2003.

[94] G. B. Arfken and H. J. Weber. *Mathematical Methods for Physicists*. Elsevier Academic Press, New York, 2005.